Influence of some sterols and nucleotides on the structure of self-assembled amphiphilic systems

by
Madhukar S

A thesis submitted to the Jawaharlal Nehru University
for the degree of

Doctor of Philosophy

2017

Raman Research Institute
Bangalore 560080
India

DECLARATION

I hereby declare that this thesis is composed independently by me at Raman Research Institute, Bangalore under the supervision of Prof.V.A.Raghunathan. The subject matter presented in this thesis has not previously formed the basis of the award of any degree, diploma, associateship, fellowship or any other similar title. I also declare that I have run it through the **Turnitin** plagiarism software.

(Prof.V.A.Raghunathan) (Madhukar S)

Raman Research Institute

Bangalore 560080

CERTIFICATE

This is to certify that the thesis entitled **Influence of some sterols and mononucleotides on the structure of self-assembled amphiphilic systems** submitted by Madhukar S for the award of degree DOCTOR OF PHILOSOPHY of Jawaharlal Nehru University is his original work. This has not been published or submitted to any other university for any other degree or diploma.

Prof. R.Subrahmanyan
Director
Raman Research Institute
Bangalore 560080 INDIA

Prof.V.A.Raghunathan
(Thesis Supervisor)

Acknowledgements

It has been an absolute privilege to work with Raghu. His ability to calmly extract sensible solutions using clear logic from seemingly insurmountable problems has never ceased to fill me with awe. I thank him a lot for patiently explaining concepts and developing my skills to the point where I am at now. Further, his composure and clarity on a range of topics (Including the ability to make the best coffee ever, Period!) make him in my opinion a true modern day Renaissance man. To be his student is an honour. Thank you Raghu.

Yashodhan (Yhat) is a teacher par excellence with an immense grasp of measure and has been a steadying influence. I am forever thankful to him for all the lectures he has given us in RRI and for drumming up some sense into me. I would also like to thank Pramod for all the incisive questioning and constant support through my time here.

My time in RRI has been further enriched through the lectures and discussions I have attended and had with the faculty in the SCM department and I thank them sincerely.

I am eternally grateful to all the wonderful teachers I had at Vivekananda College. They, V.Murugan, R.Sudarshan and J.Segar, have been instrumental in invoking in me the need to explore (and have fun doing) physics.

I have been incredibly fortunate in having found Radhakrishnan (RK), Jayakumar (JK) and Madhavan who have become absolute friends. I would like to thank RK for aligning me with his strong field, JK for completely renormalizing me and Madhavan for providing all the compact support. From explaining topology to exploring topography; they have shaped me . I owe my very spirit to them and I thank them a lot.

I would like to thank Bibhuranjan and RK for all the help and training they provided in our lab that has helped me stand and work in good rigour. I would like to thank all my lab members Santosh, Meera, Shabeeb, Sreeja, Surya and Anindyo for making the

lab an ideal workplace and a fun environment to be in. I would like to especially thank Sreeja for all the time-bound help and Meera for currying out spectacular flavours. I am extremely thankful to Ms.Vasudha for conducting all the CHNS elemental analysis trials and adding a lot of liveliness to our lab.

I am extremely thankful to Swamynathan and Marichandran who have provided me with much fodder for thought and given me great joy. I would also like to thank Jagadeesh, Chandan, Asha, Sanjay, Amit, Jagdish and Irla for all the fun times.

A lot of the experiments would not have been feasible if not for the dextrous hands in our workshop. In this regard I would like to specially thank Mr.Mani, Mr.Dhason and Mr.Ramasubramanyom.

I thank Raja and Murali for all the help. I am also very thankful to Pushparaj for all the help.

I thank all the other non-academic staff in RRI for all the prompt help provided over the years. I would like to thank all the staff at the library and computer section for the near immediate attention paid to the needs of all students. I would like to thank Mr.K.Radhakrishna, Ms. Marisa, Ms. K Radha and Mr.G.Manjunatha for all the help with regard to the processing of all the paperwork. I would also like to thank Mr.K.Krishnamaraju and Mr.C.S.R.Murthy for all the administrative help given.

My stay in RRI has been greatly enlivened through a lot of friends made in other labs and departments. I would like to especially thank Seshagiri, Chaitra, Kripa, Suresh (G.B), Nishant, Chandrakant , Sridhar and Sharadhini for all the jaunts and live music you treated me to. I would also like to thank Usha, Swati, Anupama and Divya, Maya ,Ambaran and Aksharan for all the good times.

I would like to thank the IISc Hockey club and all my wonderful friends there for all the friendly jousts and making evenings most enjoyable.

I am sincerely grateful to Dr.N.Chetan, Dr.J.Chandan, Dr.N.S.Saloni and Dr.P.H.Prasad for seeing me through some harrowing times post-surgery and having me back on my feet with my enthusiasm intact.

I have been incredibly lucky to have buddies from ye olde times Indira, Meghna, Saloni, Aditya, Bhavik and Siddharth who have always had my back and I thank them for

everything they have done for me. I would like to thank the gang at Loyola, Abinesh, Arun, Dinesh, Marian, Serdeen and Sridhar for all the ragging and always finding reasons to howl at the moon.

I thank Premila, Ramesh and Dikshit for all the support and encouragement.

I thank Radhe aunty and Thambudu for all the love they showered on me.

Rashmi and Mohan have always brought a lot of jolly into my life. I thank them for giving me sage-like wisdom on any issue troubling me. I thank Rohini for being a ray of sunshine and making my sides ache with her jokes.

Ranjani and Venkat have been my muses. I thank them for the various hues they have coloured into my life through their stories and taking me constantly on a whirlwind tour of creative forces that they are.

Immi is bar none the strongest person I have ever known. She has been an absolute inspiration for all that I do. I thank her for that.

Ma and Pa, words cannot express what I feel. You are divine. Thanks for everything.

Synopsis

This thesis documents our investigations into the structure and stability of self assembled systems of varied morphologies. The systems considered range from polymeric macro-ion complexes, formed by deoxyribonucleic acid (DNA) and oppositely charged cylindrical surfactant micelles; to sheet-like lipid bilayer systems, with a host of adsorbed and embedded molecules. We use Small Angle X-ray Scattering (SAXS) and elemental analysis techniques to chart and model the aforementioned systems.

In Chapter I we give a brief introduction to the physical principles behind self-assembly. We touch upon the specifics of the underlying interactions relevant to our systems. We also provide a comprehensive guide to the literature, pertaining to the various systems under study. We give an introduction to the methods of X-ray diffraction analysis of aligned (oriented) and unoriented (powder) samples. We then describe procedures used for data collection, and detail the modelling and fitting routines employed to construct electron density maps. We also discuss details of calculating the stoichiometry of complexes, based on relative contributions from individual constituent species, through elemental analysis.

Chapter II deals with studies that establish the stoichiometry, structure and stability of complexes, formed by the cationic surfactant cetyltrimethylammonium tosylate (CTAT) and DNA, a semi-flexible anionic polyelectrolyte. It has been reported earlier that along the ρ-C_s plane, where ρ is the CTAT to DNA base molar ratio and C_s the total CTAT concentration, the complexes lock into different two dimensional structures; a square lattice S_I^c, a hexagonal lattice H_I^c, and a swollen $\sqrt{3} \times \sqrt{3}$ superlattice $H_{I,s}^c$ of H_I^c. Here we report structural changes of the complexes when subjected to osmotic pressure, through immersion in solutions of neutral long chained polymers, like polyvinylpyrrolidone (PVP) or polyethyleneglycol (PEG). We observe the transformation of the swollen $H_{I,s}^c$ into the regular H_I^c lattice through the expungement of water with increasing osmotic pressure.

We also confirm using elemental analysis the organization of micelles and DNA within the three types of lattices, proposed based on the SAXS data.

In Chapter III, we probe the structure of complexes formed by DNA and the cationic amphiphile cetyltrimethylammonium bromide (CTAB). We study the effect of monovalent salt NaCl on the structure of these complexes at different values of ρ. We observe only the simple hexagonal lattice (H_I^c) throughout the entire range ρ probed. We compare two different models proposed in the literature that have basic repeating units of 2:1 and 3:1 DNA to micelle ratios, respectively, and establish that only the 2:1 model fits the observed data consistently. We also justify the structure from elemental analysis conducted on the complexes.

In Chapter IV, we study the complexation of DNA and the cationic amphiphile with a shorter hydrocarbon chain, dodecyltrimethylammonium bromide (DTAB). We study the effect of monovalent salt NaCl on the structure of these complexes and construct a phase diagram in the ρ- salt concentration plane. We again observe the square phase S_I^c and the superlattice $H_{I,s}^c$ phase, but not the simple hexagonal lattice (H_I^c). Further, we do not observe a transformation of the $H_{I,s}^c$ phase under osmotic pressure. The proposed structures are further justified from a comparison of values of ρ for different phases obtained from structural considerations and from elemental analysis.

Chapter V looks at the effect of cholecalciferol (vitamin D3) on the structure and phase behaviour of lipid bilayer systems. Secosteroids, such as vitamin D3, are biologically important structural derivatives of cholesterol, where the B-ring of the sterol core is broken. Earlier experimental reports of x-ray scattering analysis on aligned multilayer samples of dipalmitoyl phosphatidylcholine (DPPC) membranes with vitamin D3 presented a rich and unique phase diagram. It contained four distinct one dimensional modulated phases, including a very unusual centred-rectangular (RC) phase. We propose and undertake detailed modelling of the structures and especially elaborate on how the RC phase is a natural outcome of thickness modulation.

In Chapter VI we study the behaviour of binary mixtures of oxygenated derivatives of cholesterol embedded in lipid bilayers. Cholesterol molecules were believed to induce functional domains in cellular plasma membranes called “rafts”. These “rafts” have been implicated as possibly being host templates for an entire gamut of signalling and sorting processes of the cell. Minimal model systems of ternary mixtures of sterol,

saturated lipid and an unsaturated lipid display microscopic phase separation into a liquid ordered phase l_o , and a liquid disordered phase l_d. This coexistence however is observed only below the fluidization temperature T_m of the saturated lipid. Oxysterols, like 25-hydroxycholesterol (25HC) and 27-hydroxycholesterol (27HC) , were seen to "promote" fluid-fluid coexistence with DMPC recently above T_m. Here we conduct x-ray studies on aligned multilayers and report the effect of change in acyl chain length on the extent and form of the phase boundaries of these binary systems.

In Chapter VII we probe the organization of mononucleotides in a multilamellar phospholipid matrix. Recent reports have indicated that evolutionarily fundamental RNA-like polymers, are produced through guided polymerization involving a condensation of proximal mononucleotides. The encasement of these within a lipid stack is thought to favour and enhance this process. Here we study mixtures of mononucleotide , 5'-adenosine monophosphate (AMP) and DMPC lamellae. On the basis of our experiments on aligned multilayers of this system we show that it exhibits a two phase lamellar coexistence region involving a phase with AMP adsorbed on the bilayers over a wide range of temperature. Further we study the effect of AMP on DMPC bilayers using Cryo-SEM imaging technique.

Chapter VIII provides a brief summary of the main results of this thesis and discusses a few directions for further studies.

Contents

Chapter 1

Introduction

In this chapter we give a brief introduction to the soft-matter assemblies considered, and the experimental methods used to study them in this thesis. We start by discussing polyelectrolytes and their complexation with surfactants which result in different forms of ordered aggregates. We give a gist of the directing principles of self-assembly of surfactants and lipids. We then give a perspective into the established trends and methods in the study of the phase behaviour of these amphiphilic molecules. The tunability and adaptability of lipid bilayer assemblies, and their response to doping with smaller molecules are discussed next. Finally, we layout the specifics of the experimental techniques employed by us to probe and determine the structure of a selection of systems of the above types studied in this thesis.

1.1 Polyelectrolytes and Polyelectrolyte Complexes (PEC)

Polyelectrolytes are polymers, that in bulk solution dissociate ionizable groups along their chain and behave as charged polyions [1]. The long-range nature of coulombic forces now govern their behaviour. The degree of dissociation can vary and be varied through the nature of the ionizable group through suitable modifications. Biologically relevant polyelectrolytes, like nucleic acids (DNA and RNA), polypeptides, polysaccharides and polyampholytes exploit the delicate interplay between electrostatics and entropy to exist in different bio-relevant macromolecular states.

1.1.1 Polymers in solution

Polymers in solution behave as rigid rods at small length scales but over longer lengths they behave as flexible chains. The simplest model to describe this generic behaviour is the worm-like chain model(WLC) [2]. The polymer is pictured as an elastic filament in the Hookean regime subject to thermal fluctuations. A polymer can be modelled as being a string of N segments each of length l, such that the total contour length is L=Nl. In this model the free energy of the polymer chain is given by

$$\frac{\mathcal{H}}{k_B T} = \frac{\xi}{2} \int_0^L \left(\frac{\partial \hat{t}(s)}{\partial s} \right)^2 ds \tag{1.1}$$

where $\hat{t}$ is the unit tangent vector given by $\frac{\partial \hat{r}(s)}{\partial s}$ where r(s) is the position vector of the polymer chain and s is measured along the contour. ξ is the persistence length and serves as the characteristic length scale over which two tangent vectors along the polymer remain correlated. The persistence length clearly considers short-range interactions giving stiffness and excludes long-range interactions [3]. The typical values for ssDNA is ξ_{ssdna}=1.3nm and for dsDNA it is roughly ξ_{dsDNA}=50nm due to hydrogen bonding between base pairs [4].

In the case of polyions the behaviour is markedly different from that of neutral polymers. This is due to the counterions, which leave the parent macromolecule and give rise to a large osmotic pressure in low salt conditions. The mechanical response of the polyelectrolyte is also as a result markedly different. The counterions in bulk screen electrostatic interactions through the formation of a Debye layer. The polymer stiffness is also decided by the Debye length $\lambda = \frac{1}{\sqrt{4\pi c f l_B}}$, where c is the monomer concentration, f is the fraction of ionized monomers and l_B=$\frac{e^2}{4\pi\epsilon_o\epsilon_r k_B T}$ is the Bjerrum length. l_B is the separation between two elementary charge at which the electrostatic interactions are comparable to the thermal energy $k_B T$. In water at T=298K l_B ~0.71nm for dsDNA. For polymers made of monomers of length *"a"* the electrostatic contribution to the persistence length was noted to scale as λ^2/a [5, 6]. A quantitative criterion that distinguishes between the limits of flexible and rigid chains has also been established [7].

A large fraction of counterions lie within a finite volume in close proximity of the polyion, and do not contribute to the osmotic pressure of the system. This phenomenon is known as the Oosawa-Manning condensation [8, 9]. The principle behind it can be

captured by setting a dimensionless Coulomb coupling strength γ=l_B/l$_c$ where l_c is the distance between neighbouring charge monomers. If γ is larger than unity then counterions would condense back onto the polyion and reduce it's effective charge such that γ reduces to unity. The condensed counterions are not tightly bound back to their sites but are delocalized close to to the polyion [10]. This phenomenon results from the competition between the electrostatic energy of the counterions and their entropy. For many biopolyelectrolytes this phenomenon is relevant since the separation between neighbouring charge monomers is less than the Bjerrum length of 0.7nm in water.

1.1.2 Self assembly of Surfactants

Surfactant molecules are an amalgam of two parts [11], a polar head group and a hydrocarbon chain that is covalently linked to it. Figure 1.1 shows the structure of the surfactants considered in this thesis. In an aqueous medium, a hydrocarbon chain tends to order water molecules into a "cage"like structure. The resulting increase in the orientationally dependent hydrogen bonds between water molecules makes this state highly unfavourable entropically. The interplay between this "hydrophobicity" [12] of the hydrocarbon tail and the affinity of the polar head group drives self-assembly, i.e. spontaneous aggregation of the molecules into aggregates. Single chain surfactants, typically form spherical micelles shielding themselves by forming a hydrocarbon core, expunging water. There is however a compromise to be struck between the loss in translational entropy of monomers and the free energy gain from being integrated into a micelle. This can now be stated in a statistical thermodynamic scheme [13]. The chemical potential of a molecule in an N-mer can be defined as ,

$$\mu_N = \mu_N^0 + \frac{k_B T}{N} log \frac{X_N}{N} \tag{1.2}$$

where μ_N^0 is the internal free energy of a molecule in the aggregate,

X_N is the mole fraction of monomers in all aggregates of size N. The total monomer mole fraction $X = \sum_{N=1}^{\infty} X_N \ll 1$, since we are considering a dilute solution.

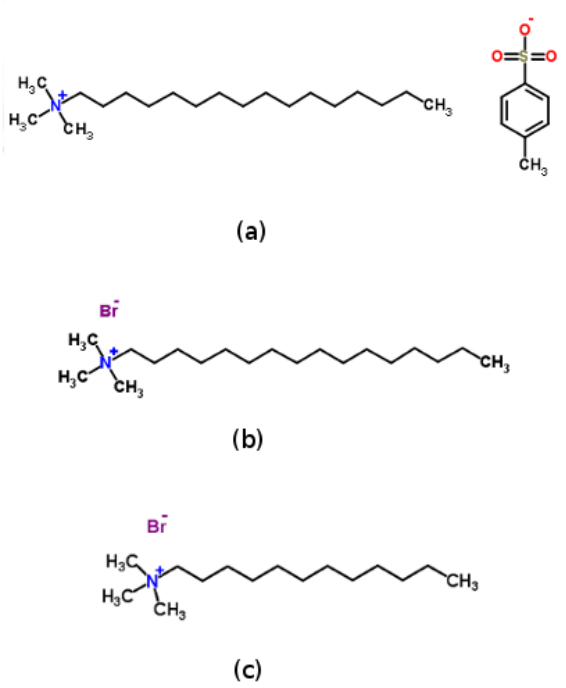

FIGURE 1.1: Structure of the surfactants studied in this thesis. **(a)**cetyltrimethylammonium tosylate, **(b)**cetyltrimethylammonium bromide and **(c)** docecyltrimethylammonium Bromide

The second term in the above equation arises to account for the entropy of mixing. Chemical equilibrium dictates that the chemical potential of a molecule be identical across all N.

$$\mu_1^0 + \frac{k_B T}{1} log \frac{X_1}{1} = \mu_2^0 + \frac{k_B T}{2} log \frac{X_2}{2} = ... = \mu_N^0 + \frac{k_B T}{N} + log \frac{X_N}{N} \tag{1.3}$$

Therefore,

$$\frac{X_N}{N} = X_1(exp[\frac{\mu_1^0 - \mu_N^0}{k_B T}]) \tag{1.4}$$

or,

$$X_N = N X_1 exp(\alpha); \alpha = \frac{\mu_1^0 - \mu_N^0}{k_B T}. \tag{1.5}$$

For an aggregate of size N the condition $\mu_N^0 < \mu_1^0$ should be satisfied. In the extremely dilute limit monomeric suspensions are favoured, i.e. $X_1 \ll 1$,$X_1 e^{\alpha} < 1$ imply $X_N \ll X_1$ and $X \sim X_1$. Increasing the surfactant concentration further pushes $X_1 e^{\alpha}$ towards unity and since $X_N < 1$, the limiting value of monomer concentration plateaus at $X_1 \sim e^{-\alpha}$. This concentration is known as the critical micellar concentration(CMC), above which aggregates form while holding the monomer concentration at near constancy.

$$CMC = (X)_c \approx (X_1)_c \approx e^{\frac{\mu_1^0 - \mu_N^0}{k_B T}} \tag{1.6}$$

Typical values of CMC for single chained surfactants, like cetyltrimethylammoniumbromide(CTAB) is $\sim 10^{-3}$M and for double-chained lipids, like dipalmitoylphophatidylcholine(DPPC), it is $\sim 10^{-9}$M. The experimental estimation of CMC is done using an array of techniques measuring responses such as turbidity,osmotic pressure and surface tension. The physical parameters display a steady behaviour below CMC and show an abrupt change near CMC resembling a first order phase transition (Figure 1.2).

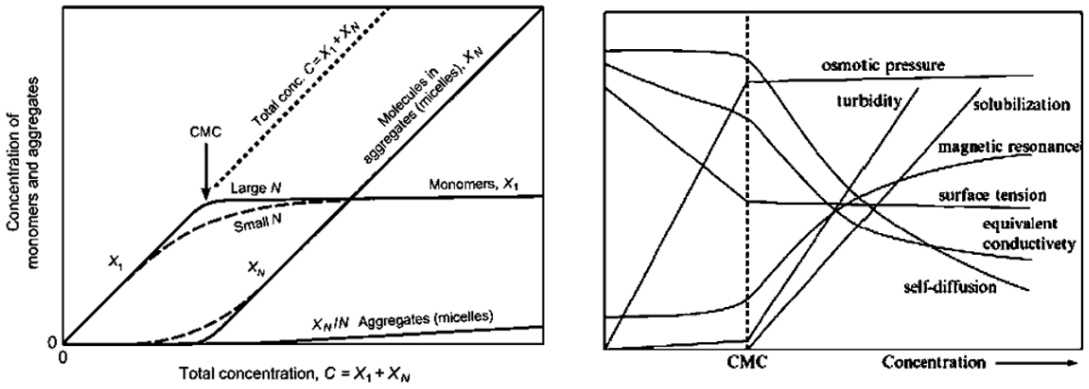

FIGURE 1.2: (a)Monomer(X_1) and aggregate(X_N) concentrations as a function of total concentration; (b)Schematic representation of response of some physical properties of surfactant solutions across CMC, [11]

1.1.2.1 Shape, dimensionality and growth of micelles

Micelles of varied shapes and sizes form based on the nature of the constituent amphiphiles. However, the governing feature common to all aggregates is the extent of their hydrophobic core. Since holes within the core are energetically unfavourable the

diameter of a spherical aggregate cannot exceed $2l$, where l is the length of the fully stretched hydrocarbon tail. This implies that at least one dimension of the aggregate is of the order of l. Therefore, there can be globular aggregates (with all 3 dimensions of order l), rod-like aggregates (2 dimensions are of order l) and bilayers (1 dimension is of order l).

The packing parameter gives an elegant scheme to determine the geometry of micelle. It is defined as,

$$p = \frac{v}{al} \tag{1.7}$$

where a is the optimal headgroup area, v is the hydrocarbon chain volume and l is the chain length. The range within which the shape parameter falls gives an ideal geometry that the micelle can take [11]. Figure 1.3 gives a schematic representation of the shape parameter of amphiphiles and the preferred geometry of the aggregates they self-assemble into.

Surfactants can have different charge residues that can be used to tune the optimal head-group area. Rod-like and disk-like micelles can be systematically driven to undergo phase transitions to form "worm-like" micelles and infinitely large sheet-like aggregates, respectively. The conditions promoting such growth require that the internal free energy per molecule within the aggregate reduce with size. For example, a rod-like spherocylindrical micelle, would preferably link up with another if $\mu^0_{cyl} < \mu^0_{sph}$. The addition of salts with highly specific counter-ions has been noted to trigger growth. Similarly, disc-like micelles start out with semitoroidal edges shielding their hydrocarbon core. The energetic cost of having an edge is overcome by accretion and coalescence of smaller discs into an infinite bilayer.

1.1.3 Form and stability of PECs

PECs form when polyions of opposite charge approach each other due to long-range electrostatic interactions. The association of the large macro-ions leads to the release of previously bound counterions. The resultant gain in entropy of the released counterions stabilizes the assembly. The complex can even remain locked in these self-assembled

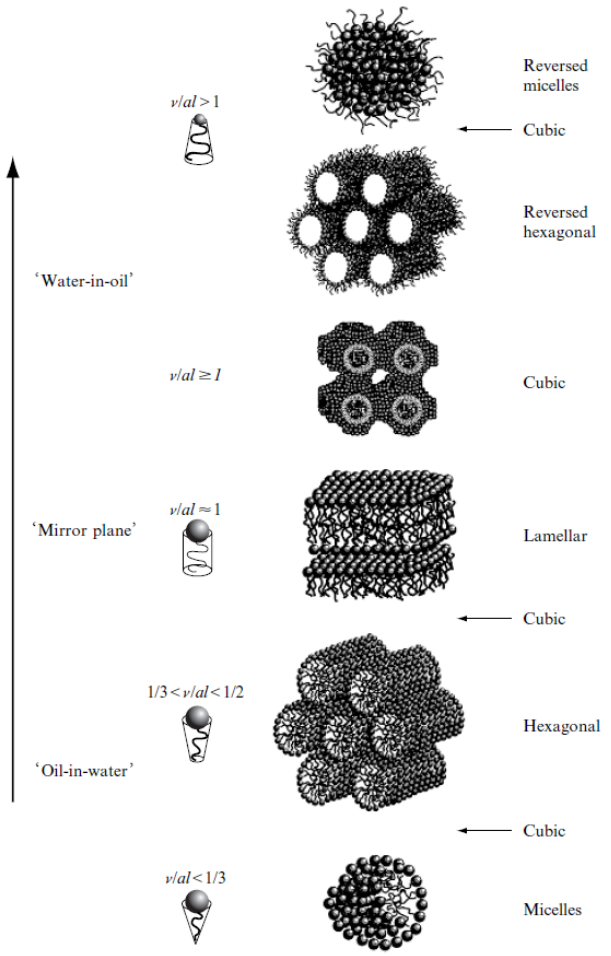

FIGURE 1.3: Shape parameters of surfactant molecules and preferred aggregate structures [14]

forms under conditions that cause overcharging and even charge reversal [15]. The addition of simple salts has been noted to have large impact on the structure through the modification of the electrostatic interactions.

The compaction of DNA and the reduction of it's charge helps overcome the cellular membrane barrier potential and promote uptake of nucleic acids [16]. Complexation with cationic lipids of specific shape is seen to increase the uptake of these "lipoplexes". Further, the release of the packaged DNA too is shown to be effected without change in native form through the addition of anionic species. The structure can be tuned through the addition of neutral helper lipids or by making the bilayer flexible [17, 18]. The structure in these cases depends on mechanical properties of the bilayer and the charge compensation mechanism between the lipid and DNA [19, 20]. Two structures

are observed in these systems: a lamellar complex where the DNA strands are sandwiched between the bilayers and the H^c_{II} where the DNA strands are confined to the cores of an inverted hexagonal phase [21]. This system shows an additional intercalated hexagonal phase. $C_{16}TA$ shows tunability in structure when complexed with DNA strands and laced with short chained alcohols [22]. Cationic lipids when complexed with actin were seen to promote polymerization of g-actin to f-actin and form novel 1-D lamellar structures [23].

Surfactants capable of forming long wormlike micelles due to the presence of strongly binding counterions or other promoters of micellar growth show a variety of columnar phases including a swollen $\sqrt{3} \times \sqrt{3}$ superlattice of the underlying H^c_I structure and a square structure [25].

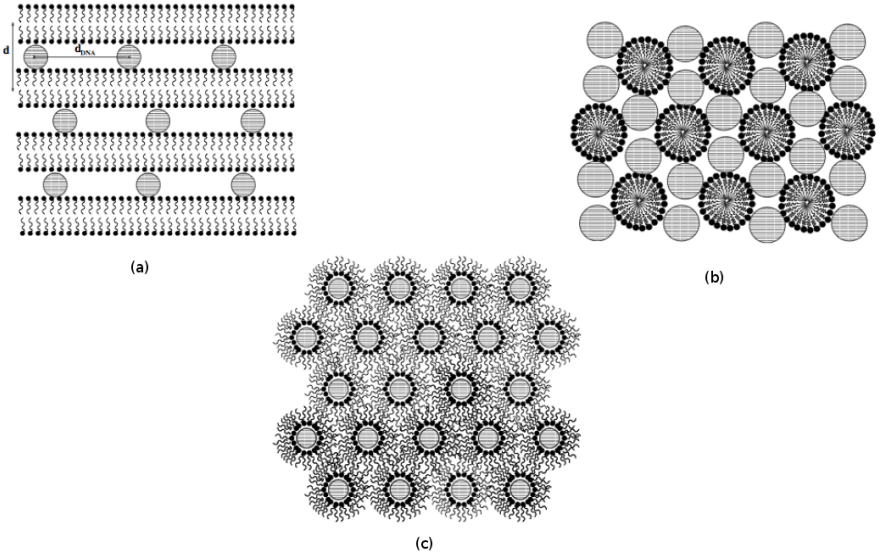

FIGURE 1.4: Polymorphism of DNA cationic surfactant complexes.
(a)L^α_c Lamellar phase with DNA sandwiched between bilayers,(b)H^c_I Intercalated hexagonal phase, (c)H^c_{II} Inverted hexagonal phase [24]

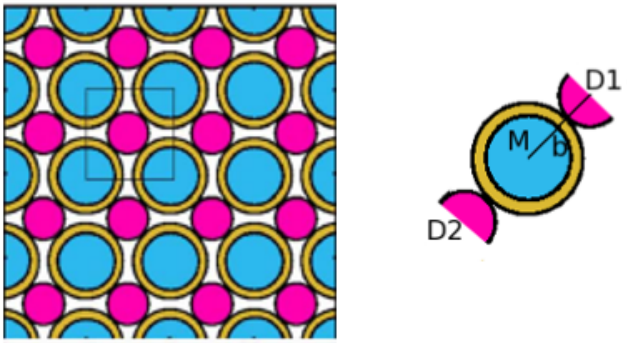

FIGURE 1.5: Square phase S^c_I and it's motif [25]

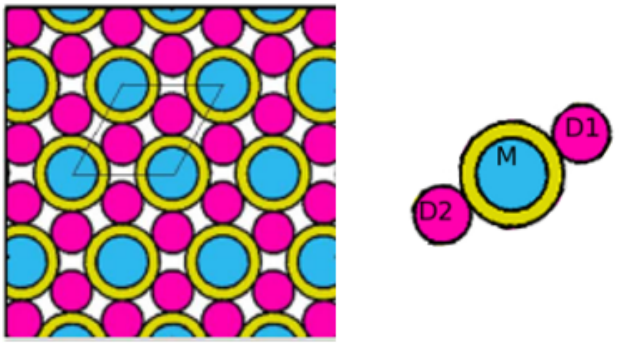

FIGURE 1.6: Hexagonal phase H^c_I and it's motif [25]

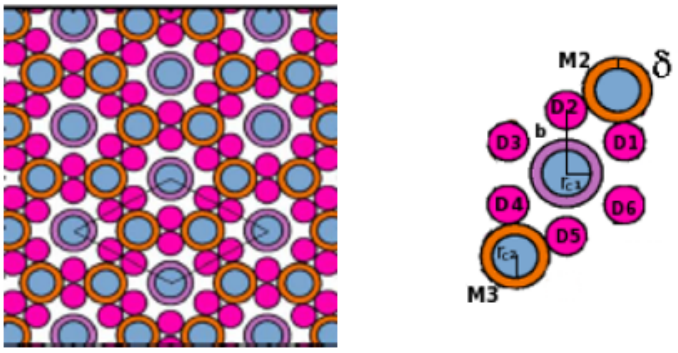

FIGURE 1.7: Superhexagonal phase and it's motif $H^c_{I,s}$ [25]

1.2 Polymorphism of Lipid bilayer systems

Bilayer forming lipids are amphiphilic molecules that consist of a polar headgroup and have typically two hydrocarbon chains [26]. The presence of the extra hydrocarbon chain as compared to single chained surfactant greatly magnifies effective hydrophobic interaction for the molecule as a whole and the CMC for lipids as a result is of the order of $\sim 10^{-9}$M. The headgroup moiety can be charged or zwitterionic, i.e. having a dipole moment when dispersed in water but possessing zero net charge. Based on the diversity of headgroups lipids can be classified into several groups such as phophatidylcholines(PCs), phosphatidylethanolamines(PEs), phosphatidylserines(PSs) and phosphatidylglycerols(PGs). Lipids of different hydrocarbon chain lengths and varying degrees of unsaturation have also been extensively studied and some are presented in Figures 1.8 and 1.9.

Cellular mechanisms that require selective compartmentalization and specificity exploit membrane properties extensively [27]. The generic picture of a cellular membrane comprises essentially a plasma membrane composed of a variety of lipids embedded with macromolecules like proteins, sterols and sugars (Figure 1.10). The production of lipids by the cell to regulate function, structure as well as interactions with other lipids, proteins and metabolites has sprung the field of lipidomics [28]. Further, regulatory processes like the transport of cargo in the cell require the packaging of material in a suitable

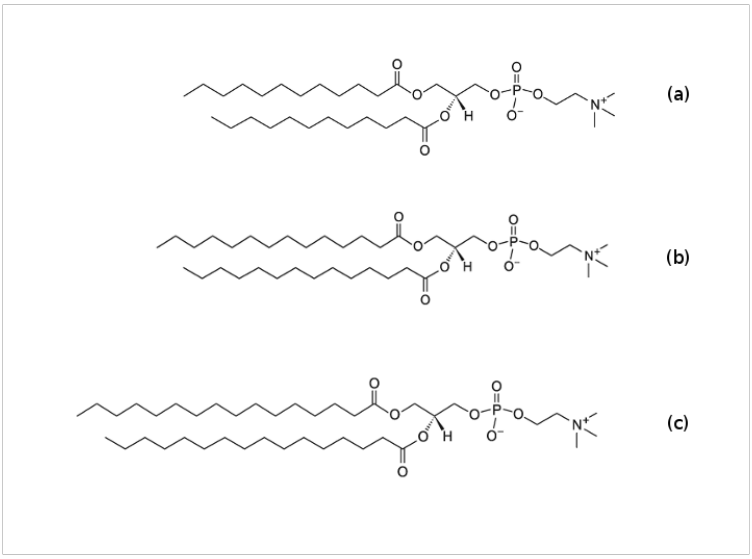

FIGURE 1.8: Structure of phosphatidylcholine lipids with different acyl chain lengths considered in this thesis.
(a)dilauryl phosphatidylcholine DLPC(12:0/12:0),(b)dimyristoyl phosphatidylcholine DMPC(14:0/14:0),(c)dipalmitoyl phosphatidylcholine DPPC(16:0/16:0)

environment. This process is done through the wrapping with a membrane and is known as vesiculation [29]. Model membrane systems help us mimic the complex cellular processes and develop a better understanding of the underlying physical features.

1.2.1 Structural polymorphism of lipid bilayer systems

In an aqueous medium lipids self-assemble into lamellae. The basic periodic unit is a bilayer with a water layer in between. They form a fluid L_α phase above a critical temperature called the main-transition temperature T_m. There is quasi long-range order along the stacking direction but along the plane of the bilayer it is a fluid [31]. T_m depends critically on the type of headgroup, hydrocarbon chain length and the degree of unsaturation in the chain. The chains are disordered and molten in the L_α phase. When they are cooled below T_m the hydrocarbon chain lock into an in-plane quasi-hexagonal lattice. They are frozen into a predominantly all trans conformation. This phase is called

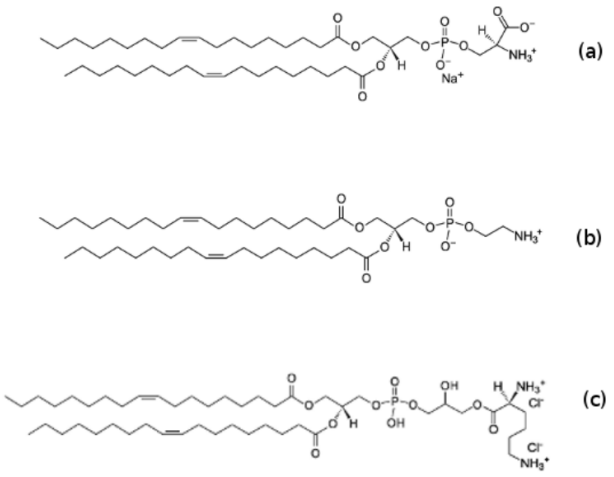

FIGURE 1.9: Structure of lipids with different headgroups.
(a)PS,(b)PE,(c)PG

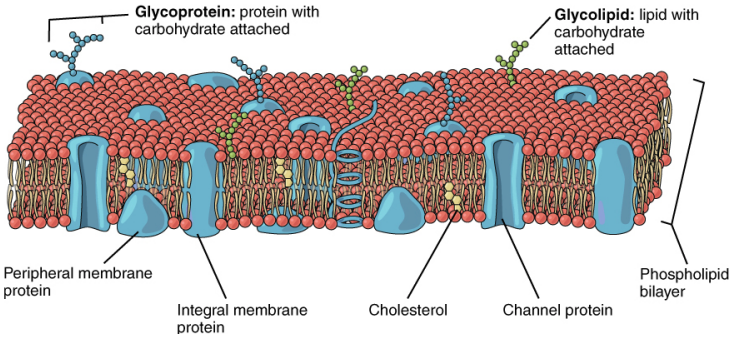

FIGURE 1.10: A schematic of the Fluid mosaic model of Cell Membranes [30]

the L_β phase. In the case of certain lipids where the headgroup area is large the chains tilt with respect to the bilayer normal. This low temperature phase is called the $L_{\beta'}$ phase. Based on variation in tilt direction three different types of gel phases have been observed [32–34]. Lipids that display this low temperature behaviour invariably display an additional intermediate phase called the $P_{\beta'}$ phase. The L_α phase shows a single set of peaks in the small-angle region along q_z, due to bilayer stacking in the z-direction. A diffuse peak is observed in the wide angle region from the molten chains. The $L_{\beta'}$ phase also shows prominent peaks along q_z corresponding to a 1-D lattice. In this case sharp peaks are seen in the wide-angle region arising from the chain lattice. The ripple phase arises from the coupling of the tilt field to the height field. This gives rise to a 1-D modulated phase that is characterized by a two-dimensional oblique lattice. Figure 1.11 shows the characteristic diffraction patterns observed accompanied by a schematic of their structure.

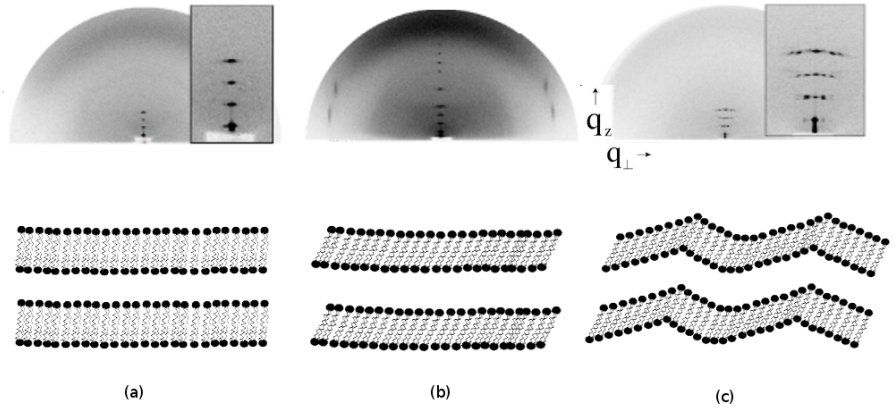

FIGURE 1.11: Characteristic diffraction patterns of aligned lipid bilayers and their shematic representations.
(a)L_α (b) $L_{\beta'}$ (c) $P_{\beta'}$.Image adapted from [35, 36].

1.2.2 The effect of sterols on lipid membranes

Sterols are lipids that are comprised of a small hydrocarbon chain attached to a bulky polycyclic steroid core. The presence of sterols is known to change the mechanical characteristics of the bilayer. This in turn is exploited heavily by a slew of cellular processes

involving sorting, compaction, signalling etc. Cholesterol, is a extremely important molecule and has been the subject of extensive studies [37]. Cholesterol enriched domains called "rafts " were hypothesized to be present in plasma membranes acting as functional platforms for a host of processes. However, their formation and function is still not well established. Recent super-resolution imaging measurements have however detected the presence of nanoscale heterogeneities in certain cell lines [38].

Ternary mixtures of cholesterol and a combination of unsaturated and saturated lipids show micron sized domains that mimic those proposed by the "raft" hypothesis [39, 40]. The observations bear striking similarities with other measurements done on Giant Plasma Membrane vesicles [41]. Figure 1.12 collates the observations from a variety of experimental techniques measuring the behaviour of binary PC-cholesterol mixtures. It is to be noted that above T_m spectroscopic studies show a coexistence between a liquid ordered phase(l_o) and a liquid disordered phase(l_d). However, X-ray scattering methods have not detected such behaviour.

Sterols of various types are known to form and get regulated by different cells as a response to a host of triggers [46]. Oxysterols are oxygenated derivatives of sterol that can form through enzymatic action and non-enzymatic mechanism. Synthesis routes in both cases are seen to be highly selective in the location on the cholesterol molecule that is oxygenated. In contrast to cholesterol, 25-hydroxycholesterol and 27-hydroxycholesterol (both side-chain derivatives formed through enzymatic action) , were seen through scattering methods, to promote fluid-fluid coexistence above the T_m of lipid matrix they were embedded in [47, 48]. Molecular dynamics studies have indicated that these molecules can remain in different orientations in the bilayer [49].

1.3 Experimental techniques

In this section we describe the experimental techniques used to study the different classes of systems considered in this thesis. The methods used to extract and analyze the x-ray diffraction data in different sample geometries are presented. We also setup the details of the elemental analysis technique used specifically for the calculation of the stoichiometric ratios of PECs. Finally, we provide the specifics of the Cryo-SEM measurements that were undertaken.

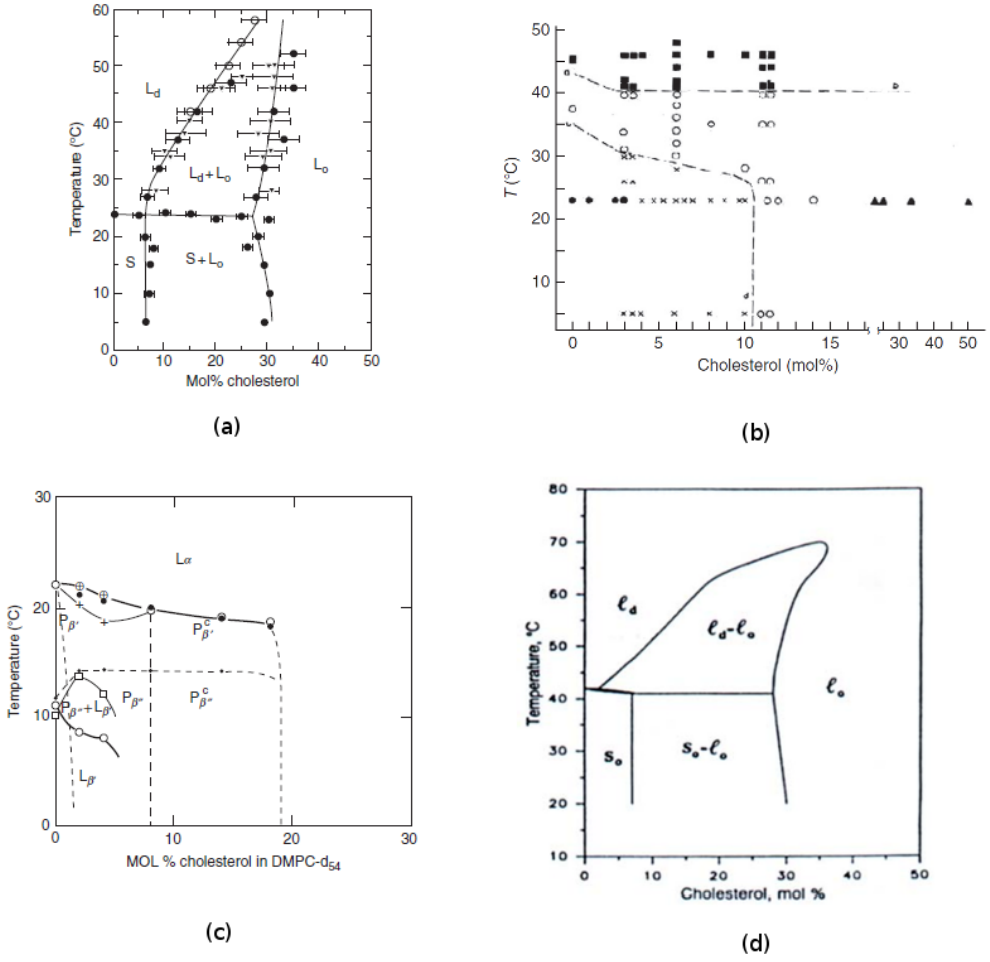

FIGURE 1.12: Partial phase diagrams of binary mixtures of PC lipid and Cholesterol. (a)NMR Studies [42] (b)x-ray scattering [43] (c)Neutron scattering [44] and (d)Theoretical models [45]

1.3.1 Principles of X-ray diffraction

Scattering studies involve the irradiation of the sample with a well collimated beam of light. The scattered intensity varies as a function of the angle between the incoming and the scattered beam. From Bragg's law, we infer that any scattered intensity at an angle 2θ results from a fluctuation or inhomogeneity in the sample with periodicity d $=\lambda/2\ \sin\theta$. X-rays have a short wavelength($\sim 1-10$ Å) and scatter off the electrons in the irradiated material. The density modulations of the structure under the First Born approximation can be obtained from the scattered intensity pattern. The large angle part of the diffraction pattern gives a readout of the structure at the atomic length scale

(WAXS) and the small angle region can be studied to elucidate structure at the colloidal length scale (SAXS).

1.3.1.1 Theory of X-ray diffraction

The density modulations in electron density $\rho(\vec{r})$ of a structure can be expressed as a convolution of a lattice function $\rho_l(\vec{r})$ which describes the lattice type on which the basic repeating units (motifs) are ordered, and a basis function $\rho_b(\vec{r})$ describing the electron density of the motif, i.e.,

$$\rho(\vec{r}) = \rho_l(\vec{r}) \circledast \rho_b(\vec{r}) \tag{1.8}$$

The Fourier transform of the above equation gives,

$$f_{structure}(\vec{q}) = f_l(\vec{q}) f_b(\vec{q}) \tag{1.9}$$

where, $\vec{q}$ is the scattering vector whose magnitude is given by q =$4\pi\sin\theta/\lambda$. f_l and f_b are the Fourier transforms of ρ_l and ρ_b, respectively.

The intensity of the scattered radiation, relative to that scattered by a single electron, is given by

$$I(\vec{q}) = |f_{structure}(\vec{q})|^2 = s(\vec{q})|f(\vec{q})|^2 \tag{1.10}$$

where

$$s(\vec{q}) = |f_l(\vec{q})|^2 \tag{1.11}$$

$s(\vec{q})$ and $f(\vec{q})$ are called the structure factor and form factor, respectively. The form factor contains a description of the "form" of the individual scatterer or motif and the structure factor bears the information on the arrangement or positions of the scatterers with respect to each other. A thorough and pedagogical review of the subject of x-ray scattering can be sought here [50–52].

Bilayer-water systems are smectic liquid crystals where long-range crystalline order is destroyed by long-wavelength fluctuations. They display quasi-long range order, characterised by power-law decay in positional correlations [53]. As a result only a few Bragg reflections are obtained in the fluid phase at full hydration. The Paracyrstalline theory(PCT) and the Caillé theory address the interpretation of scattering data from these systems. The PCT tackles the issue of thermal and lattice disorder within a stochastic approach known as stacking disorder [54]. Caillé theory further takes into account local molecular fluctuations that result in the undulation of the bilayers based on a Hamiltonian model [55]. In this thesis we construct the electron densities for the bilayers based on the method prescribed in [56].

1.3.1.2 Electron Density Profiles of bilayers by Fourier reconstruction method

The electron density of a lipid bilayer is expressed as [57],

$$\rho(z) = \rho_w + \frac{F(0)}{d} + \frac{2}{d}\sum_{h=1}^{h_{max}} \alpha_h |F_h| Cos[\frac{2\pi h z}{d}] \tag{1.12}$$

where ρ_w is the electron density of water, d is the lamellar periodicity, F_hs are the magnitudes of form factor at $q_h = \frac{2\pi h}{d}$ and $F(0)$ is the zero order form factor. α_hs are the phases of the Fourier components. The intensities give a direct readout as

$$F_h = C_h \sqrt{I_h} \tag{1.13}$$

where I_h is the intensity of the h^{th} order reflection and C_h the correction factor that takes into account the scattering geometry and sample morphology. The scattering experiments yield only the absolute ratios $r_h = \frac{F_h}{F_1}$ as we need to account for the unknown scaling factor in F_h. The electron density profile on a relative scale now reads

$$\rho(z)_{rel} \propto \sum_{h=1}^{h_{max}} \alpha_h r_h Cos[\frac{2\pi h z}{d}] \tag{1.14}$$

The readout of the intensities gives $I = |F_h|^2$, but F_h is in general a complex quantity. This requires the phase to be established accurately. The allocation of the correct phase

to the diffraction peaks is known as "phase problem in crystallography". In general the phase can take arbitrary values. However, if the motif is centro-symmetric and the origin is taken to be at the centre of symmetry α_h has only two possible values 1 and -1. This is the case for the lipid bilayer when we describe it with respect to the centre of the bilayer rendering it an even function. This narrows the resolution of the structure down to finding the phase allocation sequence for n diffraction peaks from among 2^n possibilities. The combination giving the correct electron density profile with four orders of diffraction is invariably (- - + -) for phospholipid bilayers.

Phase retrieval can be performed in different ways. Controlled swelling forces the lamellar sheets to sample the form factor at different points by changing the water layer thickness but preserving the bilayer structure [58]. When the number of reflections are few (3-4), a brute force algorithm that assigns all 2^n combinations can be tested. The form of the electron density profile that is most physically meaningful is recognized as the accurate one.

Another scheme for phase retrieval, that we follow in this thesis is described in [56]. The electron rich headgroups either leaflet are assigned a Gaussian function and the electron deficient terminal methyl group is assigned another as depicted in Figure 1.13. The electron density profile can now be written as

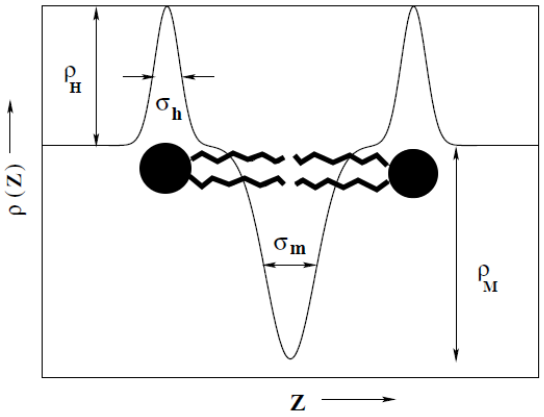

FIGURE 1.13: Schematic diagram of three Gaussian model describing trans-bilayer profile;
where ρ_h and σ_h are the height and width of the Gaussian defining the headgroup region and ρ_m and σ_m are the height and width of the Gaussian defining the terminal methyl region

$$\rho(z) = \rho_h[e^{\frac{-(z+x_h)^2}{2\sigma_h^2}} + e^{\frac{-(z-x_h)^2}{2\sigma_h^2}}] - \rho_m e^{\frac{-z^2}{2\sigma_m^2}} \tag{1.15}$$

where ρ_h and σ_h are the height and width of the Gaussian defining the headgroup region and ρ_m and σ_m are the height and width of the Gaussian defining the terminal methyl region. The Fourier transform of the model is found to be

$$F_T(q) = \sigma_m \rho_m [\frac{2\rho_h \sigma_h}{\rho_m \sigma_m}(e\frac{-q^2\sigma_h^2}{2} Cos[q_z x_h]) - e\frac{-q^2\sigma_m^2}{2}] \tag{1.16}$$

The observed data is compared with the data generated from this model keeping x_h, σ_m, σ_h and $\frac{\rho_h}{\rho_m}$ as the adjustable fit parameters. The convergence to the best fit values generates the correct set of phases. Thereafter, using Equation1.14 the electron density profile is obtained.

1.3.1.3 Experimental Setup and Data refinement

In this thesis, we have used two different sample morphologies to probe the structure. Unoriented samples were loaded in glass capillaries (Hampton Research) and sealed to prevent evaporation. The experiments were conducted in the Hecus S3-Micro small angle scattering system with a 1-D position sensitive detector (PSD). The unit comprises a built-in Peltier element temperature control system that can be tuned between 5°C and 80°C.

For oriented samples, a home-built heater was used. The control of temperature is effected through the circulation of water through the chamber from a water bath (Julabo). The chamber is sealed with a reservoir of water placed inside to achieve constant relative humidity which is monitored through a thermo-hygrometer (Testo 610). The inlet and outlet windows were covered with thin mylar sheets to prevent additional scattering. To maintain uniform humidity within the chamber the air inside was circulated using a small fan. A schematic representation of the chamber is depicted in Figure 1.14. Further hot air is blown gently on the mylar sheets to prevent condensation due to thermal gradients between the chamber and the ambient. A sealed-tube x-ray generator Genix3D(Xenocs) operating at 50 kV and 0.60 mA was used as the laboratory source. A multi-layered mirror was used to select the CuK_α line (λ=1.54Å). The beam is then

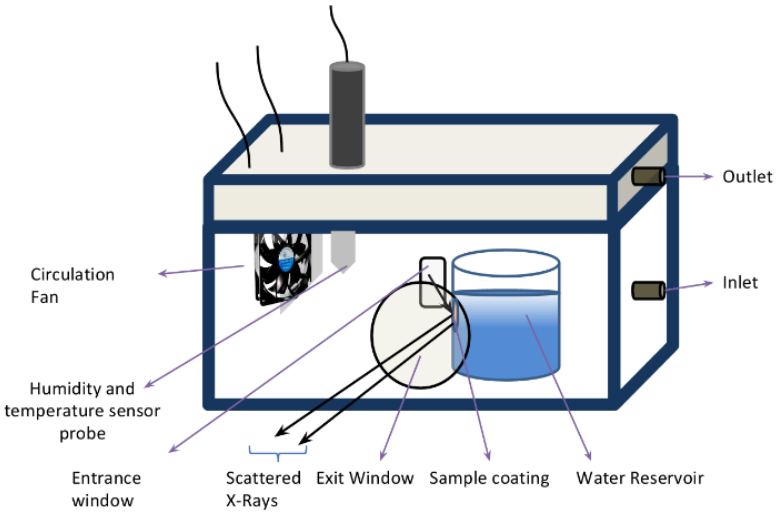

FIGURE 1.14: Schematic diagram of the temperature controlled chamber for aligned samples

guided through scatter-less slits (Xenocs) to obtain optimum beam size while minimizing parasitic scattering. Patterns were recorded on a 2D image plate detector MAR345 (Marresearch). The pixel size of 100μm was chosen. The sample to detector distance is varied to suit experimental needs. The sample to detector distance was measured using the small-angle standard silver behenate (d=58.38Å).

The diffraction pattern for oriented bilayer samples correspond to a set of peaks along q_z from the lamellar periodicity and give rise to additional peaks at $q_\perp \neq 0$ when bilayers display modulated phases. By indexing onto a two dimensional lattice the lattice parameters can be measured. The integrated intensity is obtained by encasing all high intensity pixels of the spot within a rectangular box parallel to $q_\perp$ and q_z. I(q) versus q was obtained by integrating along one of the edges of the box after background subtraction. The background was assumed to be linear across the extent of each peak. Intensity corrections for peaks along q_z and $q_\perp$ take into account the sample morphology and mosaicity. The reflections along q_z are corrected to

$$I_c = I_o \frac{2\pi\Delta}{\lambda} Sin[2\theta] \tag{1.17}$$

and for the satellite peaks to

$$I_c = I_o \frac{4\pi^2}{\lambda_r} |k| \tag{1.18}$$

where Δ is the sample mosaicity and is estimated to be about 10° [35], k is the Miller index of the corresponding satellite peak and λ_r is the wavelength of the in-plane modulation. Since the beam travels through the curved sample an absorption correction is to be done. The inability to accurately estimate the thickness of sample in our case makes the above not viable. However, previous studies have shown that the electron density maps are not affected much by absorption correction [35].

The peaks are also corrected for multiplicity of equivalent planes. For example in the case of a 2-D hexagonal lattice the [21] reflection has 12 equivalent planes whose intensities overlap at the same q, whereas the [10],[11] and [20] peaks have only 6 equivalent planes. Since we consider only relative intensities of the peaks we divide the intensity of the [21] peak by two.

1.3.2 Cryo-SEM imaging Technique and Protocol

Cryogenic Scanning Electron Microscopy (Cryo-SEM) imaging provides powerful high resolution images of surfaces of samples containing moisture without causing structural changes related to dehydration. The resolution of the technique is of the order of 1nm. size. In the field of material science this technique has been extensively used to probe a wide range of physical systems ranging from ceramic particle suspensions [59], to porosity measurements in clays to refine models of transport [60] and to study the aggregation of pigments in wet and dried paints [61]. Ultra-structural imaging of biological samples has also been performed with the added benefit of volume imaging [62].

Cryo-SEM imaging was carried out on a Zeiss,ULTRA PLUS scanning electron microscope with a cryo preparation system PP3000T, Quorum Technologies. The sample was mounted on a rivet and placed on a shuttle that has a coating of conductive glue to allow discharge of electrons. The holder is then attached to a transfer rod that is plunged in liquid nitrogen to flash freeze the sample. The sample is then retracted into a containing unit that couples with the vacuum cryo-unit. The shuttle is now extended into the cryo-chamber where moisture from the sample is sublimated. The sample is then cleaved with an attached knife edge and sputter coated with a thin layer of platinum to effect good conductance. The sample is then finally introduced into the observation chamber and docked. Throughout this process the temperature is maintained below

-160°C and to avoid contamination due to formation of ice crystals cold traps are set-up and maintained at $\sim$ -190°C.

The interaction of the electron beam with the sample is of two fundamental types elastic and inelastic scattering. Inelastic scattering involves the ionization of the sample due to excitation and generation of mostly secondary electrons(SE) along with Auger electrons and characteristic x-rays. Elastic scattering off the atomic nucleus or outer shell electrons of the sample occur without transfer of energy. The fraction of incident electrons elastically scattered through an angle of more than 90° is referred to as back scattered electrons (BSE). The energy rating of the beam can be tuned from 0.4 to 1keV. SE imaging provides greater lateral resolution over BSE imaging and they are acquired through an in-lens detector. The sample is raster scanned and SE are collected and rendered to generate surface features at high resolution.

1.3.3 Elemental analysis and method of estimating Stoichiometric ratio of PECs

Carbon, hydrogen, nitrogen, oxygen and sulphur are the basic elements of organic living matter. Elemental combustion analysis is a technique that identifies and quantifies the composition of an unknown sample based on the amount of combustion products collected through high temperature decomposition. The method has long been used by chemists to establish purity and the chemical nature of intermediate and final products when complemented with mass spectrometry and NMR data.

1.3.3.1 Experimental Setup and protocol of experiment

The trials in our case were conducted in a CHNS elemental analyzer , vario MICRO cube (elementar). The method involves weighing a known amount of sample in a tin boat. The sample is then lowered into an auto-sampler drum that has a stream of helium flowing through that is regularly enriched with pure oxygen. Complete oxidization of the sample is then carried out at the combustion reactor. The product in gaseous form is then passed over copper to reduce the nitrogen oxides to elemental nitrogen. This is finally separated in a chromatographic column and relative amounts of C,H,N and S is determined. For our experiments PECs were made at the suitable composition ratios under consideration

and the entire complex is transferred into tin boats, post equilibration. The samples are then dried thoroughly by placing in an evacuated dessicator for 3 days. The samples are then removed and crimped immediately to avoid rehydration. Small amounts of trapped moisture are known to produce inconsistencies in measurements and care was taken to avoid any contamination. The determination of amount of sample and ensuring complete dessication was done through repeated weighing in an ultra-microgram weighing balance (Sartorius).

1.3.3.2 Method to calculate stoichiometric ratio of PECS

Elemental analysis of PECs gave the total C,N and S content (weights) of the complex consisting of polyelectrolyte, surfactant and condensed counterions. The weights of the different elements obtained from the experiment are converted into moles using the appropriate atomic weights. The contribution to total number of carbon, nitrogen and sulphur from the complex can be expressed as

$$N_{carbon} = xN_s + yN_b + zN_{ion} \tag{1.19}$$

$$N_{nitrogen} = N_s + \alpha N_b \tag{1.20}$$

$$N_{sulphur} = N_{ion} \tag{1.21}$$

where, x, y and z are the number of carbons in each surfactant, base and counterion and α is the number nitrogen atoms in one base of DNA. N_s, N_b and N_{ion} are the total number of surfactant molecules, bases and condensed counterions in the sample, respectively.

Recasting the above equation in terms of number ratios, $\frac{N_{carbon}}{N_{nitrogen}} and \frac{N_{sulphur}}{N_{nitrogen}}$ we get

$$\frac{x + yn_r}{1 + \alpha n_r} = \frac{N_{carbon}}{N_{nitrogen}} - z\frac{N_{sulphur}}{N_{nitrogen}} \tag{1.22}$$

where $n_r = \frac{N_b}{N_s}$ is the number ratio between base to surfactant in the PEC.

The calf thymus DNA used is of the B-form and is known to have a ratio of 41.9% of A-T base pairs and 58.1% of G-C base pairs [63], giving an effective contribution of 19.581 carbon atoms and 7.419 nitrogen atoms per base.

The CTA^+ surfactant ion, tosylate counterion(Figure 1.1,(a)) and the DTA^+ surfactant ion (Figure 1.1,(c)) have empirical formulae of $C_{19}H_{42}N$,$C_7H_7O_3S$ and $C_{15}H_{36}N$, respectively. The presence of sulphur is therefore solely from the tosylate counterion. In 1.22 parameters x, y, α and z are obtained from the structural formula of the constituents. The number of different atoms is obtained from the experiment, allowing the estimation of n_r.

Bibliography

[1] M. Doi and S.F.Edwards, *Theory of Polymer Dynamics*, Clarendon Press, New York(1986).

[2] M. Rubinstein and R. H. Colby, *Polymer Physics*, OUP, Oxford (2003).

[3] A. R. Khoklov and A. Y. Grosberg, *Statistical Physics of Macromolecules*, AIP Press, New York (2002).

[4] J.N.Milstein and J. C. Meiners, *Encyclopedia of Biophysics*, Springer-Verlag, Berlin (2013).

[5] T. Odijk, *Macromolecules*, **12**, 688 (1979).

[6] T. Odijk, *J. Phys. Chem.*, **93**, 3888 (1989).

[7] J. L. Barrat and J. F. Joanny, *Europhys. Letters*, **24**, 333 (1993).

[8] F. Oosawa, *J.Polymer Sci.*, **23**, 421 (1957).

[9] G. S. Manning, *J. Chem. Phy.* , **51**, 3249 (1969).

[10] U. Mohanty, B .W. Ninham and I. Oppenheim, *Proc. Natl. Acad. Sci., U. S. A.*, **93**, 4342 (1996).

[11] J. N. Israelachvili, *Intermolecular and Surface forces*, Academic Press, London (1991).

[12] C. Tanford, *The Hydrophobic effect*, 2nd ed., Wiley, New York (1980).

[13] A. Ben-Shaul and W. M. Gelbart in *Micelles, Membranes, Microemulsions and Monolayers*, Eds. W. M. Gelbart,A. Ben-Shaul and D. Roux, Springer-Verlag, Berlin (1980).

[14] K. Holmberg, B. Jonsson, B. Kronberg, B. Lindman, *Surfactants and Polymers in Aqueous Solution*, 2nd ed. Wiley, West Sussex (2003).

[15] R. S. Dias, R. Svingen, B. Gustavsson, B. Lindman, M. G. Miguel and B. Akerman, *Electrophoresis*, **26**, 2908 (2005).

[16] D. D. Lasic, *Liposomes in drug delivery*, CRC Press, Boca Raton, FL (1997).

[17] J. O. Radler, I. Koltover, T. Salditt and C. R. Safinya, *Science*, **275**, 810 (1997).

[18] D. D. Lasic, H. Strey, M. C. A. Stuart, R. Podgornik and P. M. Frederik, *J. Am. Chem. Soc.*, **119**, 832 (1997).

[19] K. Wagner, D. Harries, S. May, V. Kahl, J. O. Radler and A.Ben-Shaul, *Langmuir*, **16**, 303 (2000).

[20] S. May, D. Harries and A.Ben-Shaul, *Biophys. J.*, **78**, 1681 (2000).

[21] I. Koltover, T. Salditt, J. O. Radler and C. R. Safinya, *Science*, **281**, 78 (1998).

[22] R. Krishnaswamy, G. Pabst, M. Rappolt, V. A. Raghunathan and A. K. Sood, *Phys. Rev. E*, **73**, 031904 (2006).

[23] G. C. Wong, J. X. Tang, Y. Li, P. A. Janmet and C. R. Safinya, *Science*, **288**, 2035 (2000).

[24] R. Krishnaswamy, V. A. Raghunathan and A. K. Sood, *Phys. Rev. E*, **69**, 031905 (2004).

[25] A. V. Radhakrishnan, S. K. Ghosh, G. Pabst, V. A. Raghunathan and A. K. Sood, *Proc. Natl. Acad. Sci., U. S. A.*, **109**, 6394 (2012).

[26] D. M. Small, *Handbook of Lipid Research Series*, **4**, Plenum Press, NY (1986).

[27] R. Lipowsky and E. Sackmann, ed. Handbook of Biological Physics Volume I, Elsevier Science B. V (1995).

[28] X. Han, *Nature Rev. Endocrin.*, **12**, 668 (2016).

[29] H. Hauser, *Proc. Natl. Acad. Sci., U. S. A.*, **86**, 5351 (1989).

[30] S. J. Singer and G. L. Nicholson, *Science*, **175**, 720 (1972).

[31] P. M. Chaikin and T. C. Lubensky, *Principles of Condensed Matter Physics*, C.U.P., Cambridge (1995).

[32] G. S. Smith, E. B. Sirota, C. R. Safinya, R. J. Plano and N. A. Clark, *J. Chem. Phys.*, **92**, 4519 (1990).

[33] S. T. Nagle, Y. Liu, J. Legleiter and J. F. Nagle, *Biophys.J.*, **83**, 3324 (2002).

[34] V. A. Raghunathan and J. Katsaras, *Phys. Rev. Lett.*, **74**, 4457 (1995).

[35] K. Sengupta, V. A. Raghunathan and J. Katsaras, *Phys. Rev. E*, **68**, 031710 (2003).

[36] S. Karmakar and V. A. Raghunathan, *Phys. Rev. Lett.* , **91**, 098102 (2003).

[37] L. Finegold, ed., *Cholesterol in Membrane Models*, CRC Press, Boca Raton, FL (1993).

[38] C. Eggeling, C. Ringemann, R. Medda, G. Schwarzmasann, K. Sandoff, S. Polyakova, V. N. Belov, B. Hein, C. Middendorf, A. Schnle and S. W. Hell, *Nature*, **457**, 1159 (2009).

[39] S. L. Veatch and S. L. Keller, *Phys. Rev. Lett.*, **89**, 268101 (2002).

[40] S. L. Veatch and S. L. Keller, *Biochim. Biophys. Acta.*, **1746(3)**, 172 (2005).

[41] T. Baumgart, S. T. Hess and W. W. Webb, *Nature*, **425**, 821 (2003).

[42] M. R. Vist and J. H. Davis, *Biochemistry*, **29**, 451 (1990).

[43] R. P. Rand, V. A. Parsegian, J. A. C. Henry, L. J. Lis, M. McAlister, *Can.J.Biochem.*, **58**, 959 (1980).

[44] W. Knoll, G. Schmidt,K. Ibel and E. Sackmann, *Biochim. Biophys. Acta.* , **945**, 221 (1988).

[45] J. H. Ipsen, G. Karlstrom, O. G. Mouritsen, H. Wennerstrom and M. J. Zuckermann, *Biochim. Biophys. Acta.*, **905**, 162 (1987).

[46] K. Bloch, *Science*, **150**, 19 (1965).

[47] Bibhuranjan Sarangi, PhD thesis: Organization of sterols in Model Membranes, Jawaharlal Nehru University, New Delhi, Chapter 4.

[48] M.A.Kamal, PhD thesis: Influence of some membrane active biomolecules on the phase behaviour of model lipid membranes,Jawaharlal Nehru University, New Delhi,Chapter 4.

[49] B. N. Olsen, P. H. Schlesinger, D. S. Ory and N. A .Baker, *Biochim. Biophys. Acta.*, **1818**, 330 (2012).

[50] A. Guinier and G. Fornet, *Small angle Scattering of X-rays*, Wiley, New York (1955).

[51] O. Glatter and O. Kratky, *Small angle X-ray Scattering*, Academic Press, London (1982).

[52] D. Sherwood, *Crystals, X-rays and Proteins*, Longman, London (1976).

[53] L. D. Landau and E. M. Lifshitz, *Statistical Physics*, 3rd ed.Vol.5, Butterworth-Heinemann (1980).

[54] R. Hosemann and S. N. Bagchi, *Direct Analysis of diffraction by matter*, North-Holland, Amsterdam (1962).

[55] A. Caillé, *C. R. Acad. Sci. Paris, Series B*, **274**, 891 (1972).

[56] G. Pabst,M. Rappolt,H. Amenitsch and P. Laggner, *Phys. Rev. E*, **62**, 4000 (2000).

[57] R. Zhang, R. M. Suter and J. F. Nagle, *Phys. Rev. E.*, **50**, 5047 (1994).

[58] Y. Lyatskaya, Y. Liu,S. T. Nagle, J. Katsaras and J. F. Nagle, *Phys. Rev. E*, **63**, 011907 (2000).

[59] H. M. Wyss, M. Hans, M. Hütter, M. Müller, L. P. Meier and L. J. Gauckler, *J. Coll. Inter. Sci.*, **248(2)**, 340 (2002).

[60] G. Desbois, J. L. Ural and P. A. Kukla, *eEarth Discuss.*, **4**, 1 (2009)

[61] F. Tiarks, T. Frechen, S. Kirsch, J. Leuniger, M. Melan, A. Pfau, F. Richter, B. Schuler and C. L. Zhao, *Prog. Org. Coatings*, **48**, 140 (2003).

[62] A. Rigort and J. M. Plitzko, *Arch. of Biochem. Biophys.*, **581**, 122 (2015)

[63] J. Marmur and P. Doty, *J. Mol. Biol.*, **5**, 109 (1962).

Chapter 2

Structure, Stoichiometry and Stability of CTAT-DNA complexes

2.1 Introduction

When in an aqueous solution, a significant fraction of released counterions of a highly charged macro-ion may condense back onto it. In the case of linear polyelectrolytes, this dictates the effective charge distribution on the backbone. Complexation occurs due the gain in entropy, through the release of bound counterions from the constituent oppositely charged polymers. As a result, the structure of the complexes result from a close-packing of the two species. These form a range of two dimensional lattices effecting different degrees of charge compensation not confined merely to charge neutrality.

The hierarchical assembly of these crystals depends on the interaction between the species under consideration and a host of external conditions like temperature, osmotic pressure and the effect of external buffer conditions. The nature of the binding counterions are known to have an immense influence on the morphology of the self-assembly of micelles. In the case of cetyl trimethyl ammonium tosylate (CTAT), containing the strongly binding tosylate (T^-) counterions, worm-like micelles (WLMs) are formed at concentrations as low as 1wt.% in water [1], and even highly ordered two dimensional phases at higher concentrations [2, 3]. chapter we study the effect of osmotic pressure

on complexes formed by micelles formed by a cationic surfactant, establish the exact stoichiometry of the individual species, in the different structures exhibited by these complexes.

2.2 Previous Studies

The partial phase diagram of complexes formed by cationic surfactant CTAT and calf thymus DNA complex has been well established [4]. Nematic, square, hexagonal and superhexagonal phases have been reported across the ρ -C_s plane, as shown in Figure 1.1, where ρ is the surfactant to DNA base molar ratio and C_s is the surfactant concentration. At high DNA concentrations(low ρ) and low CTAT concentrations a hexagonal phase (H_I^c) is seen. The H_I^c lattice parameter is observed to gradually change from a $\sim$ 5.70nm at C_s = 10 mM to approximately 6.11 nm at C_s= 80 mM. At low DNA concentrations (high ρ), a square phase (S_I^c)is observed having a lattice parameter a $\sim$ 5.0nm, which is insensitive to both ρ and C_s. At high DNA (low ρ) and high surfactant concentrations a superhexagonal phase ($H_{I,s}^c$) is established, which is a swollen $\sqrt{3} \times \sqrt{3}$ superlattice of the H_I^c structure. The superlattice arrangement is associated with the presence of two types of DNA micelle neighbourhoods. In one, there is 6 fold rotational symmetry of DNA rods around a micelle, similar to the H_I^c structure and the adjoining micelle has a threefold rotational symmetry(Figure 1.7).

2.3 Aim of Present Studies

This chapter deals with establishing the stability and stoichiometry of the phases formed by CTAT-DNA complexes. The proposed structure for the $H_{I,s}^c$ phase is essentially a swollen H_I^c phase. Therefore, it would be expected to transform into the $H_{I,s}^c$ phase on removal of water by applying a osmotic pressure. High molecular weight neutral long chained polymers, PEG8000 and PVP10000, were used to apply osmotic pressure. Further, through elemental analysis, the base to surfactant ratios of the complexes is determined across the ρ -C_s plane, and, verified against those suggested by the structures of these phases proposed earlier.

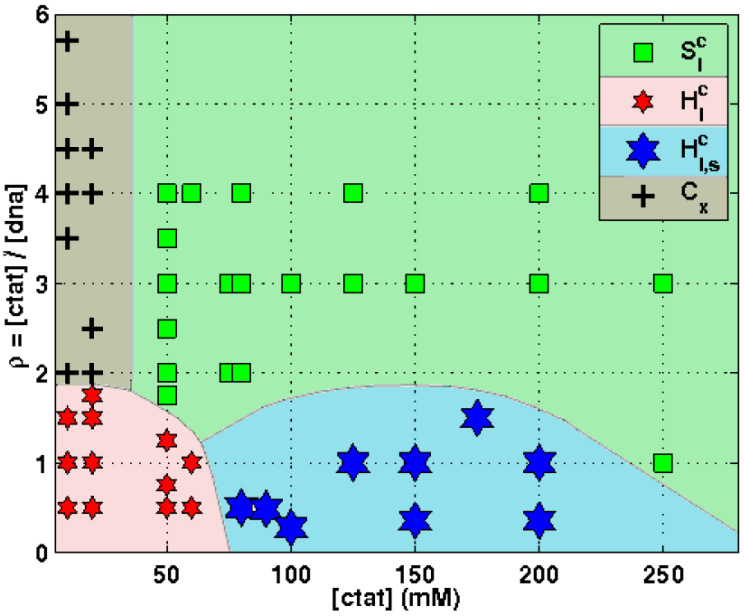

FIGURE 2.1: Phase diagram of CTAT-DNA complex in the ρ-C_s plane

2.4 Materials and Methods

CTAT, Sodium salt of Calf thymus DNA, PVP 10000 and PEG 8000 were obtained from Sigma-Aldrich. All chemicals were used as received. Complexes were prepared by adding appropriate amounts of DNA to surfactant solutions in deionized water(Millipore) and were left for about 5 days for equilibrating.

For the osmotic pressure experiments the samples were prepared at different points on the ρ-C_s plane as stated above. Appropriate amounts of PEG8000 or PVP10000 were then added to these samples in order to get the desired final polymer concentrations. The samples were then sealed and were left to equilibrate for 10 more days. The polymer solution forms a separate phase devoid of surfactant and DNA. For diffraction studies, the complex along with some supernatant was taken in 1mm glass capillaries and then flame sealed to avoid any loss of water. Small-angle x-ray scattering studies, covering a range of scattering vector (q) values from 0.01 to 5.0 nm^{-1}, were carried out using a Hecus S3-Micro system, fitted with a 1-dimensional position-sensitive detector. Typical exposure time was 30 min. In the case of trials with osmotic pressure, the sealed capillaries were run again at a later time to ensure consistency of measured periodicities.

Elemental analysis is carried out by weighing the CTAT-DNA complex at the appropriate composition and following measurement protocol as mentioned before.

TABLE 2.1: Osmotic pressure $\pi[Pa]$ applied by solutions of neutral polymers PEG8000 and PVP10000
(taken from [5])

PEG 8000		**PVP 10000**	
wt.%	$\pi[10^5\text{Pa}]$	wt.%	$\pi[10^5\text{Pa}]$
0	0	0	0
5	0.39	5	3.548
10	1.33	7.5	4.677
15	3.12	10	5.37
20	6.12	15	7.01

2.5 Results and Discussion

2.5.1 Characteristic X-ray diffraction patterns

X-ray diffraction patterns were collected for samples made at three different points on the ρ-C_s plane of the CTAT-DNA phase diagram. The observed patterns index onto S_I^c - square, $H_{I,s}^c$ - superhexagonal and H_I^c - hexagonal lattices at $\rho = 2$,$C_s = 100$mM;$\rho = 1$,$C_s = 100$mM and $\rho = 0.5$,$C_s = 50$mM, respectively.These results are consistent with the phase diagram, given earlier. The corresponding lattice parameters are 5.15nm, 6.10nm and 10.81nm. The characteristic absence of the (10) peak of the $H_{I,s}^c$ superlattice is noted.

2.5.2 Effect of Osmotic Pressure on the structure of the complex

The effect of osmotic pressure on the CTAT-DNA complexes, applied using PEG8000 [5], is presented in Table 2.2. Samples were prepared at different points along the ρ-C_s plane of the CTAT-DNA phase diagram spanning all observed phases, as shown in Figure 2.3.

At low osmotic pressures, the superhexagonal lattice $H_{I,s}^c$ persists, with no discernible change in the structure. Increasing the PEG8000 concentration to 5 wt%, forces the $H_{I,s}^c$ formed at ρ=0.5;[CTAT]=100mM, with a lattice parameter of a $\sim$ 10.81nm into a

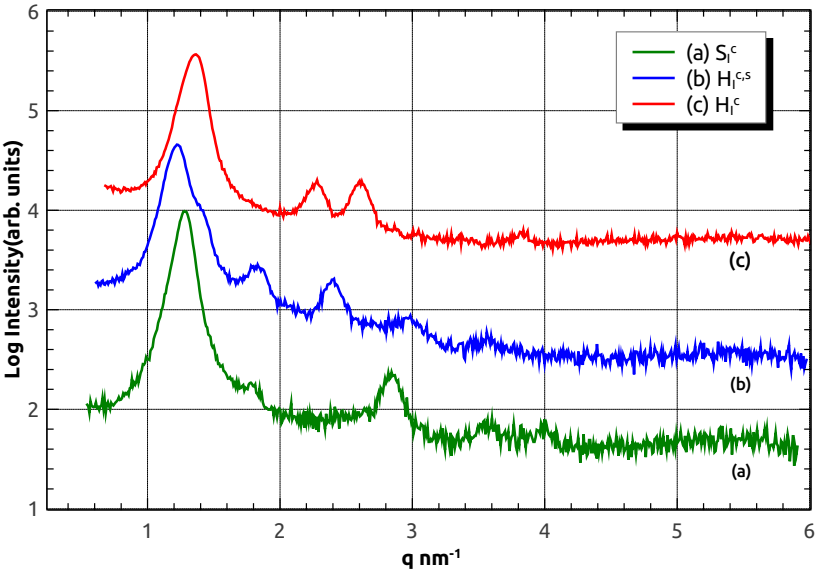

FIGURE 2.2: Characteristic X-ray patterns of CTAT-DNA complexes at (**a**)ρ = 2 C_s = 100mM; (**b**)ρ = 1 C_s = 100mM ; (**c**)ρ =0.5 C_s =50mM.

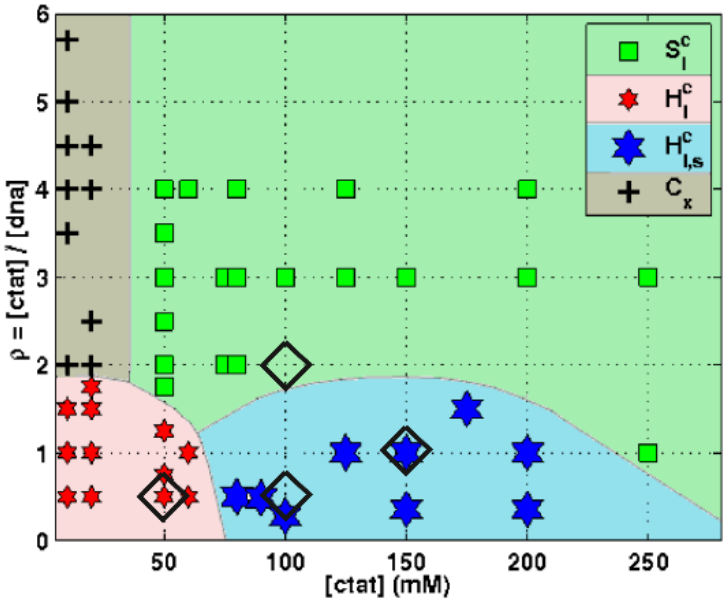

FIGURE 2.3: Phase diagram of CTAT-DNA complex in the ρ-C_s plane, where Open diamonds indicate points considered for studying the effect of osmotic pressure and lie at; (a)ρ=0.5;C_s=50mM, (b)ρ=0.5;C_s=100mM, (c)ρ=1;C_s=150mM and (d)ρ=2;C_s=100mM

H_I^c with a $\sim$ 6.05nm (Figure 2.4(a,b)). Further increase in polymer concentration, upto 20wt%, induces no change in the structure (Figure 2.4,c-g). However, a slight change in the lattice parameter is seen, from 6.05 nm to 5.80 nm as the polymer concentration is increased from 7.5wt% to 10 wt%.

For the complex made at ρ=1;[CTAT]=150mM, the lattice is transformed from $H_{I,s}^c$ into H_I^c at a higher polymer concentration of 7.5wt% (Figure 2.5,a-c).Further increase in osmotic pressure only causes a change in the lattice parameter of the H_I^c, from 6.05nm to 5.83nm between 10 wt% and 20 wt% of PEG8000(Figure 2.5,d-g). Further increase in osmotic pressure, pushes the lattice parameter within the bounds of stability of the H_I^c phase but does not change the structure.

Samples prepared in the H_I^c phase at ρ=0.5;C_s=50mM, do not show any change in structure, as shown in Figure 2.6. The lattice parameter changes slightly from 6.10 nm to 5.80nm between 0wt% to 10wt% of PEG8000. The square phase, S_I^c, at ρ=2;C_s=100mM, shows only a slight change in lattice parameter across the entire range of pressures applied, as shown in Figure 2.7. There is a small change in lattice parameter from a $\sim$ 5.05nm at 0wt% to a $\sim$ 4.82nm at 20wt% .

TABLE 2.2: Effect of Osmotic Pressure using PEG8000

Complex		**Lattice Parameter @ wt. % of PEG8000 (nm)**						
ρ	**[CTAT]mM**	**0%**	**2.5%**	**5%**	**7.5%**	**10%**	**15%**	**20%**
0.5	50	6.10 (H_I^c)	6.02 (H_I^c)	5.97 (H_I^c)	5.88 (H_I^c)	5.80 (H_I^c)	5.80 (H_I^c)	5.80 (H_I^c)
0.5	100	10.81 ($H_{I,s}^c$)	10.81 ($H_{I,s}^c$)	6.05 (H_I^c)	6.01(H_I^c)	5.91(H_I^c)	5.83(H_I^c)	5.83 (H_I^c
1	150	10.77 ($H_{I,s}^c$)	10.74 ($H_{I,s}^c$)	10.74 ($H_{I,s}^c$)	6.05(H_I^c)	5.94 (H_I^c)	5.94 (H_I^c	5.83 (H_I^c)
2	100	5.05 (S_I^c)	5.05(S_I^c)	4.97 (S_I^c)	4.97 (S_I^c)	4.97 (S_I^c)	4.82 (S_I^c)	4.82(S_I^c)

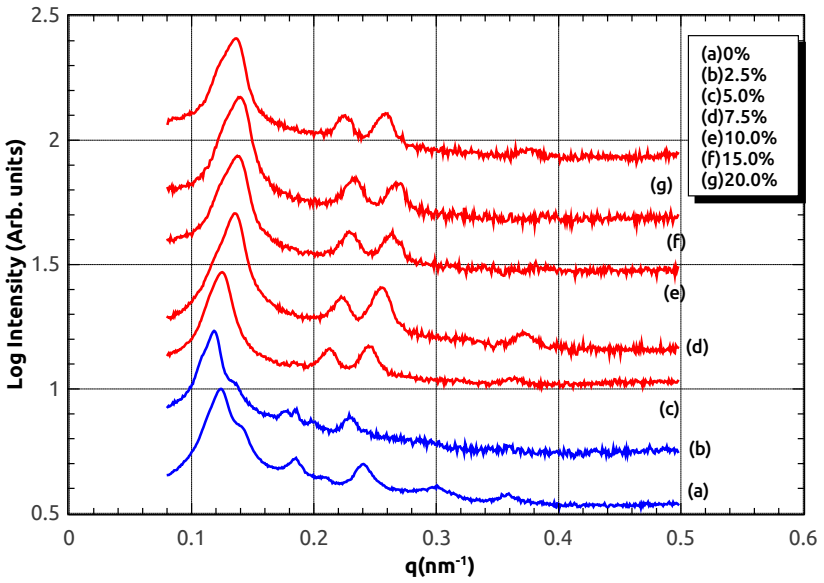

FIGURE 2.4: Diffraction patterns showing the effect of osmotic pressure on $H^c_{I,s}$; ρ=0.5,CTAT=100mM . The numbers indicate the concentration of PEG8000 in the solution

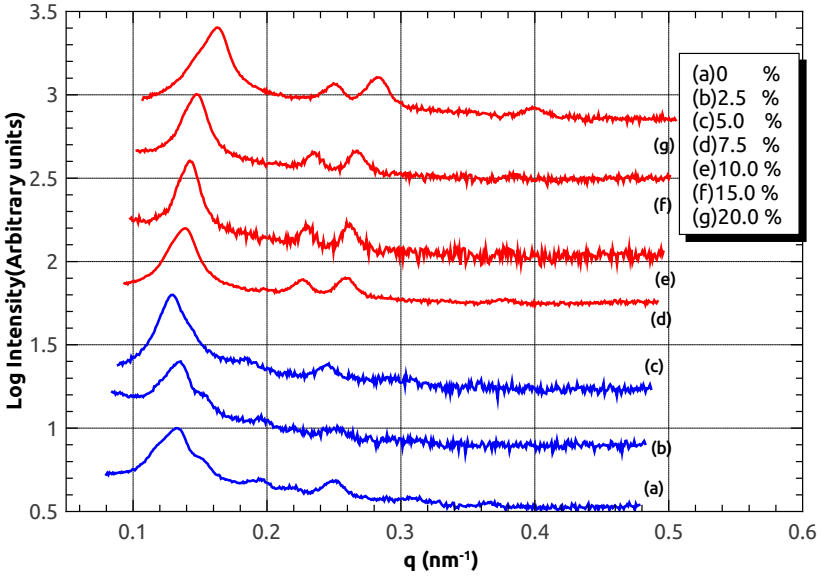

FIGURE 2.5: Diffraction patterns showing the effect of osmotic pressure on $H^c_{I,s}$; ρ=1:CTAT=150mM . The numbers indicate the concentration of PEG8000 in the solution

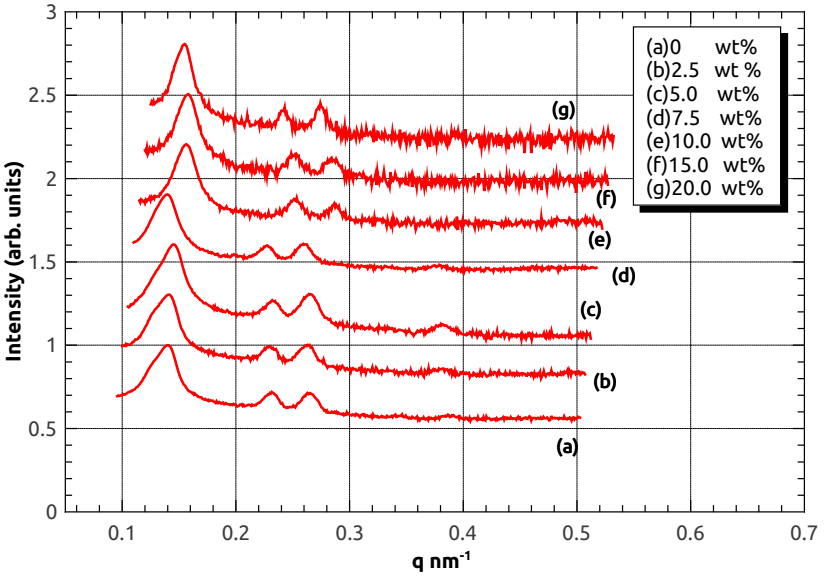

FIGURE 2.6: Diffraction patterns showing the effect of osmotic pressure on H_I^c; ρ=0.5:CTAT=50mM . The numbers indicate the concentration of PEG8000 in the solution.

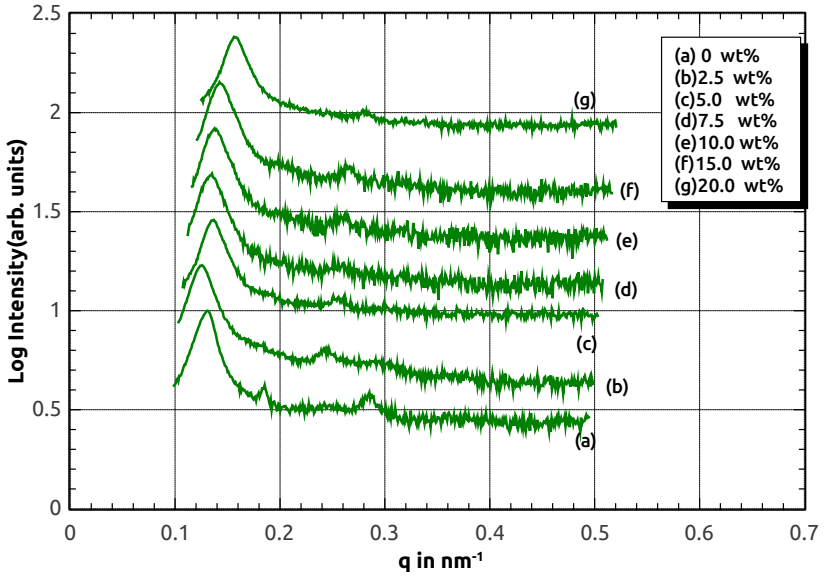

FIGURE 2.7: Diffraction patterns showing the effect of osmotic pressure on S_I^c; ρ=2:CTAT=100mM. The numbers indicate the concentration of PEG8000 in the solution

The effect of osmotic pressure, applied using neutral polymer PVP10000 on the CTAT-DNA complexes is presented in Table 2.3. At low osmotic pressures of 2 wt.%, the $H^c_{I,s}$ is reordered into the H^c_I with lattice parameter of a $\sim$ 6.10nm (Figure 2.8(a,b)). Further increase in polymer concentration upto 15 % does not induce any change in structure. The lattice parameter shifts gradually from 6.10nm at 2 wt.% to 5.70nm at 10wt.% of added PVP10000(Figure 2.8,(c-f)). At 15 wt.% the structure within the complex completely collapses and we see a broad peak indicative of a melt (Figure 2.8,(g)). The osmotic pressure has now exceeded the limit of stability of the structure. Samples prepared in the $H^c_{I,s}$ phase at ρ=0.5;C_s=50mM,as shown in Figure 2.10 do not show any change in lattice arrangement. There is again a slight change in lattice parameter from a $\sim$ 6.07nm to a $\sim$ 5.73nm, between 0wt.% to 10wt.% of PVP10000. At 15wt.% the complex turns into a melt. Birefringence of these complexes indicate that long-range orientational order is maintained, although long-range positional order is lost. $S^c_{I,s}$ phase at ρ=2;C_s=100mM, as shown in Figure 2.11, too does not show any change in structure across the range of pressure applied. However, there is loss of long-range translational order at 15 wt.% of PVP10000, as indicated by the broad peaks in the diffraction pattern.

TABLE 2.3: Effect of Osmotic Pressure using PVP10000

Complex		**Lattice Parameter @ wt. % of PVP10000 (nm)**					
ρ	**[CTAT]mM**	**0%**	**2%**	**5%**	**7.5%**	**10%**	**15%**
0.5	50	6.07 (H^c_I)	5.97 (H^c_I)	5.83(H^c_I)	5.73 (H^c_I)	5.73 (H^c_I)	Melt
0.5	100	10.81 ($H^c_{I,s}$)	6.10(H^c_I)	5.83(H^c_I)	5.83 (H^c_I)	5.70(H^c_I)	Melt
1	150	10.70 ($H^c_{I,s}$)	6.07 (H^c_I)	5.88 (H^c_I)	5.73 (H^c_I)	5.73 (H^c_I)	Melt
2	100	5.05(S^c_I)	4.94(S^c_I)	4.82(S^c_I)	4.82(S^c_I)	4.82(S^c_I)	Melt

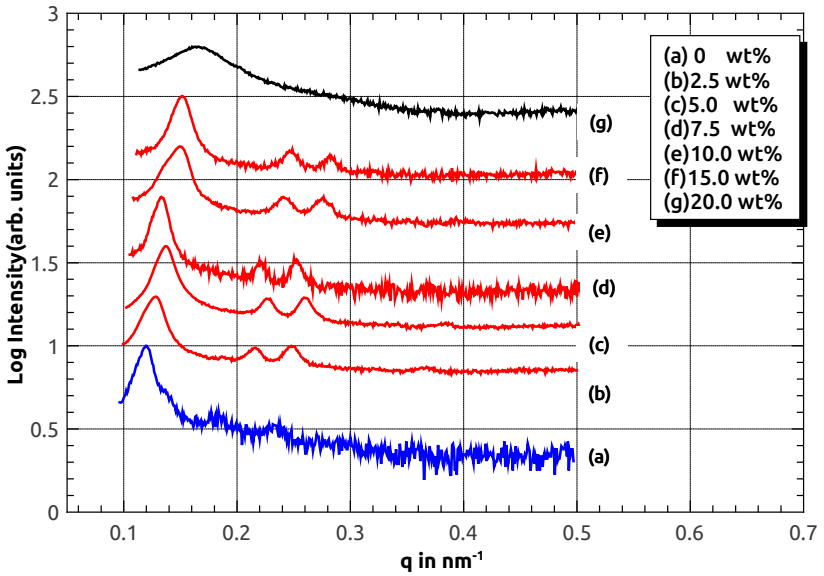

FIGURE 2.8: Diffraction patterns showing the effect of osmotic pressure on $H^c_{I,s}$; ρ=0.5:CTAT=100mM . The numbers indicate the concentration of PVP10000 in the solution

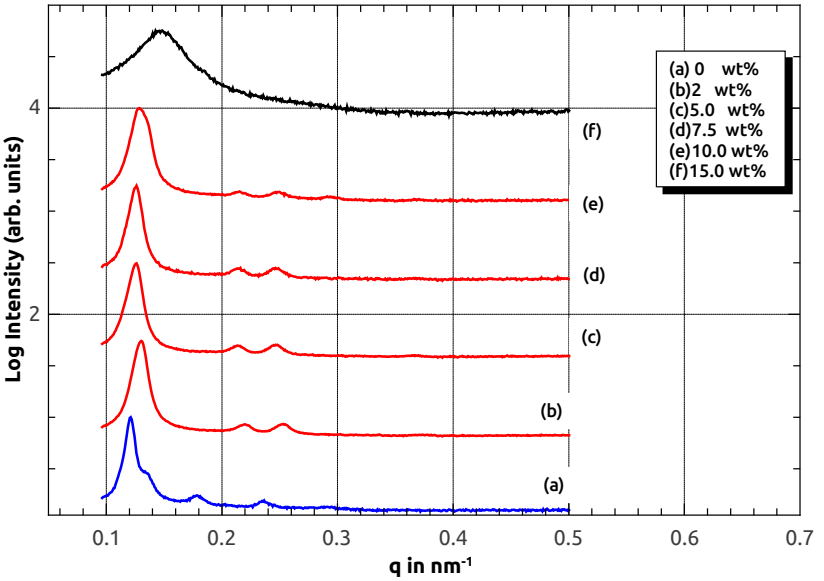

FIGURE 2.9: Diffraction patterns showing the effect of osmotic pressure on $H^c_{I,s}$; ρ=1:CTAT=150mM . The numbers indicate the concentration of PVP10000 in the solution

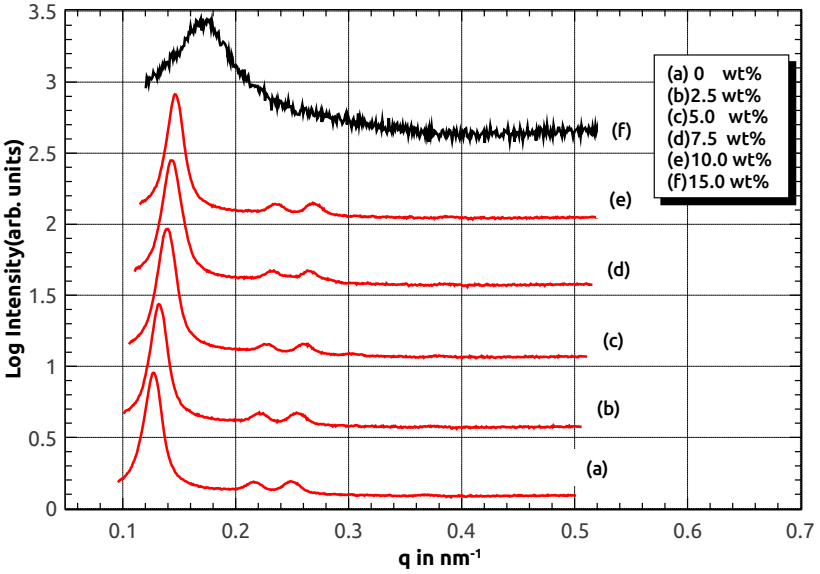

FIGURE 2.10: Diffraction patterns showing the effect of osmotic pressure on H_I^c; ρ=0.5:CTAT=50mM . The numbers indicate the concentration of PVP10000 in the solution

2.5.3 Elemental analysis and establishment of stoichiometry

Elemental analysis of CTAT-DNA complexes at different values along the ρ-C_s plane was carried out. Table 2.4 contains the results.

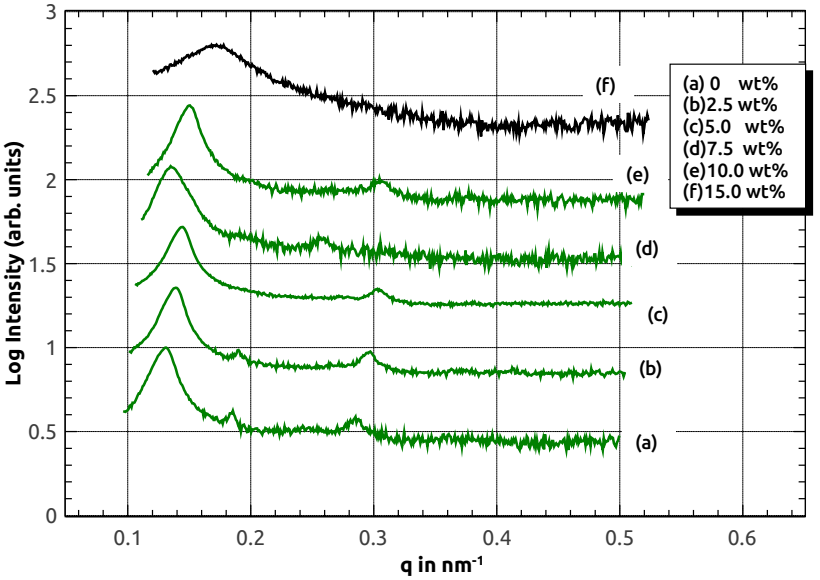

FIGURE 2.11: Diffraction patterns showing the effect of osmotic pressure on S_I^c; ρ=2:CTAT=100mM . The numbers indicate the concentration of PVP10000 in the solution

TABLE 2.4: Elemental analysis data of CTAT-DNA complexes along ρ-C_s plane

Phase	ρ	C_s	N%	C%	S%	N_b/N_s
H_I^c	0.5	50	7.41	49.43	2.627	0.821
	1	50	7.25	49.56	2.611	0.776
$H_{I,s}^c$	0.5	100	6.54	50.33	3.873	0.709
	1	100	6.81	53.49	3.458	0.621
	1	150	7.44	56.20	3.694	0.681
S_I^c	2	100	5.73	58.07	3.752	0.346
	3	50	5.6	59.68	3.576	0.294
	3	100	5.29	60.70	3.504	0.236

Complexes made in the H_I^c phase show N_b/N_s values of 0.821 and 0.776 at ρ=0.5;C_s=50mM and ρ=1;C_s=50mM, respectively. Complexes made at low ρ and higher CTAT concentrations form the $H_{I,s}^c$ superhexagonal lattice. Samples made at ρ=0.5;C_s=100mM , ρ=1;C_s=100mM and ρ=1;C_s=150mM have N_b/N_s values as 0.709, 0.621 and 0.681, respectively. Samples prepared at high ρ form complexes displaying a S_I^c square lattice. Complexes analyzed at ρ=2;C_s=100mM , ρ=3;C_s=50mM and ρ=3;C_s=10mM, return N_b/N_s values of 0.346, 0.294 and 0.236 respectively.

2.6 Discussion

Structures of different phases formed by CTAT-DNA complexes were elucidated in [4] from SAXS data. In this chapter we have used complementary experimental techniques to check the proposed structures. The structure of the $H_{I,s}^c$ phase proposed in [4] is essentially a slightly swollen version of the H_I^c structure. Hence on removing some water from the former it should transform into the latter. This is indeed what we find from our osmotic pressure experiments. On applying an osmotic pressure, using a high molecular weight polymer, which cannot penetrate into the structure, we find that the $H_{I,s}^c$ structure is transformed into the H_I^c structure above a critical value of the osmotic pressure. These observations are consistent with the structures proposed in [4].However, in the absence of knowledge of the energetics governing these systems, we have not attempted to estimate the osmotic pressure quantitatively.

The headgroup area of the quaternary ammonium surfactant in the micellar phase is about 0.65nm^2 [6]. Assuming both the DNA and the micelle to be infinitely long, the S_I^c structure has a DNA to surfactant stoichiometric ratio of 1:1. Taking the micellar radius

to be 2.0 nm, the area on the micellar surface corresponding to the height of a base pair along the DNA strand(0.332 nm [7]) turns out to be 4.17 nm^2. This corresponds to 3.2 surfactant molecules for every DNA base. Hence $N_b/N_s = 0.31$. In the case of the $H^c_{I,s}$ and the H^c_I structures the DNA to micelle stoichiometric ratio is 2:1. Hence, in these cases $N_b/N_s = 0.62$. The agreement between the estimated and observed values are very good both in the S^c_I and the $H^c_{I,s}$ phases. In the H^c_I phase the experimental values are slightly higher. It is possible that in this case, the complex incorporates a higher amount of DNA by restricting the length of the micelles. In any case, the observed differences are not very large and we may conclude that the results of the elemental analysis are also in agreement with the proposed structures.

2.7 Conclusions

In this chapter, we have discussed the influence of osmotic pressure on the different structures formed by the CTAT-DNA complexes. We clearly observe a transfer of $H^c_{I,s}$ into H^c_I structure above a critical value of the osmotic pressure. These results are consistent with the structures proposed in [4]. In addition we have also estimated the DNA:micelle stoichiometry in different structures using elemental analysis. These results further support the proposed structures.

Bibliography

[1] J. F. A. Soltero, J. E. Puig, O. Manero, P. C. Shulz, *Langmuir*, **11**, 3337 (1995).

[2] M. E. Cates and S. J. Candau, *Journal of Physics:Condensed Matter* , **2(33)**, 6869 (1990).

[3] A. Pal, R.Mary, V.A.Raghunathan, *Journal of Molecular Liquids*, **174**, 48 (2012).

[4] A. V. Radhakrishnan, S. K. Ghosh, G. Pabst, V. A. Raghunathan and A. K. Sood, *Proc. Natl. Acad. Sci., U. S. A.*, **109**, 6394 (2012).

[5] *R. P. Rand. Osmotic Pressure Data; Department of Biological Sciences,Brock University. Available online at* http://www.brocku.ca/researchers/peter_rand/osmotic/osfile.html

[6] I. Kamal, A. K. Das, P. S. Goyal, G. U. Ahmad, *Bang. J. Phys*, **15**, 105 (2014).

[7] J. C. Wang, *Proc. Natl. Acad. Sci., U. S. A.*, **76**, 200 (1979).

Chapter 3

Structure and Stoichiometry of CTAB-DNA complexes

3.1 Introduction

Giant unidimensional micelles can be obtained from the coalescence of smaller rod-like micelles under suitable conditions. This growth is highly sensitive to the trigger that causes it. The presence of monovalent ions, for instance, alters the effective headgroup area through the screening of repulsive coulombic forces. This causes the hemispherical end-caps of the rods to become highly unfavourable. The preferred morphology is now of extremely long cylinders of the order of microns. The emergent anisotropy from such a growth process can manifest in varied forms and evoke a vast range of physical responses.

3.2 Previous Studies

The tunability of CTAB-DNA complexes through the addition of short chained alcohols (Hexanol) has been studied previously [1]. The phase diagram (Figure 3.1) showed a rich plethora of phases, where at low DNA concentrations a transition from intercalated hexagonal(H_I^c) $\rightarrow$ lamellar(L_α^c) $\rightarrow$ inverted hexagonal(H_{II}^c) and at high DNA concentrations a reentrant L_α^c $\rightarrow H_{II}^c \rightarrow$ L_α^c transition was noted.

The structure of the H_I^c phase observed was shown to have a structural motif with a 2:1 DNA to micellar ratio after detailed modelling [2]. The effect of salts with strongly

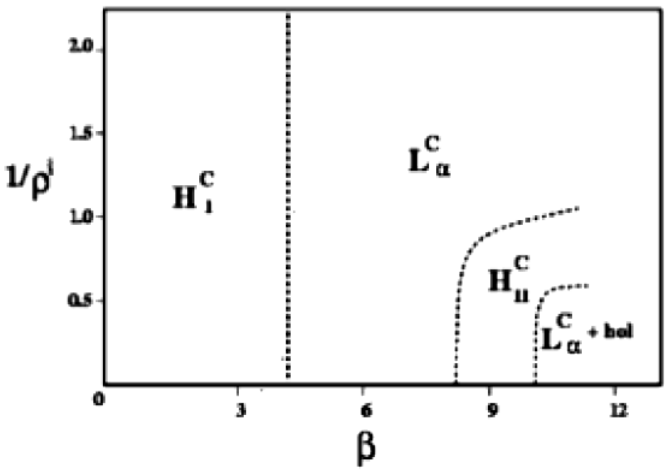

FIGURE 3.1: Partial phase diagram of CTAB-DNA-Hexanol along the β-ρ' plane where β=[hexanol]/[CTAB] and ρ'=(Weight of CTAB)/(Weight of DNA).

binding counter-ions,neutral lipid and co-surfactant has been explored earlier [3]. Other reports in literature have shown a discrete transition of DNA from elongated coil to a collapsed globule when complexed with cationic surfactants [4]. Based on packing considerations and calorimetry measurements [5], another model has been proposed for the hexagonal phase having a DNA to micelle stoichiometric ratio of 3:1 for effective electroneutrality.

3.3 Aim of Present Studies

In this chapter, we study the effect of monovalent salt NaCl on the phase behaviour of CTAB-DNA complexes. We track the complex across the isoelectric point ρ=1, where ρ is the is the CTAB to DNA base molar ratio. We also determine the exact stoichiometry between the number of bases and the number of surfactant molecules through elemental analysis. We evaluate, analyze and compare both models from literature; $H^c_{I,21}$ and $H^c_{I,31}$ with SAXS data collected for the above complexes.

3.4 Materials and Methods

Cetyltrimethylammoniumbromide(CTAB), the bromine salt of calf thymus DNA and NaCl were obtained from Sigma-Aldrich. All chemicals were used as received. Complexes were prepared by adding appropriate amounts of DNA to surfactant at values of ρ that are to be studied. The surfactant concentration is held at C_s=20mM and hydrated with the appropriate aqueous NaCl solutions and left for about 5 days for equilibrating. The rest of the protocol is as detailed in the previous chapter, for both small-angle x-ray studies and elemental analysis.

3.5 Results

3.5.1 Effect of NaCl on phase behaviour of CTAB-DNA complexes

X-ray diffraction patterns were collected for a range of values of ρ across the isoelectric point (ρ=1). At very low CTAB concentrations (ρ=0.25) the complex formed a gel giving no appreciable signal. At ρ=0.5, the complex started to stabilize, and showed development of a broad shoulder at the $\sqrt{3}$ position of a hexagonal lattice with a $\sim$ 5.22 nm (Figure 3.2,(a)). Upon further increasing ρ to 1 the hexagonal lattice fully develops giving strong peaks in the ratio of 1:$\sqrt{3}$:2 at a slightly increased a $\sim$ 5.44nm. Above the isoelectric point the hexagonal lattice ordering is maintained, with an increase in lattice parameter as tabulated in Table 3.1.

The x-ray diffraction patterns emerging from the addition of NaCl at 350mM to the CTAB-DNA complexes are presented in Figure 3.3 and the corresponding lattice parameters are tabulated in Table 3.1. At ρ=0.25, as before there was a gel that gave no signal. At all other points considered the effect of NaCl caused a robust development of the hexagonal lattice.

3.5.2 Modelling and analysis

In this section, we compare the two models describing the hexagonal phase, namely $H^c_{I,21}$ and $H^c_{I,31}$. We deployed a cartesian coordinate system (x,y) in order to describe the positions of the delta functions representing the micelles and the DNA strands in the

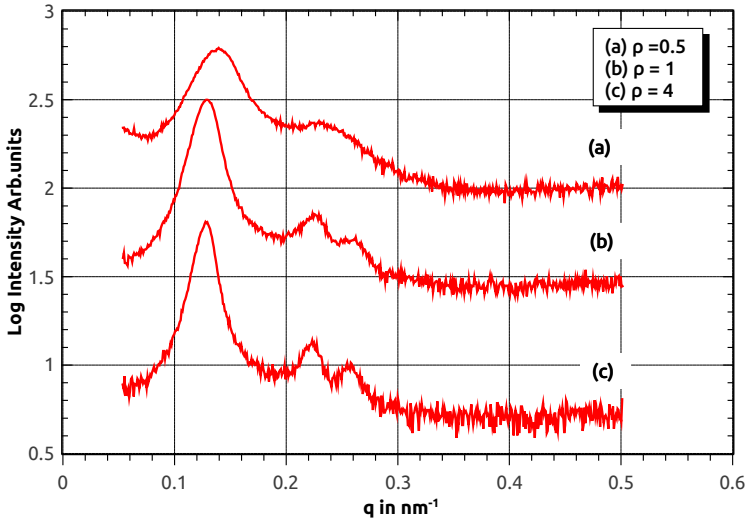

FIGURE 3.2: X-ray diffraction patterns of CTAB-DNA complexes at **(a)**ρ=0.5 **(b)**ρ=1 **(c)**ρ=4

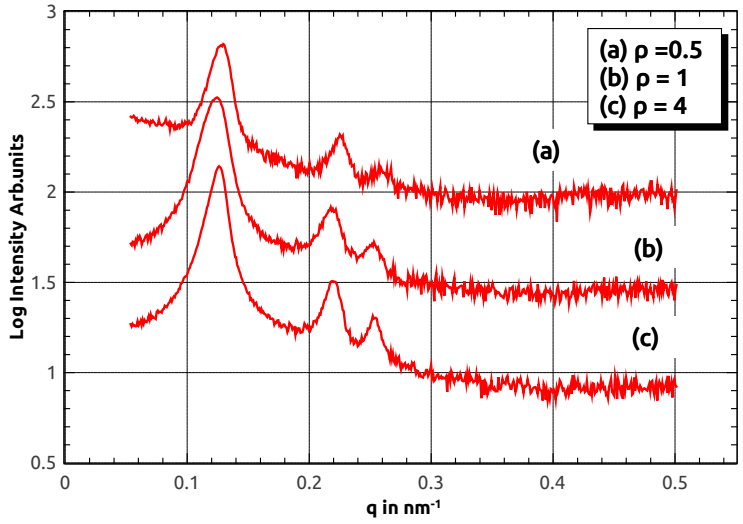

FIGURE 3.3: X-ray diffraction patterns of CTAB-DNA complexes at **(a)**ρ=0.5;**(b)**ρ=1 and **(c)**ρ=4 and 350mM NaCl.

motif. The DNA strand is described as a uniform disc with electron density ρ_d; having a radius of r_d (1.25 nm) which includes a hydration shell. The electron density of the DNA rod is expressed as,

$$\rho_d(r) = \begin{cases} \rho_d - \rho_w, & r < r_d \\ 0, & r > r_d \end{cases} \tag{3.1}$$

and its corresponding Fourier transform is,

TABLE 3.1: **Lattice Parameter**

ρ	**Conc. of NaCl (mM)**	**Lattice Parameter (nm)**
0.25	350	-
0.5	0	5.22
	350	5.34
1	0	5.44
	350	5.57
4	0	5.57
	350	5.64
5	0	5.68
	350	5.71

$$f_m(q) = 2\pi(\rho_h - \rho_w)r_h J_1(qr_h)/q - 2\pi(\rho_h - \rho_c)r_c J_1(qr_c)/q \tag{3.2}$$

The electron density of the micelle is defined as,

$$\rho_m(r) = \begin{cases} \rho_c - \rho_w, & r < r_c \\ \rho_h - \rho_w, & r_c < r < r_c + \delta \\ 0, & r > r_c + \delta, \end{cases} \tag{3.3}$$

where ρ_w is the electron density of water, ρ_h electron density of the headgroup region and ρ_c electron density of hydrocarbon region. J_1 is the Bessel function of order 1 and δ represents the width of the annular headgroup region around a hydrocarbon core of radius r_c. The values for ρ_c (280 e/nm^3) and ρ_w(332 e/nm^3) are taken from literature [6]. The Fourier transform of the micellar electron density is,

$$f_d(q) = 2\pi(\rho_d - \rho_w)r_d J_1(qr_d)/q \tag{3.4}$$

For the $H^c_{I,21}$ motif, δ(0,0) defines the position of the centre of the micelle and $\delta(0,b)$ and $\delta(0,\text{-}b)$ define the positions of the centres of the two DNA strands, as shown in Figure 1.6. The parameter $b = r_c + \delta + r_d$ and is constrained to be $a/\sqrt{3}$, due to close packing (Figure 3.4). Hence, r_c and δ cannot be independently varied. The electron density is a convolution of the electron density of the DNA, ρ_{dna}(r) with the delta functions representing their positions plus that of the micelle, $\rho_m(r)$, convoluted with the delta function representing its position. The electron density is therefore;

$$\rho_{21}(r) = \rho_{dna}(r) \circledast \{\delta(0,b) + \delta(0,-b)\} + \rho_m(r) \circledast \{\delta(0,0)\} \tag{3.5}$$

The Fourier transform of which gives,

$$f_{21}(q,\phi) = f_d(q)(2Cos[qbSin\phi]) + f_m(q) \tag{3.6}$$

For the $H^c_{I,31}$ motif, $\delta(0,0)$ defines the position of the centre of the micelle and the positions of the 6 DNA strands are given by $\delta(0,\ b)$, $\delta(0,\ b)$, $\delta(\sqrt{3}/2\ b, b/2)$, $\delta(\sqrt{3}/2b, -b/2)$, $\delta(-\sqrt{3}/2b, -b/2)$ and $\delta(-\sqrt{3}/2b, b/2)$, as shown in Figure 3.5. The parameter b is defined by $r_c + \delta + r_d$ and is constrained to be $a/2$, due to close packing constraints (Figure 3.6). Again, r_c and δ cannot be independently varied.The electron density is therefore;

$$\begin{aligned}\rho_{31}(r) = (1/2)\rho_{dna}(r) \circledast \{&\delta(0,b) + \delta(0,-b) + \delta(\sqrt{3}/2b, b/2) + \delta(\sqrt{3}/2b, -b/2) \\ &+ \delta(-\sqrt{3}/2b, -b/2) + \delta(-\sqrt{3}/2b, b/2)\} \\ &+ \rho_m(r) \circledast \{\delta(0,0)\}\end{aligned} \tag{3.7}$$

The factor of (1/2) in the first term is required to take care of the correct stoichiometry.

The Fourier transform of the above gives,

$$\begin{aligned}f_{31}(q,\phi) = 1/2 f_d(q)\{&2Cos[qbSin\phi] + 4Cos[qb/2Sin\phi]Cos[q\sqrt{3}/2bCos\phi]\} \\ &+ f_m(q)\end{aligned} \tag{3.8}$$

The fitting procedure is carried out for both models, $H^c_{I,21}$ and $H^c_{I,31}$, at two different points at ρ=1; 0mM NaCl and at ρ=4; 0mM NaCl and the results are tabulated in Table 3.2 and Table 3.3, respectively.

Although the intensities generated from both models closely mimic that from the diffractograms, the $H^c_{I,21}$ model gives physically relevant parameters of ρ_h= 362 e/nm^3,δ=0.258 nm ; ρ_h= 348 e/nm^3,δ=0.432 nm at ρ=1 and ρ=4, respectively. The headgroup area electron density of bare CTAB is projected to be ρ_h= 380e/nm^3 due to a heavy Br^-

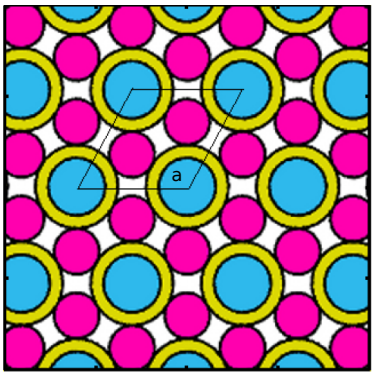

FIGURE 3.4: Lattice of $H^c_{I,21}$, from [1]

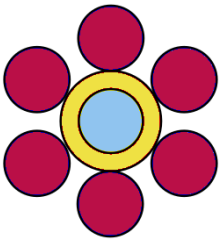

FIGURE 3.5: Motif for the $H^c_{I,31}$ showing the 6-fold arrangement of DNA around the micelle. We consider only 1/2 DNA contribution in the calculation.

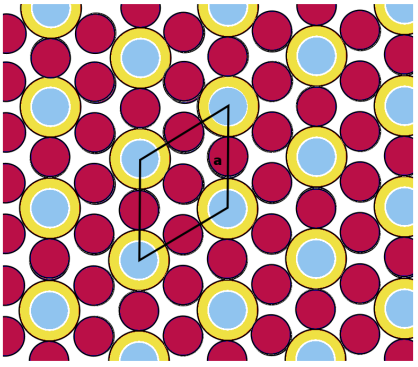

FIGURE 3.6: Lattice of $H^c_{I,31}$

TABLE 3.2: Observed Relative Intensities I_{obs}, and those calculated for the 2:1 (I_{21}) and the 3:1 (I_{31}) models for the complex at ρ=1 . The best fit for the parameters are also indicated below.

ρ=1 ;a = 5.44 nm				
h	k	I_{obs}	I_{21}	I_{31}
1	0	100	100	100
1	1	7.8	7.63	7.89
2	0	0.9	0.72	0.56
2	1	0	0.02	0.85
3	0	0	0.62	0.03
ρ_h(e/nm^3)			362	258
$\delta(nm)$			0.294	1.468

TABLE 3.3: Observed Relative Intensities I_{obs},and those calculated from the 2:1 (I_{21}) and the 3:1 (I_{31}) models for the complex at ρ=4 .The best fit for the parameters are also indicated below.

ρ=4 ;a = 5.57 nm				
h	k	I_{obs}	I_{21}	I_{31}
1	0	100	100	100
1	1	8.1	7.99	8.3
2	0	1.8	1.70	0.47
2	1	0	0.04	1.08
3	0	0	0.4	0
ρ_h(e/nm^3)			348	246
$\delta(nm)$			0.432	1.537

counterion condensation [7]. The release of some of these ions into bulk due to complexation with DNA can lead to a slight decrease in electron density. This could explain the slightly lower values obtained from the fit.

For the $H^c_{I,31}$ structure, values of ρ_h= 258 e/nm^3,δ=1.468 nm ; ρ_h= 246 e/nm^3,δ=1.537 nm are obtained at ρ=1 and ρ=4 , respectively. The value for ρ_h would necessarily have to be greater than ρ_c. However, the values obtained for ρ_h from the fit for this structure do not satisfy this condition. Further the values for δ are also not realistic.

3.5.3 Elemental Analysis and establishment of stoichiometric ratios

Elemental analysis of CTAB-DNA complexes at different ρ values across the isoelectric point was carried out for two different salt concentrations. Table 3.4 contains the results.

TABLE 3.4: Elemental analysis data of CTAB-DNA complexes

ρ	**Conc. Of NaCl [mM]**	**N%**	**C%**	$\mathbf{N_b/N_s}$
0.25	350	7.58	30.19	1.943
0.5	0	9.81	46.46	1.267
	350	7.41	39.26	1.02
1	0	8.58	51.83	0.734
	350	7.29	44.24	0.727
4	0	7.89	53.44	0.571
	350	7.04	50.66	0.498
5	0	7.68	53.14	0.545
	350	6.56	47.83	0.483

In the absence of salt N_b/N_s decreases monotonically with increasing ρ from 1.267 at ρ=0.5 to 0.545 at ρ=5. A similar behaviour is seen at 350mM NaCl.In this case too, N_b/N_s decreases monotonically with increasing ρ, from 1.943 at ρ=0.25 to 0.483 at ρ=5. Further for the same value of ρ the N_b/N_s ratio is slightly lower in the presence of salt.

3.6 Discussion

In this chapter we have fitted the small-angle x-ray diffraction data from CTAB-DNA complexes to models proposed in the literature. Of these, only the $H^c_{I,21}$ model gives a satisfactory fit with the experimental data. Hence, the $H^c_{I,31}$ structure can be ruled out based on these studies.

We have also estimated the DNA base to surfactant molar ratio in these complexes using elemental analysis. This ratio is found to depend on the value of ρ decreasing monotonically with increasing ρ. At ρ=1, N_b/N_s =0.7, which is rather close to that estimated for H^c_I as discussed in the earlier chapter. It decreases at higher values of ρ indicating that a higher concentration of the surfactant is present in the complex. This suggests the formation of vacancies in the 2D Hexagonal lattice at the DNA sites. Similarly, at low values of ρ the N_b/N_s ratio is much higher suggesting the formation of vacancies at the micellar sites. We can say that by creating such vacancies the complex can incorporate higher amount of the excess species without changing the structure. In these two limits the assumption of infinitely long aggregates used to estimate N_b/N_s in the previous chapter breaks down. In the presence of salt at a given ρ the N_b/N_s values

are slightly lower. This is highly suggestive of the formation of longer micelles. Hence, the N_b/N_s values are also shown to be consistent with the $H^c_{I,21}$ structure.

3.7 Conclusions

The H^c_I lattice structure persists across the range of ρ probed. The addition of monovalent salt (NaCl) results in the growth of micelles and results in enhanced translational order resulting in sharper peaks in the diffraction data. Our diffraction data are consistent with the $H^c_{I,21}$ structure and $H^c_{I,31}$ structure proposed in literature can be ruled out. Elemental analysis shows that the stoichiometry of the structure is not fixed but can be tuned by varying ρ. This most probably arises from the creation of voids in the lattice that allow additional intake of the excess species.

Bibliography

[1] R. Krishnaswamy, V. A. Raghunathan and A. K. Sood, *Phys. Rev. E*, **69**, 031905 (2004).

[2] R. Krishnaswamy, G. Pabst, M. Rappolt, V. A. Raghunathan and A. K. Sood, *Phys. Rev. E*, **73**, 031904 (2006).

[3] A. V. Radhakrishnan, PhD thesis: Investigations on the polymorphism of surfactant DNA complexes, Jawaharlal Nehru University, New Delhi, Chapter 4.

[4] S. M. Melnikov, V. G. Sergeyev, K. Yoshikawa, H. Takahashi and I. Hatta, *J. Chem. Phys.*, **107**, 6917 (1997).

[5] C. Leal, L. Wadsö, G. Olofsson, M. Miguel and H. Wennerström *J. Phys. Chem. B*, **108 (9)**, 3044 (2004).

[6] B. Cabane, *Surfactant Solutions:New Methods of Investigation, edited by R. Zana*, Marcel-Dekker, New York (1987).

[7] F. Husson, H. Mustacchi and V. Luzzati, *Acta. Cryst.*, **13**, 575 (1960).

Chapter 4

Structure, Stability and Stoichiometry of DTAB-DNA complexes

4.1 Introduction

The associativity between DNA and cationic surfactants is a complex interplay between the surfactant packing ratio and the electrostatics governing the system. Self-assembly of surfactant aggregates shows high sensitivity to the hydrocarbon chain length displaying a vast range of regular and irregular structural forms [1]. This leads to the dependence of the complexation phenomena on the morphology of the aggregate, which can be tweaked through the suitable tuning of external conditions like electrolyte concentration.

4.2 Previous Studies

The effect of monovalent salts and salts with other counter-ions on DTAB-DNA complexes have been studied previously [2]. The complete phase sequence, resolution of structure and stoichiometry have not been thoroughly investigated. Earlier reports have indicated the possibility of a two stage binding process to describe the formation of the DTAB-DNA complex [3]. More recent studies suggest that the binding of DTAB could

induce possible secondary structural changes to DNA [4–8]. However, these studies involving microcalorimetric and diffusion measurements have not generated a consensus opinion on the exact nature of the micellar arrangement around the DNA scaffolding. The dependence on chain length of different trimethylammoniumbromides with DNA estimating particle size measurements through dynamic light scattering and Atomic force microscopy has been reported [9, 10]. These studies again hint at the inability of shorter chain analogues to effectively neutralize the charges on the DNA. A comprehensive overview of the problems besetting DTAB-DNA complex formation has been presented recently [11].

4.3 Aim of Present Studies

In this chapter, we study the effect of addition of monovalent salt NaCl to dodecyltrimethylammonium bromide (DTAB)-DNA complexes at different values of ρ. The effect of osmotic pressure applied using neutral long chained polymers PEG8000 and PVP10000 on the complex is presented. Through elemental analysis, we determine the base to surfactant ratios of the complexes across the ρ -[NaCl] plane, and compare with those estimated from structural considerations.

4.4 Results

4.4.1 Effect of addition NaCl on phase behaviour of DTAB-DNA complex

A partial phase diagram showing the effect of NaCl on DTAB-DNA complexes across a range of ρ is shown in Figure 4.1 . The complex formed in the absence of salt shows lack of long range translational correlations. The diffraction patterns obtained across the range of ρ probed show broad peaks in the small angle region. The addition of small amounts of NaCl increases the translational ordering in the complex, giving a $H^c_{I,s}$ superhexagonal structure at low ρ and a S^c_I square structure at high ρ.

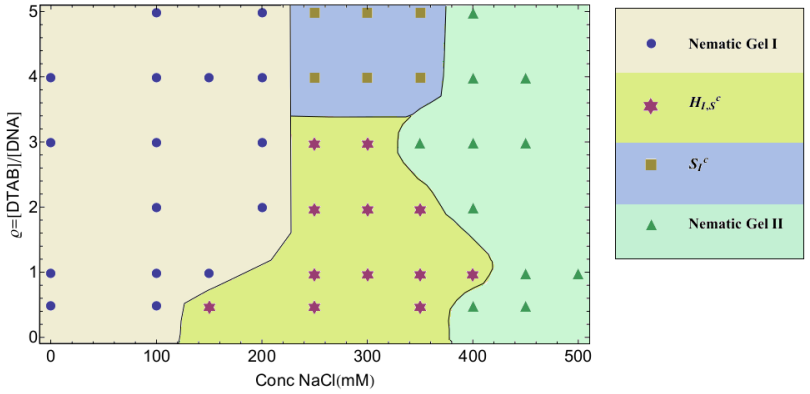

FIGURE 4.1: Partial phase diagram in the ρ-[NaCl] plane for DTAB-DNA complexes, deduced from diffraction data.

4.4.1.1 Phase behaviour of DTAB-DNA complex at low ρ

At high DNA concentration (ρ=0.5) the complex formed in the absence of NaCl shows a broad peak in the diffraction pattern. Under a polarizing microscope these complexes are birefringent. We refer to this as a "nematic-gel I" as they have long-range orientational order but lack long-range translational order. At [NaCl]= 150mM the complex develops into a $H^c_{I,s}$ superhexagonal lattice. This structure is retained up to [NaCl]=350mM. The lattice parameter changes from a∼8.244 nm at [NaCl]=150mM to a∼8.57 nm at [NaCl]=350mM. At [NaCl]=400mM the complex melts into a birefringent nematic gel giving rise to a broad peak in the diffraction pattern.This is noted as "nematic-gel II".

At ρ =1 the "nematic-gel I" is obtained in the absence of NaCl (Figure 4.2,(a)). As more salt is added to the system the complex transforms into the $H^c_{I,s}$ structure, Figure 4.3. As in the case of CTAT-DNA complexes the (1,0) peak is always absent in the diffraction pattern of the structure. The lattice parameter changes from a∼8.43nm at [NaCl]=250mM to a∼8.82nm at [NaCl]=400mM. At [NaCl]=450mM the lattice structure is lost and we end up with "nematic-gel II", Figure 4.4.

The identification of the $H^c_{I,s}$ phase is through indexing the relative positions of the peak to a hexagonal lattice using the relation $d_{hk} = \frac{a}{\sqrt{4/3(h^2+k^2+hk)}}$, where a is the lattice parameter, as shown in Table 4.1

TABLE 4.1: Indexing of diffraction pattern of the complex at ρ=1 [NaCl]= 300mM, to the $H^c_{I,s}$ structure.

h,k	1,0	1,1	2,0	2,1	3,0
$\sqrt{h^2+k^2+hk}$	1	$\sqrt{3}$	2	$\sqrt{7}$	3
$q^c_{hk} = q_{10} \times \sqrt{h^2+k^2+hk}$	0.834	1.445	1.668	2.206	2.502
q^o_{hk}	-	1.454	1.653	2.210	2.517

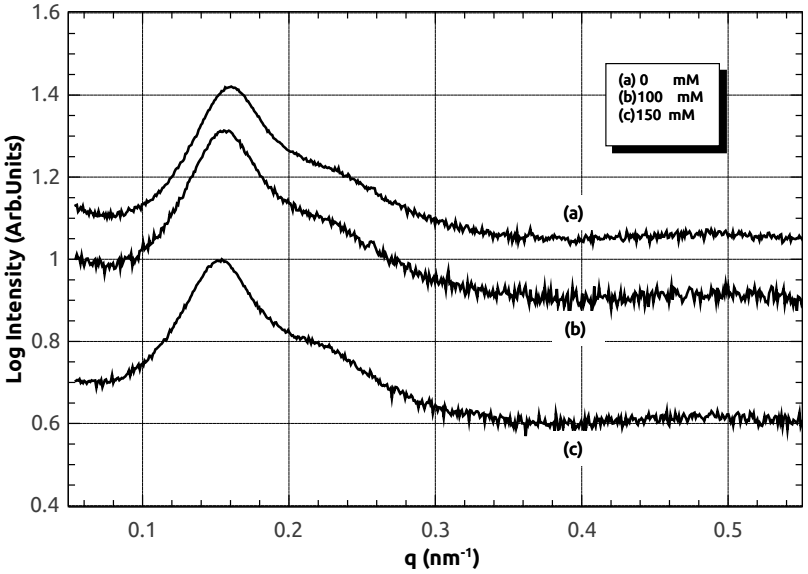

FIGURE 4.2: Diffraction patterns obtained post addition of NaCl to DTAB-DNA complex; at ρ=1;(a)[NaCl]= 0mM,(b)[NaCl]=100mM,(c)[NaCl]=150mM

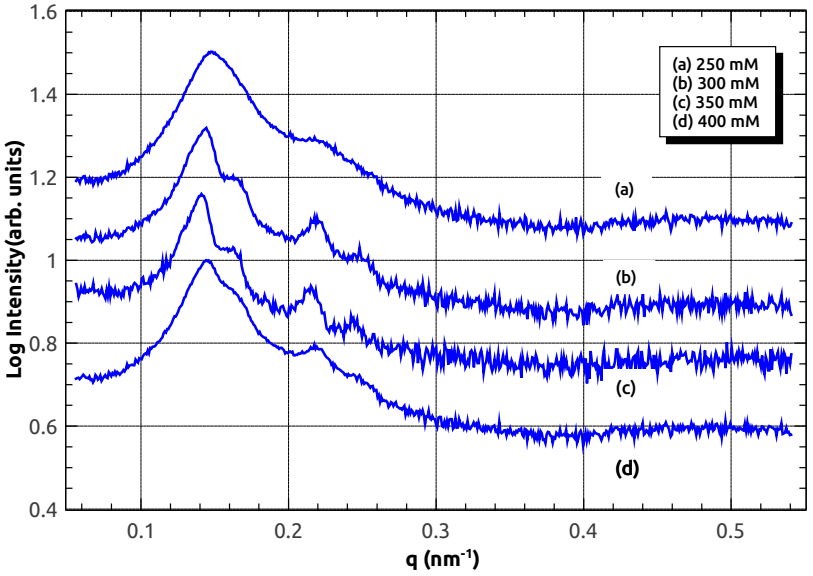

FIGURE 4.3: Diffraction patterns obtained post addition of NaCl to DTAB-DNA complex at ρ=1; (a)[NaCl]= 250mM,(b)[NaCl]= 300mM,(c)[NaCl]= 350mM,(d)[NaCl]= 400mM

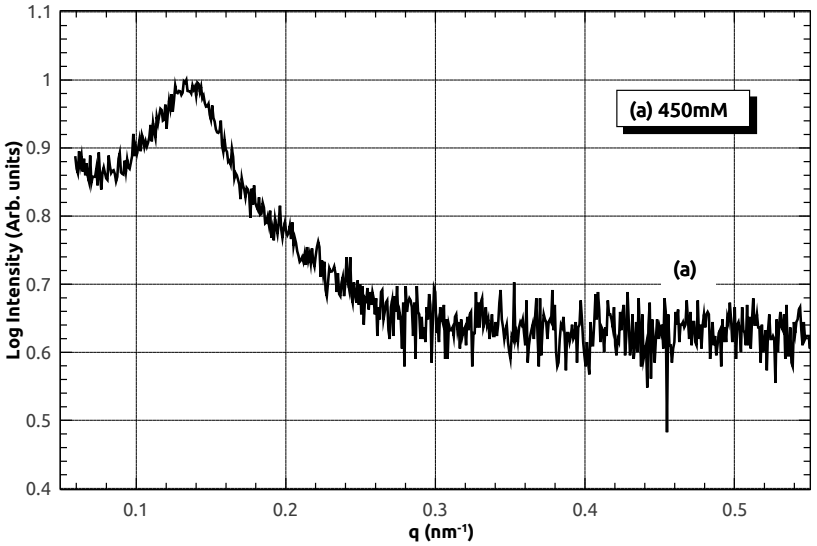

FIGURE 4.4: Diffraction patterns obtained post addition of NaCl to DTAB-DNA complex at ρ=1;(a)[NaCl]= 450mM

4.4.1.2 Phase behaviour of DTAB-DNA complex at high ρ

At ρ=4, in the absence of NaCl we again obtain "nematic-gel I". The addition of salt up to 150mM is observed to gradually cause the peak to become sharper, (Figure 4.5,(b-d)). Further addition of NaCl results in the formation of S_I^c lattice with a $\sim$ 4.06nm, (Figure 4.6,(a-c)). The lattice parameter changes slightly from a $\sim$ 4.06nm at [NaCl]=250mM to a $\sim$ 4.35nm at [NaCl]=350mM. Increase in external salt to [NaCl]=400mM results in complete loss in lattice structure and the formation of "nematic-gel II" phase, Figure 4.7.

The identification of the S_I^c phase is through indexing the relative positions of the peak to a hexagonal lattice using the relation $d_{hk} = \frac{a}{\sqrt{(h^2+k^2)}}$,where a is the lattice parameter, as shown in Table 4.2.

TABLE 4.2: Indexing of diffraction pattern of the complex at ρ=4 [NaCl]= 300mM, to the S_I^c structure

h,k	1,0	1,1	2,0	2,1
$\sqrt{h^2+k^2}$	1	$\sqrt{2}$	2	$\sqrt{5}$
$q^c_{hk} = q_{10} \times \sqrt{h^2+k^2}$	1.468	2.076	2.936	3.283
q^o_{hk}	1.468	2.073	2.931	3.281

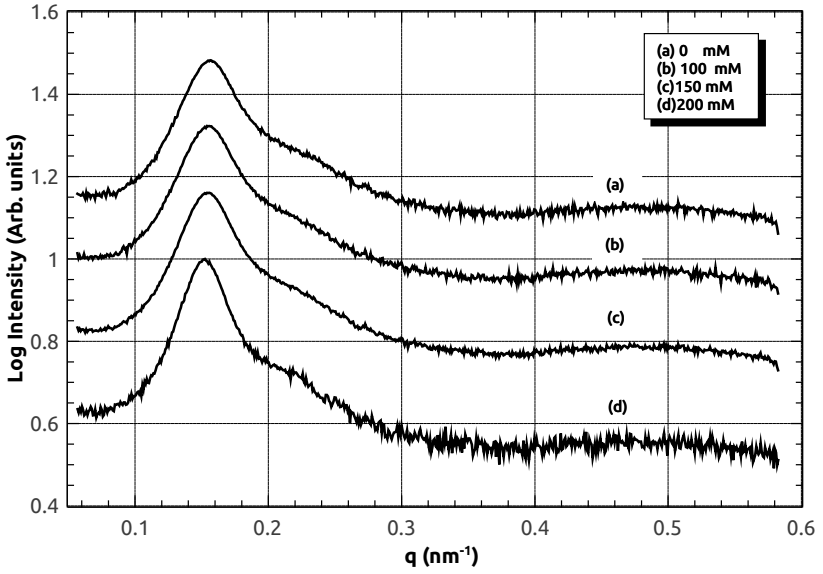

FIGURE 4.5: Diffraction patterns obtained post addition of NaCl to DTAB-DNA complex at ρ=4;(a)[NaCl]= 0mM,(b)[NaCl]= 100mM,(c)[NaCl]= 150mM,(d)[NaCl]= 200mM

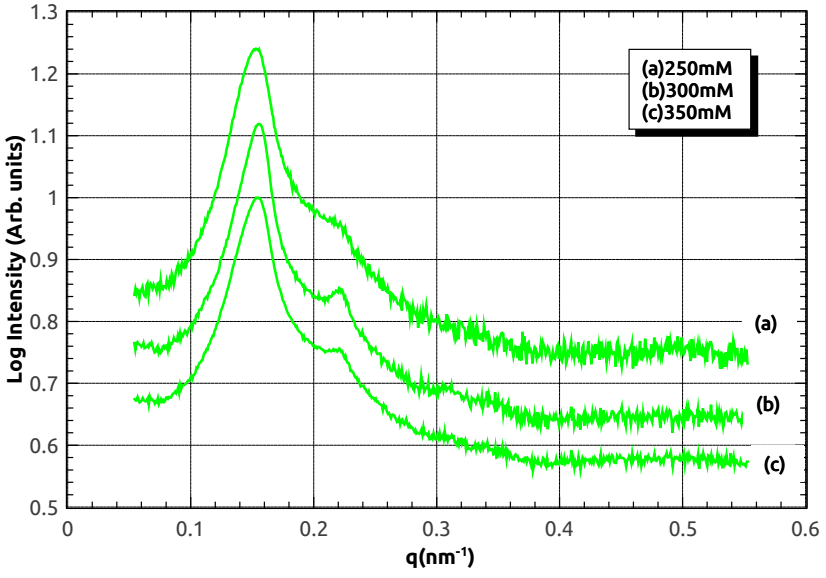

FIGURE 4.6: Diffraction patterns obtained post addition of NaCl to DTAB-DNA complex at ρ=4;(a)[NaCl]= 250mM,(b)[NaCl]= 300mM,(c)[NaCl]= 350mM.

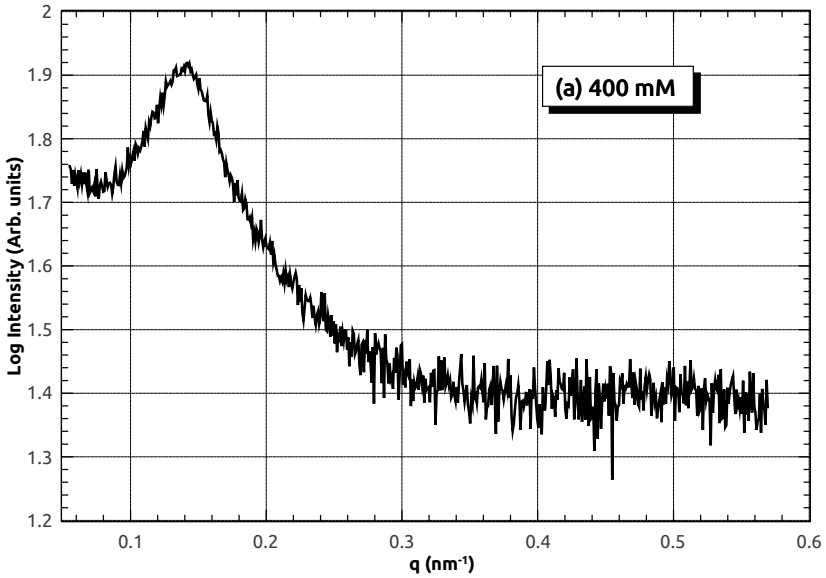

FIGURE 4.7: Diffraction patterns obtained post addition of NaCl to DTAB-DNA complex at ρ=4;(a)[NaCl]= 400mM.

4.4.2 Effect of Osmotic pressure

Osmotic pressure was applied to complexes prepared at two points in the ρ-Concentration of NaCl plane, as shown in Figure 4.8

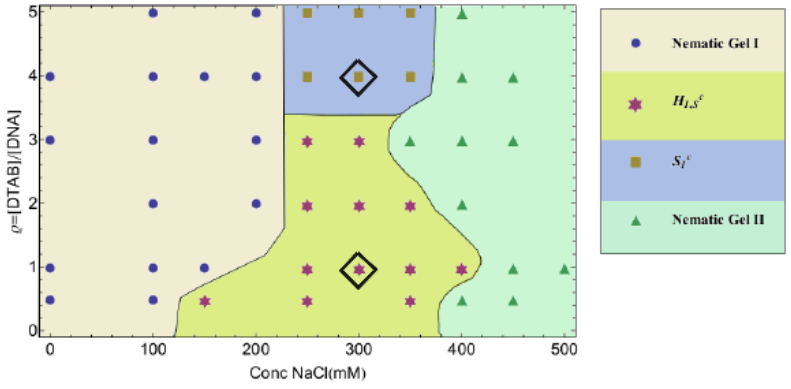

FIGURE 4.8: Phase diagram of DTAB-DNA complex in the ρ-Conc. of NaCl plane, where Open diamonds indicate points considered for studying the effect of osmotic pressure and lie at; (a)ρ=1;[NaCl]=300mM and (b)ρ=4;[NaCl]=300mM

The effect of osmotic pressure, applied using the neutral polymer PEG 8000 on DTAB-DNA complexes at ρ=1,[DTAB]=10mM,[NaCl]=300mM is presented in Table 4.3. Upon gradually increasing the osmotic pressure a slight decrease in lattice parameter from 8.67 nm at 0 wt.% to 8.56 nm at 20 wt.% of PEG8000 is noted, (Figure 4.9,(a-e)). Through the range of osmotic pressure applied the complex is capable of maintaining the $H^c_{I,s}$ superhexagonal lattice order robustly.

TABLE 4.3: Effect of Osmotic Pressure using PEG8000

Complex		**Lattice Parameter @ wt. % of PEG8000 (nm)**				
ρ	**[NaCl]mM**	**0%**	**5%**	**10%**	**15%**	**20%**
1	300	8.67 ($H^c_{I,s}$)	8.62 ($H^c_{I,s}$)	8.62($H^c_{I,s}$)	8.52 ($H^c_{I,s}$)	8.56 ($H^c_{I,s}$)

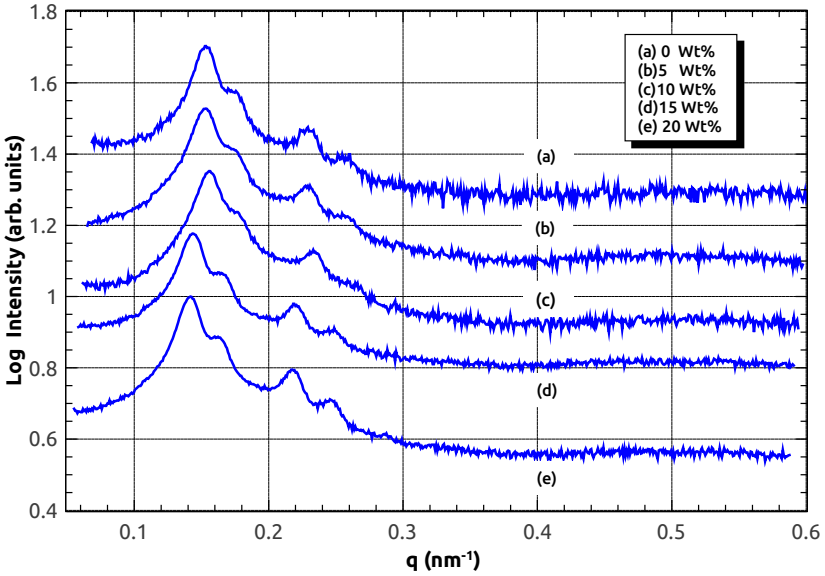

FIGURE 4.9: Diffraction patterns showing the effect of PEG8000 on $H^c_{I,s}$; ρ=1:DTAB=10mM:[NaCl]= 300mM.

The effect of osmotic pressure, applied using neutral polymer PVP 10000 on the DTAB-DNA complexes is presented in Table 4.4. For the sample prepared in the $H^c_{I,s}$ phase at ρ=1, [DTAB]=10mM, [NaCl]=300mM, the increase in osmotic pressure causes a slight change in lattice parameter from 8.67 nm at 0 wt.% to 8.47 nm at 15 wt.% of added neutral polymer, (Figure 4.10,(a-d). The higher order peaks become gradually weaker on increasing the polymer concentration till at 20wt% of PVP10000 the complex collapses into a disordered melt.

For the sample prepared in the S^c_I phase at ρ=4, [DTAB]=10mM, [NaCl]=300mM, the increase in osmotic pressure causes a slight change in lattice parameter from 4.28 nm at

TABLE 4.4: Effect of Osmotic Pressure using PVP10000

Complex		**Lattice Parameter @ wt. % of PVP10000 (nm)**				
ρ	**[NaCl]mM**	**0%**	**5%**	**10%**	**15%**	**20%**
1	300	8.67 ($H^c_{I,s}$)	8.56 ($H^c_{I,s}$)	8.47($H^c_{I,s}$)	8.47 ($H^c_{I,s}$)	Melt
4	300	4.28 (S^c_I)	4.28(S^c_I)	4.16(S^c_I)	4.11 (S^c_I)	-

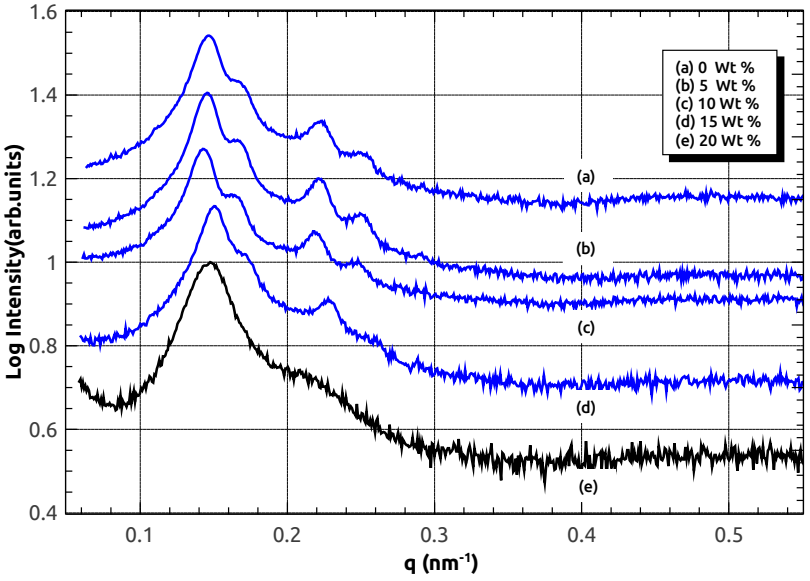

FIGURE 4.10: Diffraction patterns showing the effect of PVP10000 on $H^c_{I,s}$; ρ= 1:DTAB= 10mM:[NaCl] =300mM.

0 wt.% to 4.11 nm at 15 wt.% of neutral polymer (Figure 4.11, (a-d)). At 20 wt.% the complex becomes a highly compact structure as for the low ρ case.

4.4.3 Elemental analysis and establishment of stoichiometric ratios

Elemental analysis of DTAB-DNA complexes at different values along the ρ-[NaCl] plane was carried out. Table 4.5 contains the results. In the absence of salt, N_b/N_s decreases monotonically with increasing ρ from 1.453 at ρ=0.5 to 0.64 at ρ=5. Similar behaviour is found at [NaCl]=300mM. For a given value of ρ, N_b/N_s is slightly higher in the presence of salt.

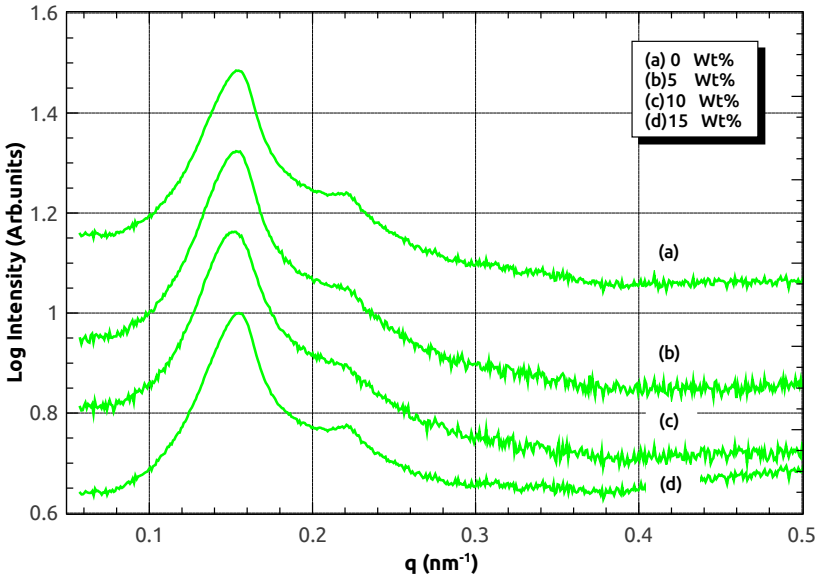

FIGURE 4.11: Diffraction patterns showing the effect of PVP10000 on S_I^c; ρ= 4:DTAB= 10mM:[NaCl] =300mM.

TABLE 4.5: Elemental analysis data of DTAB-DNA complexes

ρ	**Conc. Of NaCl mM**	**N%**	**C%**	$\mathbf{N_b/N_s}$
0.5	0	9.59	37.70	1.453
	300	4.89	18.89	1.522
1	0	6.72	28.26	1.209
	300	8.5	34.35	1.349
2	0	10.10	44.14	1.09
	300	8.73	37.3	1.157
2.5	0	8.68	42.85	0.803
	300	9.27	45.23	0.825
3	0	8.49	45.32	0.662
	300	8.38	41.93	0.775
3.5	0	10.13	54.03	0.662
	300	8.23	41.75	0.751
4	0	8.24	44.27	0.652
	300	8.68	42.85	0.762
5	0	8.13	43.94	0.642
	300	9.66	49.22	0.771

4.5 Discussion

Figure 4.1 summarizes the results of our SAXS studies on DTAB-DNA complexes. In the absence of salt a "nematic-gel" phase without long-range translational order is obtained at all values of ρ. This behaviour is very different from that of CTAB-DNA complexes discussed in the previous chapter. Thus, the reduction of the chain length

of the surfactant has a profound influence on the structure of these complexes. This most probably arises from the propensity of DTAB to form small ellipsoidal micelle. These micelles would act as cross-linkers between the stiff DNA strands leading to the formation of the nematic gel.

The addition of NaCl to the complex leads to the formation of translationally ordered structures of the complex. Interestingly two different structures are observed depending on the value of ρ. A S_I^c observed at high values of ρ whereas a $H_{I,s}^c$ structure is observed at low ρ. This behaviour is again very different that that of CTAB-DNA complexes where only the H_I^c phase is seen at all values of ρ and [NaCl]. Unlike in the CTAT-DNA system the $H_{I,s}^c$ superlattice complex in the present case does not transform into the H_I^c structure on applying an osmotic pressure. This observation is consistent with the absence of a H_I^c phase in the phase diagram shown in Figure 4.1. It is possible that the reduced micellar size leads to an increased DNA-DNA repulsion that would favour the S_I^c phase over the H_I^c phase. However, it is not clear why this system forms the $H_{I,s}^c$ in the presence of salt at low ρ. The ratio N_b/N_s can be estimated for the S_I^c as in the case of CTAB-DNA case described in the previous chapter. Due to the shorter chain length of DTAB N_b/N_s turns our to be around 0.4 which is slightly larger than the value of 0.3 obtained for CTAB-DNA complexes. If the $H_{I,s}^c$ has a structure similar to that proposed for CTAT-DNA complexes one would expect N_b/N_s to have a value of 0.8 . The observed values for the S_I^c phase which occurs for ρ >3 are around 0.65 which is much above the expected value of 0.4 . This discrepancy might arise from the tendency of DTAB to form ellipsoidal micelles instead of long cylindrical ones. At lower values of ρ in the superhexagonal phase N_b/N_s varies from 1.45 to 0.8 as ρ is varied from 0.5 to 2.5 . The N_b/N_s value at ρ=2.5 is in fair agreement with what is proposed for the $H_{I,s}^c$. The increase in N_b/N_s at lower values of ρ might arise from vacancies in the lattice at the micellar sites as was proposed in the earlier chapter. Interestingly, in the presence of NaCl N_b/N_s values are found to slightly increase for all values of ρ, a trend opposite to what is seen in CTAB-DNA complexes. We do not at present understand the origin of this difference.

4.6 Conclusions

The phase diagram of DTAB-DNA complexes along the ρ-Concentration of NaCl plane is established. The phase behaviour of this system is very different from that of CTAB-DNA complexes indicating the important role played by the surfactant chain length in determining the structure of these complexes. Elemental analysis studies indicate that the stoichiometry of these complexes is fairly fixed in the S_I^c structure but varies by almost a factor of 2 in the $H_{I,s}^c$ phase.

Bibliography

[1] R. Chatterjee and D. K. Chattoraj, *Biopolymers*, **18(1)**, 147 (1979).

[2] A. V. Radhakrishnan, PhD thesis: Investigations on the polymorphism of surfactant DNA complexes, Jawaharlal Nehru University, New Delhi, Chapter 5.

[3] S. Z. Bathaie, A. A. Moosavi-Mohavedi and A. A. Saboury, *Nucleic Acids Res.*, **27(4)**, 1001 (1999).

[4] D. M. McLoughlin, A. V. Gorelov and K. A. Dawson, *Prog. Colloid Polym. Sci*, **118**, 226, (2001).

[5] J. Courtois and J. F. Berret, *Langmuir*, **26(14)**, 11750 (2010).

[6] J. Zhang, D. J. F. Taylor, P. X. Li, R. K. Thomas and J. Penfold, *Langmuir*, **19(9)**, 3712 (2003).

[7] J. Zhang,D. J. F. Taylor, P. X. Li, R. K. Thomas, J. B. Wang and J. Penfold, *Langmuir*, **24(5)**, 1863 (2008).

[8] J. Oremusova, *Tenside Surfactants Detergents*, **49(3)**, 231, (2008).

[9] E. Acosta, A. Mesbah and T. Tsui, *J. Surf. Det.* , **9(4)**, 367 (2006).

[10] S. Y. Ran, Y. W. Wang, G.C.Yang and L.X.Zhang*J. Phys. Chem. B.*, **115(16)**, 4568 (2014).

[11] R. Dias, K. Dawson and M. G.Miguel, *DNA interactions with Polymers and Surfactants, edited by R. Dias and B. Lindman*, John Wiley and Sons Inc. (2007).

Chapter 5

Structure and modelling of centred rectangular phase of Vitamin D3 doped bilayers

5.1 Introduction

Cholesterol has a number of derivatives that are of vital importance that form as a response to a range of environmental triggers. Secosteroids are derived by cleaving one of the rings of the bulky steroid core in cholesterol. Vitamin D3 is a typical example where the B-ring is cleaved. This occurs naturally in biological systems as a result of exposure to ultraviolet radiation [1] and derivatives of vitamin D3 are highly effective in differentiation and proliferation of epidermal cells [2, 3]. Further the synthesis of vitamin D3 from its precursor is seen to be enhanced in liposomal preparations made of distearoyl phosphatidycholine(DSPC 18:0) [4]. Cholesterol and its derivatives have been known to regulate the physical characteristics of lipid membranes strongly and have been implicated as key players in the processing and functioning of a range of biologically relevant phenomenon [5].

5.2 Earlier Studies

Some lipids, like DSPC and DPPC, are capable of displaying tilt order of chains with respect to the bilayer normal. In these cases in addition to the main transition from the gel to fluid phase ($L_\beta \rightarrow L_\alpha$) they display a pre-transition through the formation of an intermediate tilted gel phase ($L_\beta \rightarrow P_{\beta'} \rightarrow L_\alpha$), whose structure is shown in Figure 5.1 (a). The addition of cholesterol to the bilayer was also seen to induce in addition to the $P_{\beta'}$ a symmetric height modulated phase P_β (Figure 5.1 (b)). These structures arise due to a coupling between the tilt field and the bilayer height profile [6, 7]. Theoretical considerations dealing with the energetics of modulations of the lipid bilayer had long posited the possible existence of a thickness modulated phase [8] as well as height modulated phases [6, 9]. Although height modulated phases of bilayer have been reported widely in the literature [10–12], there has only been one report of the thickness modulated phase [13]

It has been noted that even low concentrations of certain sterols like 25-hydroxycholesterol and 25-OH-D3 completely abolish the pre-transition and split the main transition of certain lecithins and severely disrupt lipid organization [14]. The effect of secosteroids, cholecalciferol(VitaminD3),in Figure 5.2(b)) and ergocalciferol(vitamin D2), on dipalmitoyl phosphatidylcholine (DPPC)(Fig.1.8,(c)) has been looked at previously [13]. A partial phase diagram on the temperature-sterol mole fraction(ϕ_{cc}) plane has been constructed (Figure 5.3) based on diffraction data from aligned multilayers [13]. At sterol mole fraction (ϕ_{cc}) between 5-10 mol% the asymmetric ripple phase $P_{\beta'}$, is found. Increasing ϕ_{cc} (12.5-17.5 mol%) is seen to induce a symmetric ripple phase P_β. At higher ϕ_{cc} ($\geq$17.5mol%) a ripple phase $P^*_{\beta'}$ with ripple wavelength roughly half that of the $P_{\beta'}$ phase is observed which transforms to a centred rectangular (RC) phase on increasing temperature. The RC phase was noted to be composed of thickness modulated bilayers locking into a centred rectangular lattice, as shown in Figure 5.1 (c).

5.3 Aim of the present studies

In this chapter we propose a simplistic model to describe the RC phase. The intensities were calculated from a proposed model to describe the structure, which were compared with experimental data to estimate the relevant physical parameters .

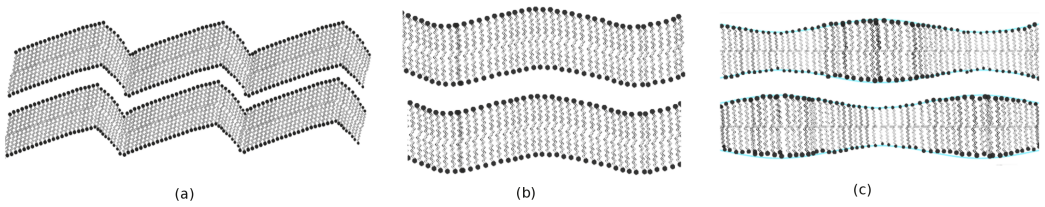

FIGURE 5.1: Schematic diagram showing (a) asymmetric ripple $P_{\beta'}$ phase (b) symmetric height modulated P_{β} phase and (c) thickness modulated RC phase.

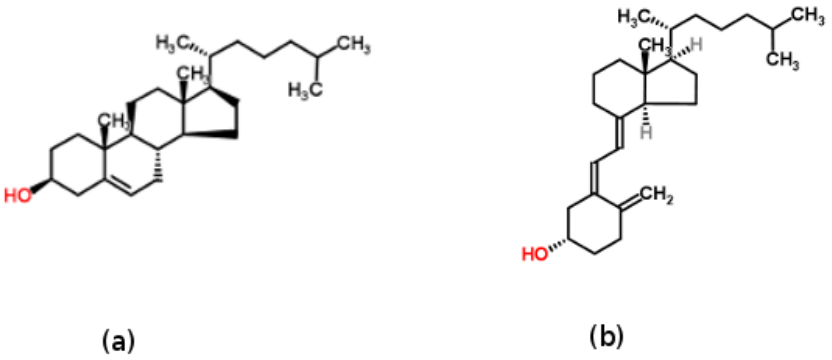

FIGURE 5.2: Structure of (a)Cholesterol and (b)Cholecalciferol (vitamin D3)

5.4 Materials and Methods

Vitamin D3 and dipalmitoyl phosphatidylcholine (DPPC) were procured from Sigma-Aldrich. All chemicals were used as received. Stock solutions of lipid and sterol were prepared in HPLC chloroform and aliquoted to reach the desired compositions keeping the concentration of the total lipid at 1 mg/mL. The lipid sterol mixture was then coated on the side of a beaker (radius $\sim$ 1cm) to create a patch of area roughly 15-20 mm^2. The beaker was then kept in an evacuated chamber for approximately 24hrs to facilitate complete evaporation of the chloroform. The samples were then sealed in a larger beaker with a water reservoir and let to anneal at temperatures above the effective fluidization temperatures of the particular mixture to form extended bilayer stacks. The samples

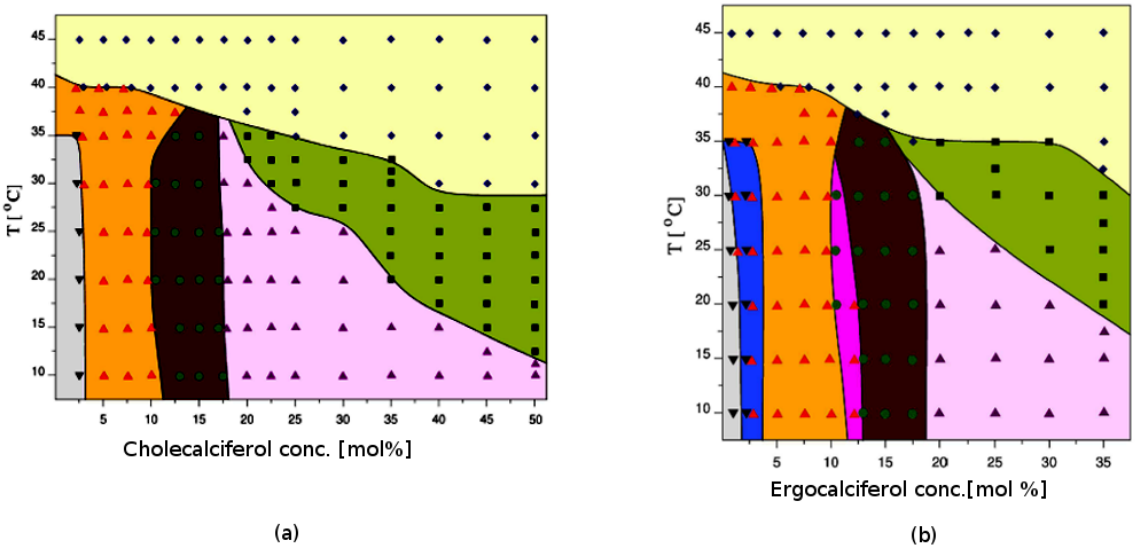

FIGURE 5.3: Partial phase diagrams of (a)DPPC- vitamin D3 (b)DPPC- vitamin D2. From [13] where (▼) $L_{\beta'}$, (▲) $P_{\beta'}$, (●) P_{β}, (▲) $P^{*}_{\beta'}$, (■) RC and (♦) L_{α} .

were then loaded into a humidity and temperature controlled chamber for the small-angle x-ray scattering studies keeping the relative humidity(RH) at $\sim 98\%$. The RH in the chamber was maintained by placing a reservoir of millipore water and allowing the sample in the chamber to equilibrate through the course of the experiment.

5.5 Results

X-ray diffraction patterns were collected at different points on the composition-temperature plane of DPPC-vitamin D3 phase diagram. These results are consistent with the phase diagram Figure 5.3.

5.6 Modelling and analysis of the RC phase

In this section, we model the RC phase. We describe the bilayer by assigning one delta function to the bilayer mid-plane and one each to the two headgroup regions. The distribution of vitamin D3 in the membrane is likely to be non-uniform due to the thickness modulation. However, since the difference in electron density between the lipid and vitamin D3 is negligible we neglect any in-plane modulations in the electron densities of the chain and headgroup regions. Figure 5.5 shows the electron density of

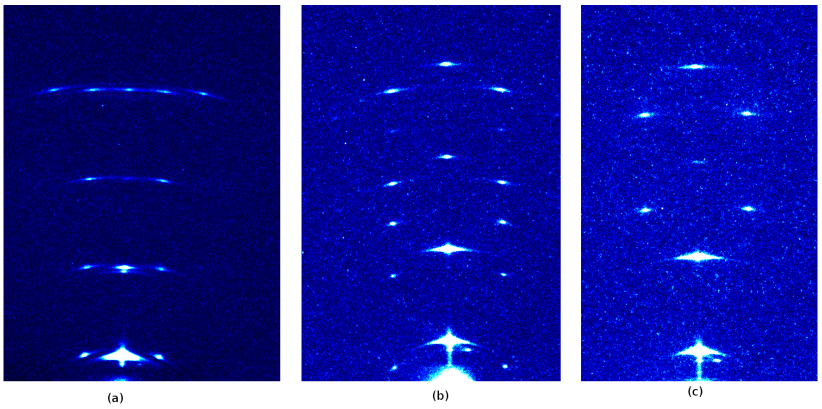

FIGURE 5.4: Diffraction patterns obtained from aligned multilayers of DPPC-vitamin D3 at different points along the temperature-composition plane. (a)$P_{\beta'}$ at ϕ_{cc}=15mol%, T=15°C. (b)$P_{\beta'}$ at ϕ_{cc}=7.5mol%. T=15°C. (c)RC phase at ϕ_{cc}=45mol%,T=15°C.

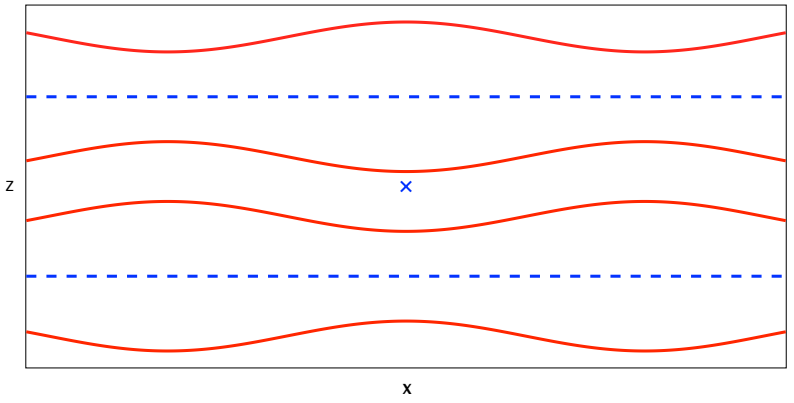

FIGURE 5.5: Model of the electron density of the RC phase. The dashed lines in blue represent the mid-planes of the bilayers whereas the red solid lines correspond to the headgroup regions.

the RC phase used in the calculation. It consists of a stack of bilayers along z with each bilayer height modulated along x. Adjacent bilayers are shifted along x such that the minimum thickness of one layer matches with the maximum thickness of the adjacent bilayer. The electron density of each bilayer consists of a delta function at its mid-plane and two delta functions corresponding to the headgroup regions. The lattice is built through the stacking of two bilayers corresponding to the periodicity of 2d where d is the separation between the mid-planes of adjacent bilayers.

The electron density of the repeating motif is given by,

$$\rho(x,z) = \rho_c\left[\delta\left(z-\frac{d}{2}\right)+\delta\left(z+\frac{d}{2}\right)\right] + \rho_h\left[\delta\left(z-\frac{d}{2}-\frac{\delta_h}{2}-ACos[q_x^0 x]\right)+\delta\left(z-\frac{d}{2}+\frac{\delta_h}{2}+ACos[q_x^0 x]\right) + \delta\left(z+\frac{d}{2}-\frac{\delta_h}{2}+ACos[q_x^0 x]\right)+\delta\left(z+\frac{d}{2}+\frac{\delta_h}{2}-ACos[q_x^0 x]\right)\right] \quad (5.1)$$

where, ρ_h and ρ_c are the electron densities of the headgroup and the bilayer mid-plane respectively.

The Fourier transform of the above gives the form factor,

$$F(q_x,q_z) = \rho_c\left(e^{iq_z\frac{d}{2}}+e^{-iq_z\frac{d}{2}}\right)2\pi\delta(q_x) + \rho_h\left[e^{iq_z(\frac{d}{2}+\frac{\delta_h}{2}+ACos[q_x^0 x])} + e^{iq_z(\frac{d}{2}-\frac{\delta_h}{2}-ACos[q_x^0 x])} + e^{-iq_z(\frac{d}{2}-\frac{\delta_h}{2}+ACos[q_x^0 x])} + e^{-iq_z(\frac{d}{2}+\frac{\delta_h}{2}-ACos[q_x^0 x])}\right] \quad (5.2)$$

Using the Jacobi Anger expansion,

$$e^{izCos[\theta]} = \sum_{n=-\infty}^{\infty} i^n J_n(z) e^{in\theta} \quad (5.3)$$

We get

$$F(q_x,q_z) = 4\pi\rho_c Cos\left[\frac{q_z d}{2}\right]\delta(q_x) + 4\pi\rho_h Cos\left[q_z\frac{d+\delta_h}{2}\right]\sum_n (i)^n J_n(q_z A)\delta(q_x+q_x^0)] + 4\pi\rho_h Cos\left[q_z\frac{d-\delta_h}{2}\right]\sum_n (-i)^n J_n(q_z A)\delta(q_x+q_x^0)] \quad (5.4)$$

Using trigonometric relations this can be simplified to

$$\begin{aligned} F(q_x, q_z) = 4\pi\rho_c Cos\left[\frac{q_z d}{2}\right]\delta(q_x) \\ + 8\pi\rho_h Cos\left[q_z\frac{d}{2}\right]Cos\left[q_z\frac{\delta_h}{2}\right]\sum_{n-even}(i)^n J_n(q_z A)\delta(q_x + q_x^0) \\ + 8\pi\rho_h Sin\left[q_z\frac{d}{2}\right]Sin\left[q_z\frac{\delta_h}{2}\right]\sum_{n-odd}(i)^n J_n(q_z A)\delta(q_x + q_x^0) \end{aligned} \tag{5.5}$$

The reciprocal lattice of the system can be written as,

$$S(q_z) = \sum_h \delta(q_z - hq_z^0), \quad where \quad q_z^0 = \frac{\pi}{d} \tag{5.6}$$

Evaluating Equation 5.5 at the reciprocal lattice points given by Equation 5.6, we get

$$F(n-odd, h-odd) = (-1)^{h-1} 8\pi\rho_h Sin\left[\frac{\pi h\delta_h}{2d}\right] \times \sum_{n-odd}(i)^n J_n(q_z A)\delta(q_x + q_x^0) \tag{5.7}$$

$$F(n{-}even, h{-}even) = (-1)^{h-1}4\pi\rho_c\delta(q_x){+}(-1)^{h-1}8\pi\rho_h Cos\left[\frac{\pi h\delta_h}{2d}\right]\times\sum_{n-even}(i)^n J_n(q_z A)\delta(q_x{+}q_x^0) \tag{5.8}$$

where $\alpha = \delta_h/d$ and $\beta = A/d$. The above equations 5.7 and 5.8 give the structure factor of the reflections and are used to generate the the amplitudes of the peaks. As can be seen from the equations the amplitudes are non-zero only when $h + n = even$, which is consistent with the centred rectangular symmetry of the system. In order to the fit the observed structure factors ($|F_o^{hk}| = \sqrt{I^{hk}}$) and those calculated ($|F_c^{hk}|$) we define a measure,

$$\Sigma = \sum_{h,k} ||F_c^{hk}| - |F_o^{hk}||^2 \tag{5.9}$$

and minimize it employing a non-linear least squares fitting method (Levenberg-Marquardt algorithm) from the Experimental Data Analyst(EDA) package, Mathematica . The adjustable parameters in the model are: α, β and ρ_c/ρ_h. The best fit values of the intensities are given in Table 5.1. Values of the model parameters obtained are: α = 0.836, $\beta = 0.072$ and ρ_c/ρ_h = -0.01 . Since $d = 5.43$ nm, amplitude of the thickness modulation $A = 0.39$ nm and the bilayer thickness $\delta_h = 4.54$ nm. This value of δ_h is in good agreement with those reported in literature [10, 11]. However, the value of ρ_c/ρ_h is not. This discrepancy most probably arises from the use of the simplistic 3-delta function model employed here. The phases for the reflections were obtained from the calculated structure factors, $e^{i\phi^{hk}} = \frac{F_c^{hk}}{|F_c^{hk}|} = \pm 1$, and combined with the observed magnitudes(F_0^{hk}) and inverse Fourier transformed to generate the two-dimensional electron density map, Figure 5.6, using the expression,

$$\rho(x,z) = \sum_{h,k} F_o^{hk} e^{i\phi^{hk}} Cos[q_x^{hk}x + q_z^{hk}z] \tag{5.10}$$

The map portrays the RC phase as a thickness modulated bilayer where the adjacent bilayers are shifted by half the wavelength of modulation. The black line serves as a visual aid to identify the bilayer. The artefactual intensity modulation seen along the direction of modulation arises due to truncation errors from having only a small number of peaks.

TABLE 5.1: Observed and calculated intensities of the diffraction peaks in the centred rectangular phase of DPPC - vitamin D3 membranes

h	n	I_o	I_c	ϕ^{hk}
2	0	100	100	-
4	0	26.5	26.13	-
6	0	0.0	0.01	
8	0	2.5	3.50	-
10	0	0.0	0.77	
1	1	0.0	1.07	
3	1	0.0	7.74	
5	1	2.8	2.64	-
7	1	1.5	2.50	+
2	2	0.0	0.04	
4	2	0.0	0.43	
6	2	0.0	0.00	
8	2	0.0	0.28	

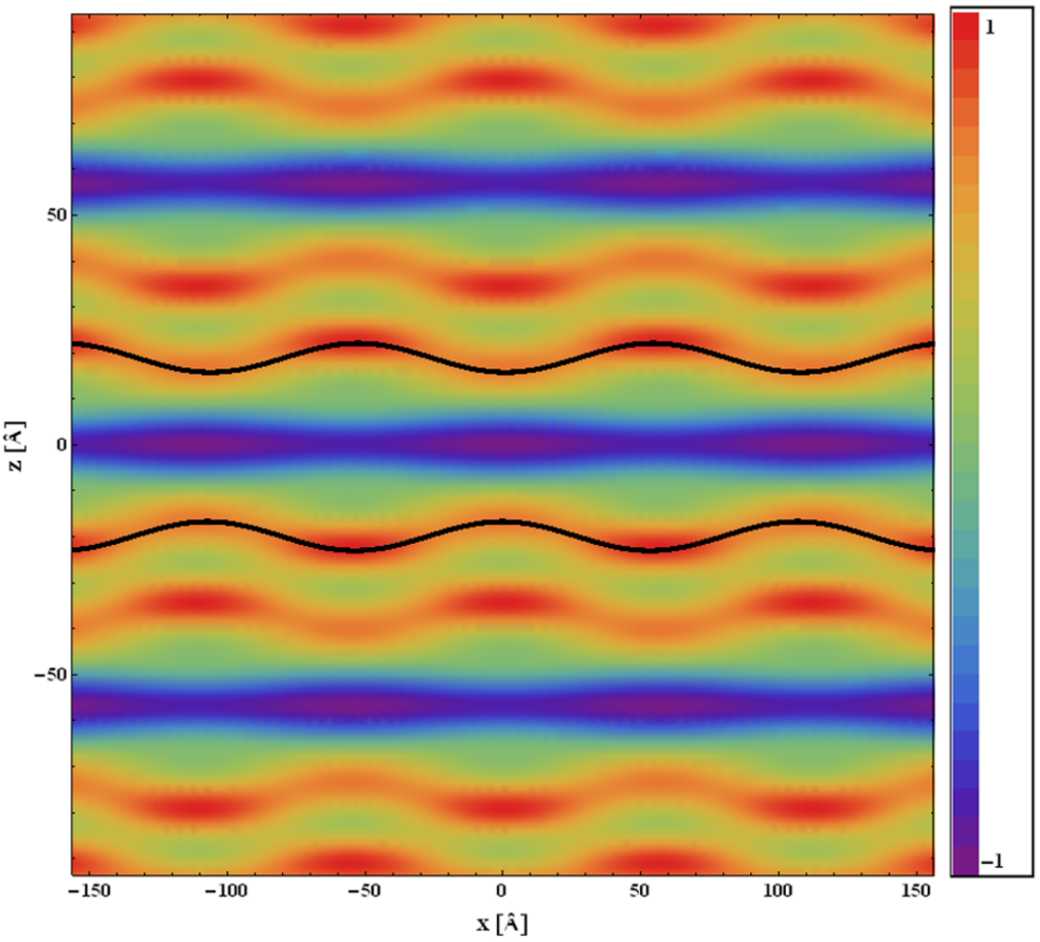

FIGURE 5.6: Electron Density map obtained for the RC phase

5.7 Conclusions

The diffraction patterns for centred rectangular phase of DPPC-vitamin D3 bilayers were collected. We also presented an electron density model for the structure of this phase. By comparing the observed intensities of the peaks with those calculated from the model we obtain estimates for the parameters: α, β and ρ_c/ρ_h. Further we generate an electron density map by combining the calculated phases (ϕ^{hk}) and the observed amplitudes of the different peaks.

Bibliography

[1] M. F. Holick, *Am. J. Clin. Nutr.*, **60**, 619 (1994).

[2] K. Merz and B. Sternberg, *J. Drug Targ.*, **2**, 411 (1994).

[3] V. W. Thompson and H. F. DeLuca, *J. Biol. Chem.*, **239(4)**, 984 (1964).

[4] X. Q. Tian and M. F. Holick, *J. Biol. Chem.*, **274(7)**, 4174 (1999).

[5] E. Ikonen, *Nature Rev. Mol. Cell. Biol*, **9**, 125 (2008).

[6] T. C. Lubensky and F. C. Mackintosh, *Phys. Rev. Lett.*, **71**, 1565 (1993).

[7] K. Sengupta, V. A. Raghunathan and Y. Hatwalne, *Phys. Rev. Lett.*, **87**, 055705 (2001)

[8] R. E. Goldstein and S. Leibler, *Phys. Rev. Lett.*, **61**, 2213 (1988).

[9] N. Shimokawa, S. Komura and D. Andelmann, *Eur. Phys. J. E.: Soft Matter Biol. Phys.* , **26**, 197 (2011).

[10] W. J. Sun, S. T. Nagle, R. M. Suter and J. F.Nagle, *Proc. Natl. Acad. Sci.* , **93(14)**, 7008 (1996).

[11] G. Pabst, M. Rappolt, H. Amenitsch and P. Laggner, *Phys. Rev. E*, **62**, 4000 (2000).

[12] K. Sengupta, V. A. Raghunathan and J. Katsaras, *Phys. Rev. E*, **68**, 031710 (2003).

[13] M. A. Kamal, A. Pal and V. A. Raghunathan, *Soft Matter*, **8**, 11600 (2012).

[14] S. P. Verma, J. R. Phillipot and D. F. H. Wallach, *Biochemistry*, **22**, 4587 (1983).

Chapter 6

Influence of 25-hydroxycholesterol and 27-hydroxycholesterol on DLPC and POPC membranes

6.1 Introduction

The embedding of "membrane-active" molecules has been known to strongly perturb the equilibrium phases of lipid bilayers. Cholesterol, having eight chiral centres, is believed to be capable of selective partitioning and inducement of lipidic phases and "raft-like" domains. These domains subsequently could behave as highly relevant and functional platforms for a range of biomimetic processes [1]. Further, oxygenated derivatives of cholesterol, are capable of anchoring in membranes in a wide range of interfacial states, strongly influencing membrane dynamic properties[2, 3]. In cells the physical interplay at the membrane is exploited whereby apoptosis is noted through the addition and regulation of oxysterols that inhibit "raft-formation"[4, 5].

6.2 Previous Studies

The effect of oxygenated derivatives of Cholesterol, 25-hydroxycholesterol (25-HC) and 27-hydroxycholesterol(27-HC) (Figure.6.1), on a wide range of lipids has been probed from different experimental and computational angles. Partial phase diagram of binary mixtures 25-HC and 27-HC with DPPC and DMPC, using small-angle x-ray scattering methods, across the temperature-composition plane have been established [6, 7].In both studies the sterols are found to severely change the ripple characteristics of the pretransitional phase of the native lipid and also induce a fluid-fluid coexistence well above the main transition temperature. Molecular dynamics studies have indicated that the orientation of cholesterol is along the bilayer normal, anchored at the bilayer water interface. Similar studies on 25-HC show that due to the presence of a second hydroxyl group at the end of the aliphatic chain they are capable of adopting different orientations in the bilayer. The first being similar to the Cholesterol molecule, the second taking an inverted orientation with respect to the bilayer normal with the second hydroxyl group anchored at the interface and a third orientation where both hydroxyl groups anchor at the interface describing the "boat" configuration. There is also a thinning of the membrane thickness occuring due to the possible formations of dimers of sterol molecules [8]. The complete structural features of lipid bilayers considered in our study, DLPC and POPC, have been accurately characterized earlier [9, 10].

6.3 Aim of Present Studies

The main aim of the present studies is to probe the influence of chain length and chain unsaturation on the phase behaviour of binary oxysterol - lipid membranes. In these studies we use DLPC which contains two 12-carbon chains, instead of DMPC and DPPC used in earlier studies that contain longer chains. To probe the role of chain unsaturation, we use POPC,which contains one unsaturated chain and one saturated chain. .

6.4 Materials and Methods

25-hydroxycholesterol (25-HC), 27-hydroxycholesterol(27-HC), dilauroyl phosphatidylcholine(DLPC) and 1-palmitoyl 2-oleoyl phosphatidylcholine(POPC)were procured from

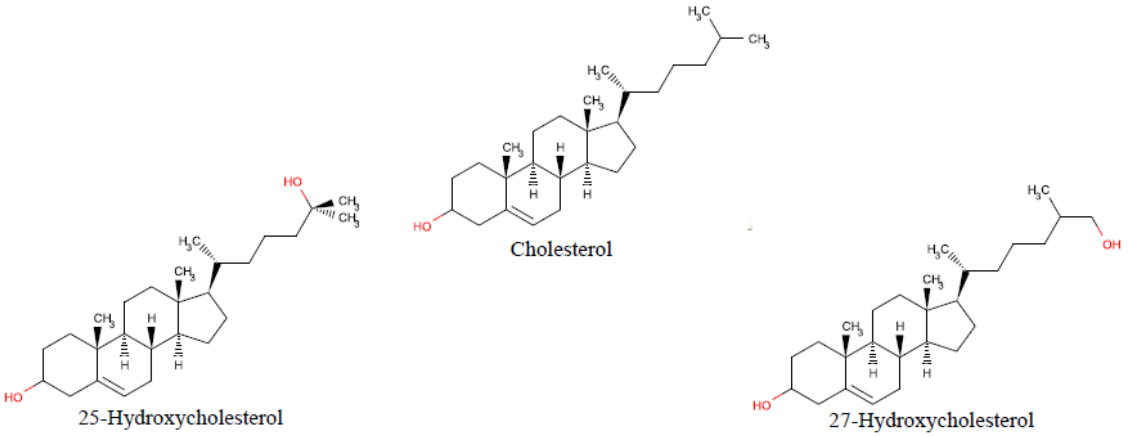

FIGURE 6.1: Structures of Cholesterol, 25-hydroxycholesterol and 27-hydroxycholesterol. Figure adapted from [8]

Sigma-Aldrich. All chemicals were used as received. Stock solutions of all lipids and sterols were prepared in HPLC grade chloroform and aliquoted to reach the desired compositions. Aligned Bilayer stacks were prepared using the protocol described in the previous chapter. The samples are then sealed in a larger beaker with a water reservoir and let to anneal at temperature above the effective fluidization temperatures of the particular mixtures to form extended equilibrium bilayer stacks. The samples are then loaded into a humidity and temperature controlled chamber for the small-angle x-ray scattering studies.

6.5 Results

6.5.1 Phase diagram of 25-HC DLPC binary mixtures

A partial phase diagram of 25-hydroxycholesterol - DLPC binary mixtures across the composition-temperature plane, deduced from SAXS data, is shown in Figure 6.2. At low sterol concentration, X_c=5 mol%, there is no significant change in the phase behaviour of DLPC. For X_c=10 mol%, we observe two sets of peaks with lamellar periodicities of d1 $\sim$ 50.1 Å and d2 $\sim$ 47.1Å,above the main transition temperature of pure DLPC (T_m=-2°C). At higher temperatures, the regime of coexistence ends giving a single set of peaks with a reduced periodicity of d $\sim$ 46.1Å. The extent of the two phase region is

noted to be gradually increasing with sterol concentration ,with the high temperature single phase appearing only at T $\sim$ 45°C at X_c=15 mol%. Further increase in X_c results in a gradual diminishing of the two phase coexistence region. At X_c=25 mol%, the two phase region is completely abolished and we see uniform fluid L_α behaviour at all temperatures.

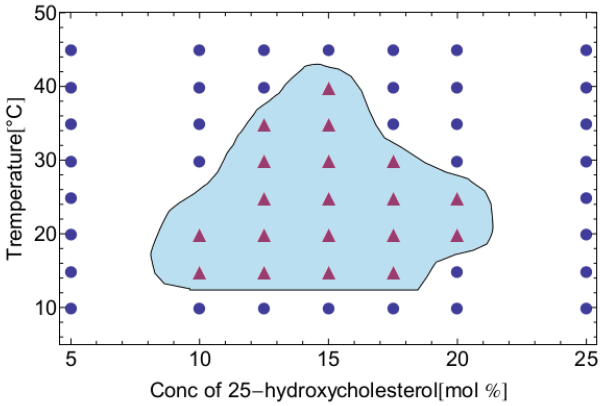

FIGURE 6.2: Partial phase diagram of 25-hydroxycholesterol - DLPC bilayers. Coexistence of two fluid phases is seen over the shaded region (▲) and single lamellar phase over the rest (●).

6.5.2 Characteristic x-ray diffraction patterns for 25-HC - DLPC bilayers

Figure 6.3 portrays the typical x-ray patterns observed at X_c=15 mol % across the fluid-fluid coexistence region. At high temperatures, a single periodicity of d $\sim$ 46.1Å is noted ((h) in Figure 6.3). A second set of peaks appear across the two phase region ((g) to (b) in Figure 6.3) which disappears to give a uniform low temperature phase with d $\sim$ 49.4Å ((a) in Figure 6.3).

Table 6.1 lists the periodicities observed along the composition-temperature plane for 25-HC DLPC bilayers.

6.5.3 Electron density profiles for 25-HC DLPC bilayers

The relative electron density profiles (edp) calculated for 25-HC DLPC at X_c=15 mol% and X_c=17.5 mol%, after correct phase allocation are shown in Figure 6.4 and Figure 6.5, respectively. The edps are evaluated for the low temperature and the high temperature

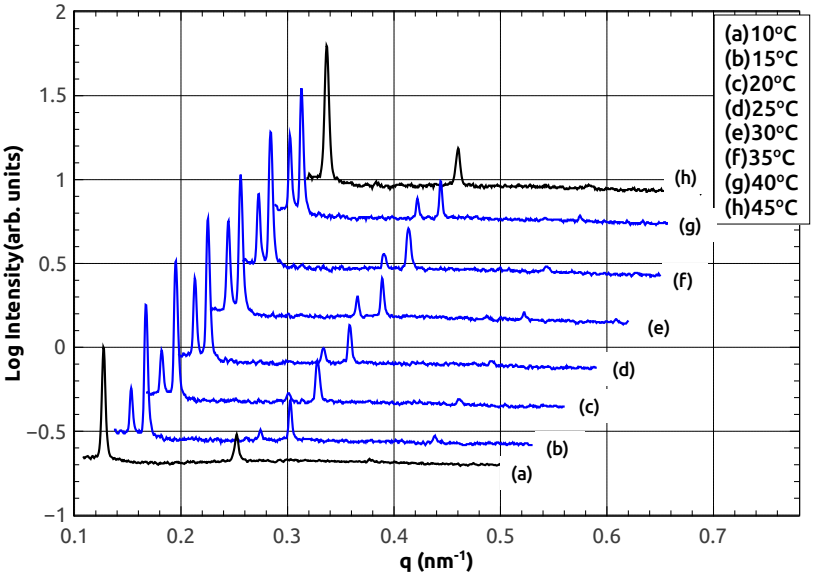

FIGURE 6.3: Characteristic x-ray diffraction patterns of 25-HC DLPC bilayers at X_c=15 mol% at different temperatures

TABLE 6.1: Lamellar spacings d(Å) of 25-HC DLPC bilayers as a function of temperature

T[°C]	X_c(mol %)						
	5	10	12.5	15	17.5	20	25
45	46.4	46.1	46.1	46.6	47.1	47.4	48.3
40	-	46.1	46.6	51.5,46.1	47.1	47.7	-
35	46.6	49.9,46.1	50.3,45.9	50.5,46.1	47.7	50.1	47.9
30	46.6	49.7,46.4	50.3,45.9	51.3,46.4	51.3,47.1	50.1	47.9
25	47.1	-	51.1,46.1	52.3,46.7	51.3,47.4	50.3,47.8	48.7
20	46.9	50.1,47.1	51.5,46.6	50.5,46.8	51.6,47.4	50.3,47.8	49.1
15	47.1	51.1,47.1	51.5,47.1	51.5,46.8	52.5,47.2	51.0	51.1
10	47.4	47.7	48.9	49.4	50.3	50.8	51.6

fluid L_α phases and also across the two-phase coexistence region. Table 6.2 contains the values for Headgroup spacing(d_{hh}).

TABLE 6.2: d_{hh}[Å] for 25-HC DLPC bilayers as a function of temperature

X_c=15 mol%		**X_c=17.5 mol%**	
T [°C]	**d_{hh}[Å]**	**T [°C]**	**d_{hh}[Å]**
45	29.7	40	29.98
20	31.32	20	31.64
	35.74		36.08
10	32.2	10	32.40

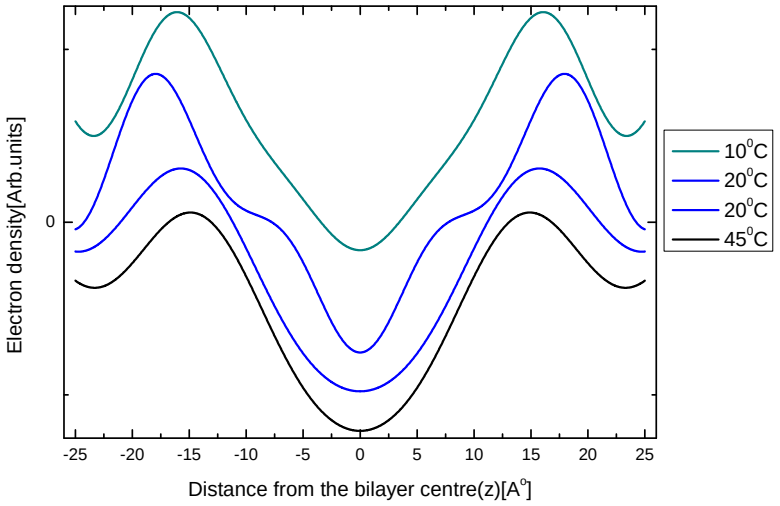

FIGURE 6.4: Trans-bilayer electron density profile of 25-HC DLPC [X_c=15 mol %] bilayers across different temperatures spanning the two-phase coexistence region

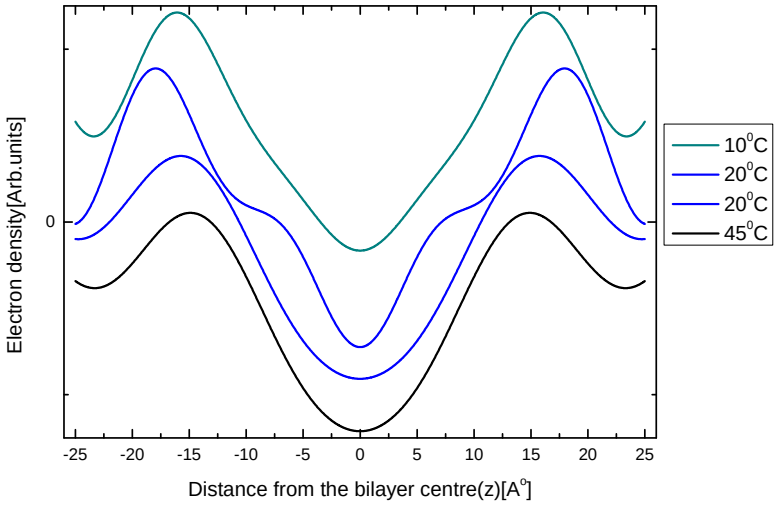

FIGURE 6.5: Trans-bilayer electron density profile of 25-HC DLPC [X_c=17.5 mol %] bilayers across different temperatures spanning the two-phase coexistence region

6.5.4 Effect of doping DLPC with 27-HC and POPC with 25-HC and 27-HC

27-HC DLPC mixtures were studied at two different sterol concentrations of X_c =15 mol% and X_c =17.5 mol% over a temperature range from 10°C to 45°C. These mixtures do not show phase separation over this temperature range and only a single lamellar phase is observed, as shown in Figure 6.6. Binary mixtures of 25-HC POPC and 27-HC POPC were also studied at X_c= 15 mol%. These systems too show only a single lamellar phase over a temperature range from 10°C to 45°C, as shown in Figure 6.7.

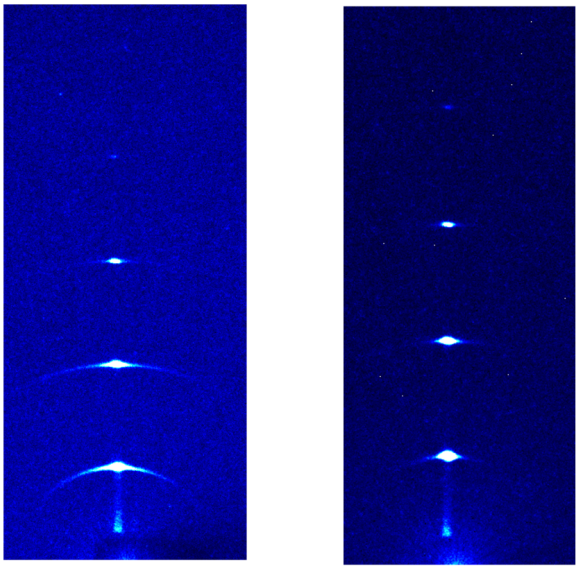

FIGURE 6.6: Characteristic x-ray diffraction patterns of (a)27-HC DLPC bilayers at X_c=15 mol% at T=15°C and (b)27-HC DLPC bilayers at X_c=17.5 mol% at T=15°C

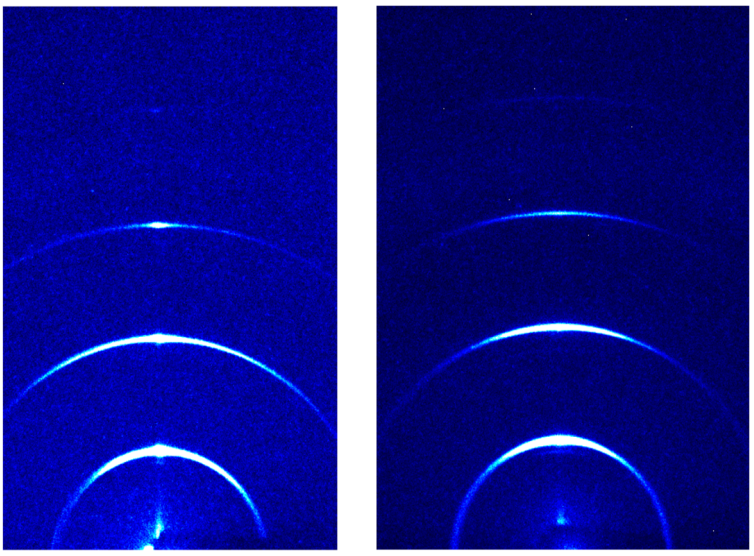

FIGURE 6.7: Characteristic x-ray diffraction patterns of (a)25-HC POPC bilayers at X_c=15 mol% at T=15°C and (b)27-HC POPC bilayers at X_c=15 mol% at T=15°C

6.6 Discussion

The fluid-fluid coexistence observed in 25-HC DLPC bilayers is consistent with similar behaviour seen in binary mixtures of this oxysterol with longer chain lipids DMPC and DPPC [7]. The trans-bilayer electron density maps of the coexisting lamellar phases, indicate that the sterol-rich phase has a higher bilayer thickness of $d_{hh} \sim 36\mathring{A}$ compared to the sterol poor phase which has a bilayer thickess of $d_{hh} \sim 31\mathring{A}$. Such increase in the bilayer thickness with sterol content is well known in lipid-cholesterol bilayers and is attributed to the stretching of the lipid chains in the presence of cholesterol. Our results indicate that similar "chain-condensing" effect is produced by 25-HC.

Both 25-HC and 27-HC induce fluid-fluid phase separation in DMPC bilayers [7], whereas only 27-HC induces this behaviour in DPPC bilayers [6]. On the other hand, our results show that only 25-HC leads to phase separation in DLPC. These results suggest that the thickness of the lipid bilayer plays an important role in the fluid-fluid phase separation seen in binary oxysterol - lipid systems. It is possible that the oxysterol molecules form hydrogen bonded dimers in bilayers of appropriate thickness, leading to phase separation. Further work is needed to confirm this hypothesis.

6.7 Conclusions

Our results suggest that 25-HC has a "condensing effect" on the lipid chains, similar to cholesterol. They also suggest that the bilayer thickness plays an important role in the fluid-fluid phase separation seen in oxysterols-lipid bilayers.

Bibliography

[1] J. R. Silvius, *Biochim. Biophys. Acta*, **1610(2)**, 174 (2003).

[2] J. J. Theunissen, R. L. Jackson, H. J. Kempen and R. A. Demel, *Biochim. Biophys. Acta.*, **860(1)**, 66 (1986).

[3] R. P. Holmes and N. L. Yoss, *Biochim. Biophys. Acta*, **770(1)**, 15 (1984).

[4] J. B. Massey, *Curr. Opin. Lipidol*, **17(3)**, 296 (2006).

[5] J. B. Massey and H. J. Pownall, *Biochemistry*, **45(35)**, 10747 (2006).

[6] Bibhuranjan Sarangi, PhD thesis: Organization of sterols in Model Membranes, Jawaharlal Nehru University, New Delhi, Chapter 4.

[7] M. A. Kamal, PhD thesis: Influence of some membrane active biomolecules on the phase behaviour of model lipid membranes, Jawaharlal Nehru University, New Delhi, Chapter 4.

[8] B. N. Olsen, P. H. Schlesinger, D. S. Ory and N. A. Baker, *Biochim. Biophys. Acta.*, **1818(2)**, 330 (2012).

[9] N. Kucerka,Y. Liu,N. Chu, H. I. Petrace, S. Tristram-Nagle and J. F. Nagle, *Biophys. J.*, **88(4)**, 2626 (2005).

[10] N. Kucerka, M. P. Nieh and J. Katsaras, *Biochim. Biophys. Acta.*, **1808(11)**, 2761 (2011).

Chapter 7

Interaction and Structure of AMP-DMPC bilayers

7.1 Introduction

Self-assembled lipid membranes play host to a number of processes from encapsulation of proteins and smaller molecules to acting as a substrate aiding the study of the physical principles governing the above [1, 2]. The tunability and adaptability of these membranes provide a multitude of well established phases that have been shown to be functional intermediates of cell membranes.

7.2 Previous Studies

Abiogenesis is an extensive field of study looking into the non-enzymatic synthesis of the precursors of life [3, 4]. Earlier reports have shown that polymerization of mononucleotides, like 5'-adenosine monophosphate (AMP) (Figure 7.1), occur under extreme conditions [5]. Oligomerization due to the formation of phosphodiester bonds between nucleotides seen here are highly suggestive of prebiotic assemblies leading to the formation of RNA-like polymers. The structure and phase behaviour of dimyristoyl phosphatidyl choline(DMPC), (Figure 7.2), is well established [6]. The complete structural resolution of the low temperature 1-D modulated bilayer phases has been carried out earlier. Specifically, the effect AMP molecules on DMPC has also been looked at

previously[7, 8]. Subjecting the samples to multiple cycles of hydration and dehydration under suitable pH conditions has demonstrated the adsorption of AMP molecules onto lipid bilayers. Further the nucleotides form ordered arrays post condensation onto the bilayers[9, 10].

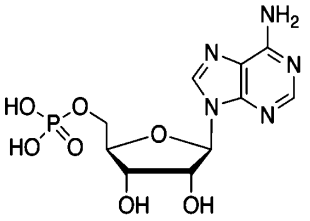

FIGURE 7.1: Structure AMP molecule

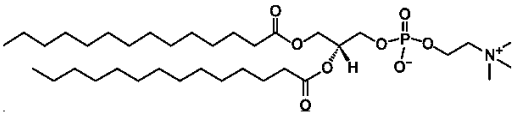

FIGURE 7.2: Structure of DMPC

7.3 Aim of Present Studies

In this chapter, we look at the structural changes, induced through doping of DMPC bilayers with AMP. We prepare oriented multilayer samples of the above mixtures at different compositions and extract small-angle x-ray scattering profiles at different temperatures. Trans-bilayer electron density profiles of the bilayers were constructed from the patterns observed. We also image the mixtures through freeze-fracture Cryo-SEM technique, and correlate them with the results of the diffraction experiments.

7.4 Materials and Methods

5'-adenosine monophosphate (AMP) and dimyristoyl phosphatidylcholine(DMPC) were procured from Sigma-Aldrich. All chemicals were used as received.Stock solutions of AMP were prepared in Millipore water within the solubility limit ($\sim$ 4 mg/mL) and added to accurately weighed amounts of DMPC to reach the required composition. Bilayer stacks were prepared by coating the mixtures on the external surface of a clean glass beaker (r $\sim$ 1 cm). The samples are then sealed in a larger beaker with a water

reservoir and allowed anneal at room temperature to form extended bilayer stacks. The samples are then loaded into a humidity and temperature controlled chamber for the small-angle x-ray scattering studies.

7.5 Results

7.5.1 Characteristic X-ray diffraction patterns of AMP-DMPC bilayers

At ratios of AMP:DMPC[1:1], the bilayers exhibit a single fluid phase at temperature well above T_m of DMPC(Figure 7.3,(d)). On lowering the temperature two distinct sets of lamellar peaks emerge (Figure 7.3(b,c)). We refer to the phase with lesser periodicity as L_α and the one with the higher periodicity as L_{amp}. At lower temperatures the L_α disappears and only the L_{amp} phase is present. A similar trend was observed for other ratios of AMP:DMPC; 1:2 (Figure 7.4), 1:3 (Figure 7.5)and 1:4 (Figure 7.6). There is also a gradual shift in intensity on cooling as more of L_{amp} type bilayers are present (Figure 7.7). At all points sampled there were sharp peaks indicative of crystallization of AMP in the wide-angle region that do not disappear upon heating and annealing at high temperatures (T $\sim$ 50°C).

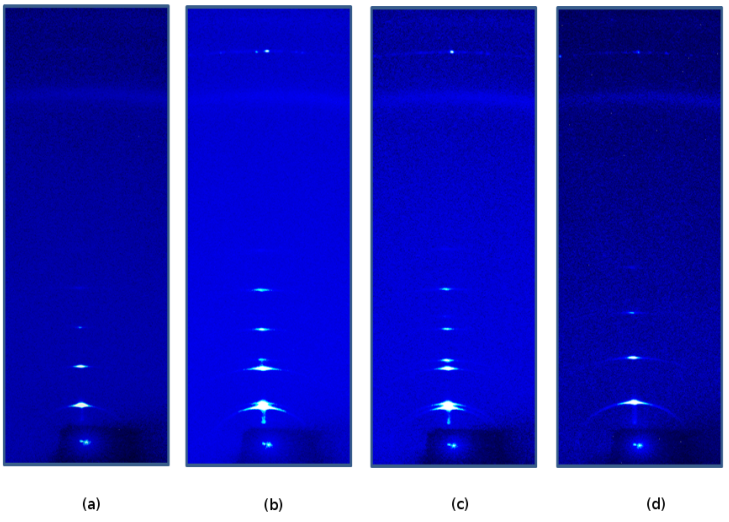

FIGURE 7.3: X-ray diffraction patterns of AMP-DMPC [1:1] multilayers at different temperatures;
(a)T=25°C:(b)T=30°C:(c)T=34°C:(d)T=37.4°C.

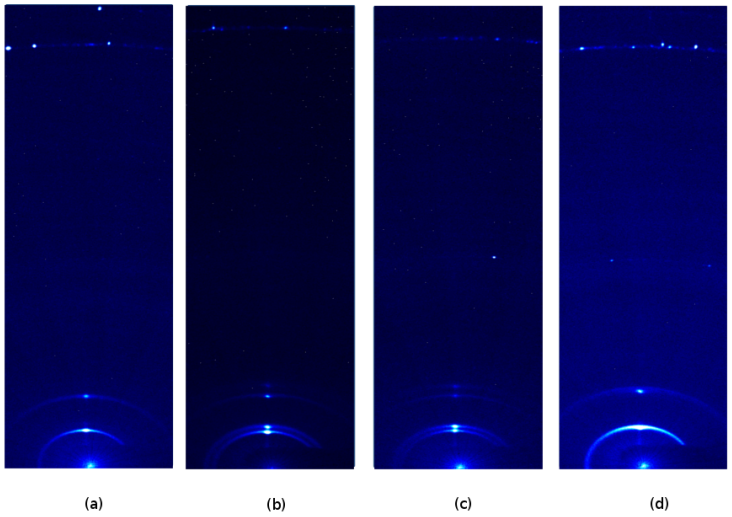

FIGURE 7.4: X-ray diffraction patterns for AMP-DMPC [1:2]at different temperatures; (a)T=29.6°C:(b)T=31°C:(c)T=35.5°C:(d)T=38.2°C.

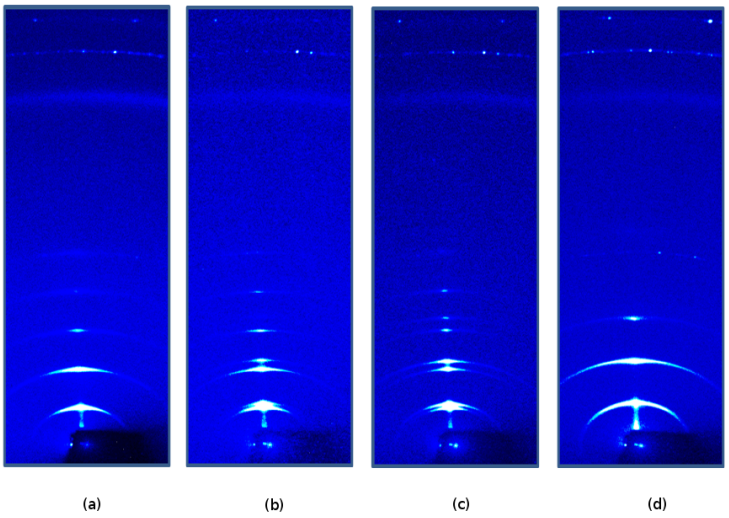

FIGURE 7.5: X-ray diffraction patterns for AMP-DMPC [1:3]at different temperatures; (a)T=25°C,(b)T=29°C,(c)T=32.5°C, (d)T=36°C.

Table 7.1 contains the lamellar periodicities obtained for the mixtures at different compositions and temperatures. The high temperature L_α phase is consistently seen to have a periodicity smaller by $\sim$ 7-8 Å than the low temperature L_{amp} phase in samples with composition [1:1],[1:2] and [1:3]. Samples made at AMP:DMPC[1:4] display a difference of about 6.2 Å between these phases.

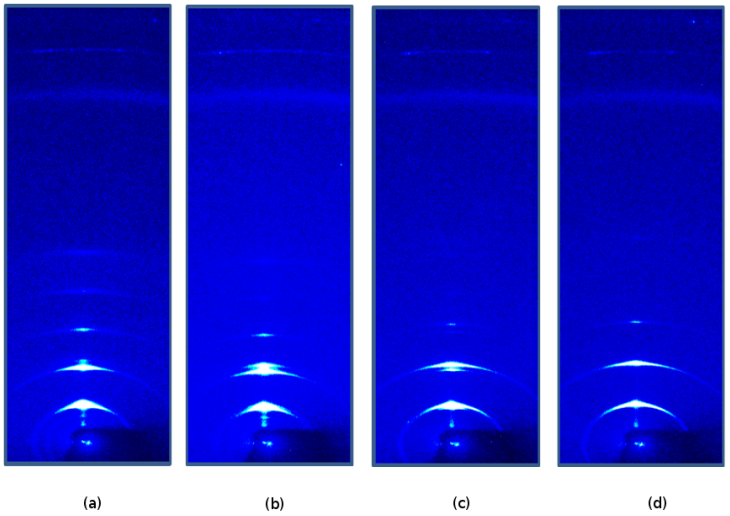

FIGURE 7.6: X-ray diffraction patterns for AMP-DMPC [1:4]at different temperatures; (a)T=28°C,(b)T=32.4°C,(c)T=36.2°C, (d)T=39°C.

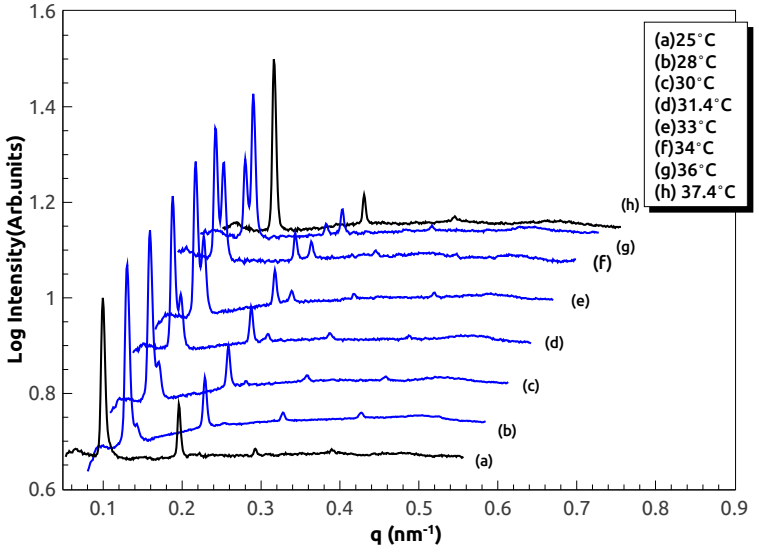

FIGURE 7.7: Integrated x-ray diffraction intensities of AMP-DMPC [1:1] multilayers

7.5.2 Electron Density Profiles of AMP:DMPC bilayers

The relative electron density profiles (edp) calculated for AMP:DMP ratios of [1:1] and [1:3], after correct phase allocation are shown in Figure 7.8 and Figure 7.9, respectively. The edp are evaluated for the L_α phase, L_{amp} phase and across the two-phase coexistence region. Table 7.2 contains the values for headgroup spacing (d_{hh}), which is a reliable measure of the width of the bilayer obtained directly from the edps.

TABLE 7.1: Lamellar periodicities d (in Å) of AMP-DMPC bilayers as a function of temperature.

1:1		**1:2**		**1:3**		**1:4**	
T [°C]	d [Å]	T[°C]	d [Å]	T[°C]	d [Å]	T[°C]	d [Å]
25	61.6	29.6	66.6	19.5	63.8	28	64.5
28	61.6,*54.9*	31	66.6,*55.9*	25	63.8	30.4	66.6,*61.3*
30	62.5,*54.9*	32.5	67.3,*59.5*	29	63.8,*56.7*	32.4	65.9,*62.5*
31.4	62.7,*55.9*	35.5	68.1,*59.5*	32.5	62.5,*56.7*	34.4	64.5,*61.3*
33	62.7,*55.9*	36.7	65.2,*58.9*	33.6	61.3,*56.2*	36.2	63.8,*60.1*
34	62.7,*55.9*	38.2	*58.3*	36	*55.9*	39	*58.3*
36	61.6,*54.9*						
37.4	*54.5*						

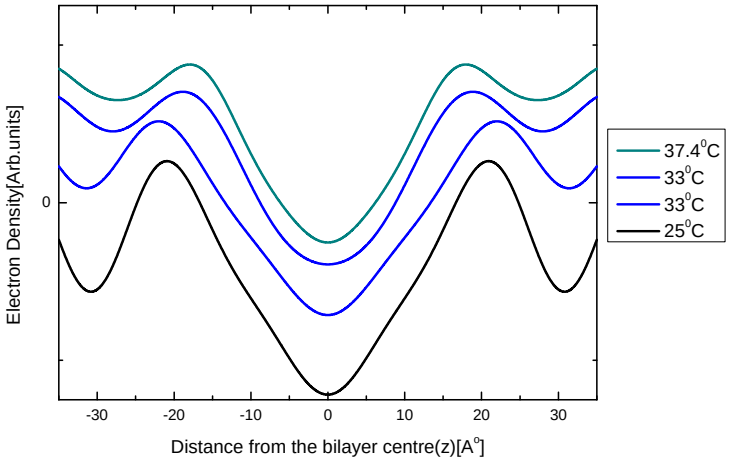

FIGURE 7.8: Trans-bilayer electron density profile of AMP-DMPC[1:1] multilayers across different temperatures spanning the two-phase coexistence region

TABLE 7.2: d_{hh}[Å] for AMP-DMPC bilayers as a function of temperature

1:1		**1:3**	
T [°C]	**d_{hh}[Å]**	**T [°C]**	**d_{hh}[Å]**
37.4	36.06	36	35.86
33	37.56	32.5	38.12
	43.94		44.88
25	42.08	25	44.12

7.5.3 Cryo-SEM imaging of AMP:DMPC bilayers

Cryo-SEM images were obtained for pure DMPC bilayers and compared with those at different amounts of added AMP. "Scroll-like" images obtained for DMPC bilayer indicate the presence of multilamellar vesicles (Figure 7.10,(a,b)). The addition of AMP

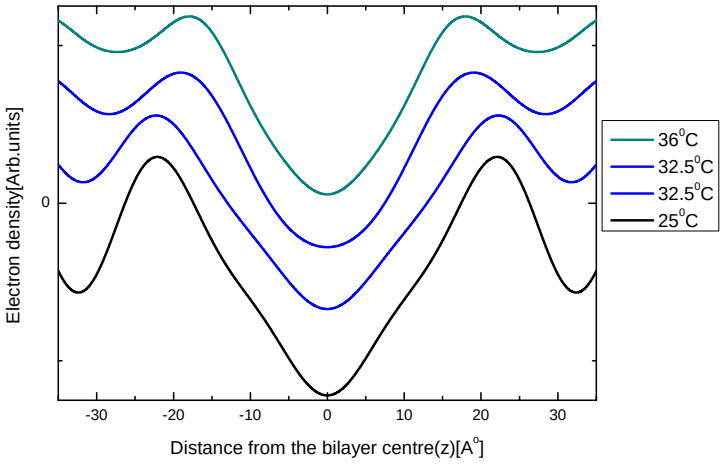

FIGURE 7.9: Trans-bilayer electron density profile of AMP-DMPC[1:3] across different temperatures spanning the two-phase coexistence region

causes the bilayer to electrostatically swell and form small unilamellar vesicles(SUVs) (Figure 7.10(c-f)).

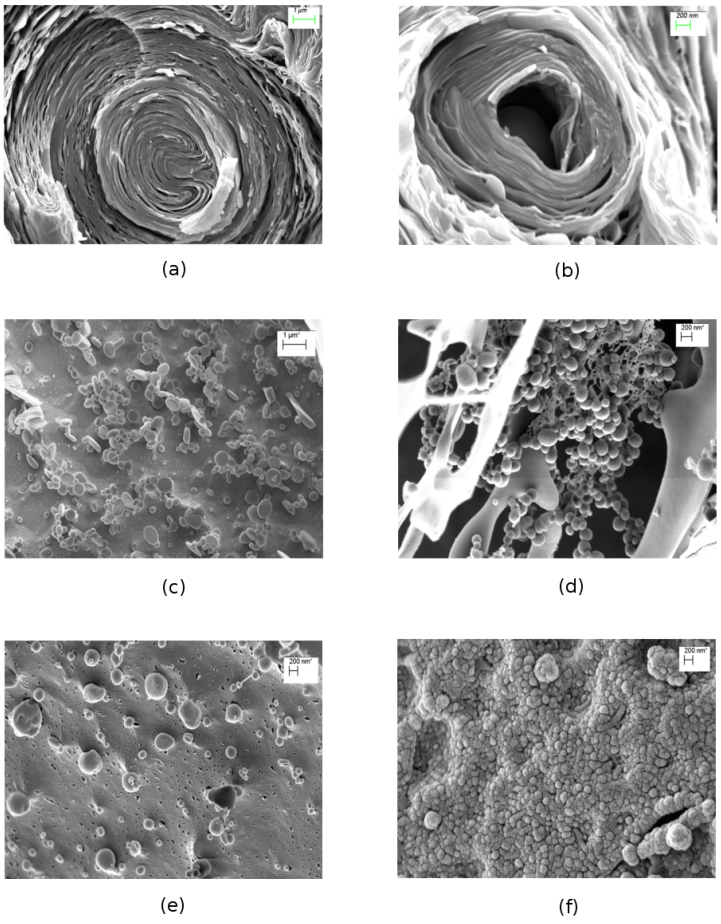

FIGURE 7.10: Cryo-SEM micrograph of AMP-DMPC bilayers : (a) and (b) [Pure DMPC] ; (c) and (d) [1:1] ; (e) [1:2], (f) [1:3]

7.6 Discussion

In this chapter we have studied the influence of AMP on the phase behaviour of DMPC bilayers. Our diffraction data indicate that AMP has significant effect on the structure of DMPC bilayers. At neutral pH the acid form of AMP used in the present studies is expected to be doubly ionized. Our studies indicate that these AMP ions bind to the DMPC bilayer, probably through their hydrophobic moieties creating a surface charge density on the bilayers. This leads to the formation of unilamellar vesicles in dilute solutions as observed through Cryo-SEM imaging. This binding in turn leads to a transition at around 37°C. The electron density profiles show that one of the coexisting phases has a higher bilayer thickness probably due to the binding of AMP. These results indicate that nucleotides such as AMP can bind to lipid bilayers and form clusters. It is possible that such nucleotide rich clusters will facilitate their oligomerization as proposed in the RNA world hypothesis for the origin of life on earth. While our results clearly indicate the formation of nucleotide rich patches on the bilayer the mutual orientation of nucleotides within these patches will have to be probed further.

At lower temperatures a single phase is obtained which shows a 1-D lamellar structure. The ripple phase of DMPC is clearly suppressed on binding of AMP.

7.7 Conclusions

In this chapter we have studied the interaction AMP with DMPC bilayers. AMP binds to DMPC bilayers leading to a repulsive inter-bilayer interaction in dilute samples. At higher concentrations AMP significantly alters the phase behaviour of DMPC bilayers. The coexistence of two lamellar phase with different bilayer thicknesses suggest that AMP is capable of forming dense clusters on lipid membranes which might facilitate their oligomerization.

Bibliography

[1] I. Vattulainen, *J. Am. Chem. Soc.*, **130**, 44 (2005).

[2] J. P. Schlebach and C. R. Sander, *Q. Rev. Biophys.*, **48(1)**, 1 (2015).

[3] D. W. Deamer, *Origins Life*, **17**, 3 (1985).

[4] L. E. Orgel, *Crit. Rev. Biochem. Mol. Biol.*, **39**, 99 (2004).

[5] D. W. Deamer and C. D. Georgiou, *Astrobiology*, **15**, 1091 (2015).

[6] K. Akabori and J. F. Nagle, *Soft Matter*, **11(5)**, 918 (2015).

[7] L. Toppozini, H. Dies, D. W. Deamer and M. C. Rheinstadter, *PLoS one*, **8**, 62810 (2013).

[8] S. Himbert, M. Chapman, D. W. Deamer and M. C. Rheinstadter, *Nature Sci. Rep.* , **6**, 31285 (2016).

[9] L. Misuraca, F. Natali, L. Silva, J. Peters, B. Deme, J. Olivier, T. Seydel, V. Laux-Lesourd, D. W. Deamer and M. C. Maurel, *Life*, **7(1)**, 2 (2017).

[10] C. V. Mungi and S. Rajamani, *Life*, **5(1)**, 65 (2015).

Chapter 8

Summary

In this thesis we have studied the various structures formed by polyelectrolyte complexes made of cationic surfactants and DNA. In the case of CTAT-DNA complexes, we observe that the $H^c_{I,s}$, phase which is a swollen $\sqrt{3} \times \sqrt{3}$ superlattice of the underlying H^c_I structure, transforms into the H^c_I structure under application of osmotic pressure. The other phases exhibited by this system H^c_I and the S^c_I structure do not change their structures under osmotic pressure. Through elemental analysis we confirm that the DNA to micelle stoichiometry of the structures is as predicted by the proposed structures for these complexes. Phase behaviour of the amphiphile CTAB, that is a variant of CTAT having a Br_- counterion, is observed to form only the H^c_I phase across all values of ρ probed. The addition of NaCl is seen to lead to robust development of the H^c_I structure. Here, we also compare two models proposed in the literature for the H^c_I phase, namely $H^c_{I,21}$ and $H^c_{I,31}$, where the DNA to micelle ratios are 2:1 and 3:1, respectively. Through analysis of diffraction data we establish the $H^c_{I,21}$ structure as the correct form. Stoichiometric analysis of the H^c_I complex of CTAB-DNA indicates that the DNA to micelle ratio varies across the ideal value expected from the structural model, depending on which of the two species is in excess. This could possibly be due to the formation of voids in the lattice at the site of the deficient species. Further experiments are needed to unequivocally establish this conclusion.

The shorter chained analogue of CTAB, DTAB, does not form complexes with well developed long-range translational order due to it's tendency to aggregate into small micelles. The addition of monovalent salt NaCl to these complexes is seen to induce

growth of micelles and development of well ordered structures. The $H^c_{I,s}$ and the S^c_I structures are observed at low and high values of ρ respectively, but the H^c_I lattice is never observed. Further the application of osmotic pressure is seen not to induce a transformation of the $H^c_{I,s}$ lattice. This suggests that the structure of this phase might be different from that observed in the CTAT-DNA system. Further the stoichiometry of this assembly is seen to be different from that expected for the structure proposed for the $H^c_{I,s}$ phase of CTAT-DNA complexes. We do not at present have a well defined structure that describes the $H^c_{I,s}$ phase of DTAB-DNA complexes.

Our results indicate that the structure of surfactant-DNA complexes is very sensitive to the chain length of the surfactant. Therefore, along with the cosurfactant and counterion the chain length is a very convenient parameter to tune the structure of these systems. At present there are no theoretical studies on the energetics of these systems that can explain their rich polymorphism. We hope our studies would motivate future investigations along this direction.

In this thesis we have also looked at some bilayer assemblies formed by certain biomolecules and lipid membranes. Vitamin D3 doped DPPC bilayers were reported to form a novel, thickness-modulated, rectangular-centred lattice. Here we have proposed a model to describe the structure of this RC phase and estimate it's salient structural features.

Early studies had suggested the occurrence of a fluid-fluid coexistence in binary lipid-cholesterol membranes. However, later studies do not provide any evidence for such a phase behaviour. Interestingly, 25-hydroxycholesterol and 27-hydroxycholesterol were found to induce coexisting fluid phases in PC membranes. We have studied the influence of the lipid chain length on this phase behaviour. It is found that 25-hydroxycholesterol induces fluid-fluid coexistence in DLPC but not 27-hydroxycholesterol. On the other hand both these oxysterols form coexisting fluid domains with the longer chained lipid DMPC. Our results suggest that the bilayer thickness plays an important role in this phase behaviour. It is possible that dimer formation between oxysterol molecules in the two leaflets of the bilayer is responsible for the observed behaviour. Further work is necessary to confirm this conjecture.

The interaction of mononucleotides with lipid bilayers is of great interest for understanding the origins of life on earth. In this thesis, we also looked at the interaction of the mononucleotide, AMP, with DMPC lipid bilayers. Adsorption of AMP onto the

lipid bilayers was seen to induce a coexistence of two lamellar phases with different periodicities. The modelling of these phases showed they contain bilayers of different thickness. Further freeze-fracture Cryo-SEM imaging shows that the binding of AMP swells the bilayers to form SUVs. This shows that AMP endows a surface charge density to the bilayers on adsorption, thereby causing the swelling. The interactions between the grafted AMP and the lipid needs to be probed further to understand the observed phase behaviour.